Scientific report ; WR 2009-04

Detection of Cb and TCu clouds using MSG-SEVIRI cloud physical properties and weather radar observations

Cintia Carbajal Henken, Maurice Schmeits, Erwin Wolters and Rob Roebeling

De Bilt, 2009

KNMI scientific report = wetenschappelijk rapport; WR 2009-04

De Bilt, 2009

PO Box 201
3730 AE De Bilt
Wilhelminalaan 10
De Bilt
The Netherlands
http://www.knmi.nl
Telephone +31(0)30-220 69 11
Telefax +31(0)30-221 04 07

Authors: Carbajal Henken, C.K.
Schmeits, M.J.
Wolters, E.L.A.
Roebeling, R.A.

Detection of Cb and TCu clouds

using MSG-SEVIRI cloud physical properties and weather radar observations

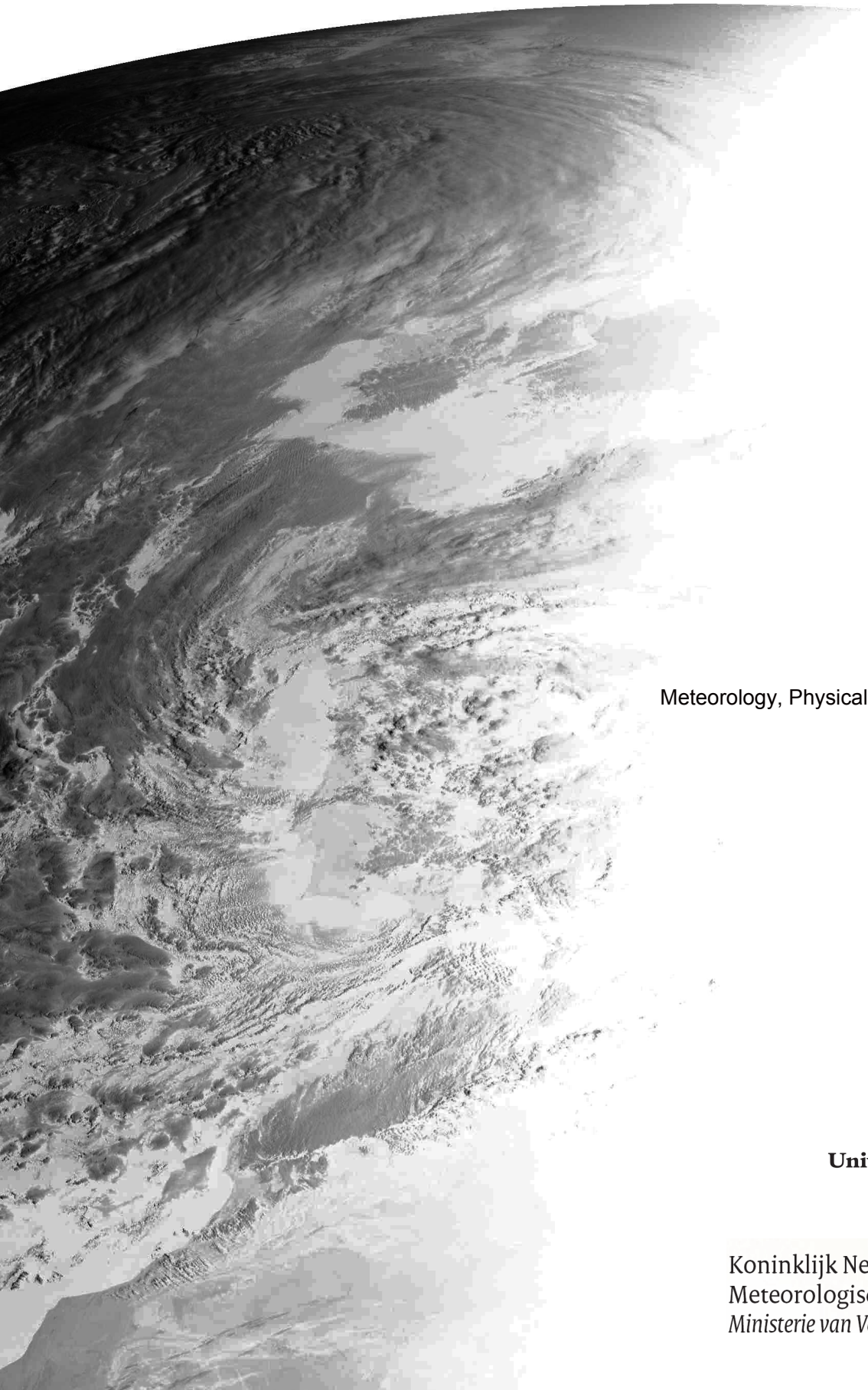

Master Thesis
Cintia Carbajal Henken
Utrecht University
IMAU
Meteorology, Physical Oceanography and Climate
September 2009

Supervisor IMAU
Dr. Geert-Jan Roelofs

Supervisors KNMI
Dr. Rob Roebeling
MSc. Erwin Wolters

Universiteit Utrecht

Koninklijk Nederlands
Meteorologisch Instituut
Ministerie van Verkeer en Waterstaat

Master Thesis by Cintia Carbajal Henken (C.K.CarbajalHenken@phys.uu.nl), 2008–2009 supervised by Dr. Geert-Jan Roelofs (IMAU), Dr. Rob Roebeling (KNMI) and Erwin Wolters (KNMI).

Cover image: Meteosat HRV satellite image (edited) taken on 16 September 2009 at 18.00 UTC.

Abstract

Deep convective clouds, such as Towering Cumulus (TCu) and Cumulonimbus (Cb) clouds, may pose a serious risk to aviation. For a responsible replacement of human observers at airport weather stations in the Netherlands by automated observation systems of present weather, a Probability Of Detection (POD) of at least 80 % and a False Alarm Rate (FAR) of no more than 20 % is required. Therefore, the POD (58 %) and FAR (70 %) of the present KNMI automated radar-based Cb/TCu cloud detection method are not considered satisfactory. In this study, satellite derived cloud physical properties and High Resolution reflectances in the Visible (HRV) as well as weather radar data are used to develop a new Cb/TCu cloud detection method. The cloud physical properties are derived from the visible and near-infrared channels of the Spinning Enhanced Visible and InfraRed Imager (SEVIRI) onboard a Meteosat Second Generation (MSG) satellite. The detection method is constructed for a MSG box area around Schiphol airport for the daytime summer period. METeorological Aerodrome Reports (METAR) of Cb and TCu clouds are used as 'ground truth'. The Cb/TCu cloud detection method is performed in two steps. First, a Convective Cloud Mask (CCM) is constructed to produce a hazard map. This map includes pixels which represent potential convective cloud pixels based on a thresholding technique. For the hazard map, the level of risk, which indicates the probability of presence of Cb/TCu clouds at and in the vicinity of the airport, is determined using a logistic regression model. Predictors for the model have been derived from the cloud physical properties, HRV reflectance and weather radar data. The frequent selection of the HRV derived predictors in the forward stepwise selection method revealed the importance of high resolution satellite data. Therefore, a cloud optical thickness has been derived from the HRV reflectance. The CCM shows a two-third decrease for the non-events (no Cb/TCu clouds), while over 95 % of the yes-events (Cb/TCu clouds) remain. The predicted probabilities from the logistic regression model show good Reliability and Resolution and positive skill over sample climatology. Using the Critical Success Index (CSI) and the Bias, a probability threshold is determined to convert predicted probabilities into predicted group memberships. Combining the results from the CCM with the results from the final logistic regression model, a POD of 65.2 % and a FAR of 35.4 % are obtained for a maximum CSI and a bias of no more than 5 %. These verification scores show a substantial improvement with respect to the scores from the present automated Cb/TCu cloud detection method.

Contents

1st Chapter

INTRODUCTION

Convective clouds, such as the Towering Cumulus (TCu) and Cumulonimbus clouds (Cb), can be striking features in the sky, but may also produce hazardous weather. Especially deep convection, such as a mature cumulonimbus cloud, is accompanied by rapidly changing weather on different spatial and temporal scales. Weather associated with convective clouds consists of precipitation in the form of intense rain showers, snow, hail or graupel. Also strong winds and lightning may be present. Turbulence, strong wind shears, reduced visibility, heavy precipitation and lightning, and the onset of ice on airplanes within and around convective clouds can be a threat to aviation. At the same time, the hazardous weather increases annual costs in the aviation industry due to time and fuel loss that arise from delayed, canceled and rerouted flights as well as accidents. Furthermore, the presence of hazardous weather can be relevant to ground transport, tourism, the energy supply industry, the construction industry and farmers. Heavy precipitation can lead to flash flood events causing destruction to homes and businesses and occasionally also fatalities.

The need to accurately forecast, detect and monitor hazardous weather phenomena has led to the development of numereous methods for forecasting, detection and monitoring of convective initiation, clouds and precipitation. Current techniques for detection and monitoring of convective clouds and the nowcasting (forecasting up to 2-6 hours) of severe weather are based on near real-time information given by radar and satellite. Numerical weather prediction models have problems forecasting the onset of convection due to inaccurate representations of the atmospheric state and the dynamic and micro-physical state of clouds on sub-grid (small scale) resolution. Radars can be used to detect convective precipitation, but the spatial coverage of radar networks is usually limited. Satellites can be used to detect convective clouds before the onset of precipitation and in areas of limited radar coverage. Various cloud characteristics can be identified from visible and infrared satellite images using multispectral techniques. Several methods use (dynamic) thresholds in visible and (combined) infrared satellite channels for cloud classification and rainfall estimations, but also more advanced pattern recognition techniques have been developed. Less methods use satellite derived cloud physical properties to detect convective clouds and estimate convective rainfall.

The ability to detect and monitor convective clouds increases with increasing satellite resolution both in space and time. In 2002, the first Meteosat Second Generation (MSG) satellite has been launched into space. The onboard Spinning Enhanced Visible and InfraRed Imager (SEVIRI) has an increased time resolution of 15 minutes compared to the 30 minutes of the older generations of satellites. The horizontal resolution for the (near) infrared channels increased from 5 km to 3 km at the sub-satellite point. Also the number of spectral channels has increased and a high resolution visible channel with a horizontal resolution of 1 km is included, which was 2.5 km for the older generation. The EUropean organization for the exploitation of METeorological SATellites (EUMETSAT) has initiated the Satellite Application Facility on Climate Monitoring (SAF-CM) to retrieve cloud physical properties, such as the optical thickness and particle size, for climate trend watching. The cloud physical properties are derived from visible and near-infrared cloud reflectances and infrared cloud top brightness temperatures using SEVIRI observations, a Cloud Physical Property (CPP) algorithm and Radiative Transfer Model (RTM) simulations.

At the Royal Netherlands Meteorological Institute (KNMI), the automated observation system of present weather (AUTO METAR) uses a radar algorithm adopted from Météo-France to detect towering cumulus and cumulonimbus clouds. It is based on radar reflectivity thresholds and area size of the precipitation echoe, as well as on information from a lightning detection network (Wauben *et al.*, 2006). The aim of the KNMI is to fully automize present weather observations at most weather stations in the Netherlands. However, for a responsable replacement of human observers at Dutch airports by an automated observation system, the Probability Of Detection (POD) of Cb clouds (58%) and the large False Alarm Rate (FAR) (70%) of the present radar algorithm are not considered to be satisfying. A probability of detection of at least 80% and false alarm rate of no more than 20% are required. Combining weather radar data with satellite data is expected to improve the detection of convective clouds and to decrease false alarms. Also, the increased time and spatial resolution of SEVIRI opened new possibilities in this research area. The objective of this thesis research is to develop an automated Cb/TCu cloud detection method using MSG-SEVIRI derived cloud physical properties and reflectance in the visible. The main research question is as follows:

How can satellite derived cloud physical properties and reflectances contribute to an improved automated detection method of towering cumulus and cumulonimbus clouds?

An improvement of the convective cloud detection method over the present radar-based method at the KNMI will be measured in terms of probability of detection and false alarm rate. The cloud physical properties and reflectance in the visible are related to the presence of convective clouds in satellite images in a physical and statistical sence. Supplementary to the main research question, the following sub-questions can be addressed:

How can cloud physical properties and reflectance in the visible be related in a physical sense to convective clouds to determine hazard?

How can cloud physical properties and reflectance in the visible be related in a statistical sense to convective clouds to determine level of risk?

Hazard is the potential to cause harm. Convective clouds are considered to form a hazard to aviation when present at and within the surroundings of the airport. The cloud physical properties and the reflectance in the visible are used to differentiate between convective and non-convective clouds within a satellite image. Convective clouds will pose a serious risk to aviation when they have grown into severe convective clouds (Cb/TCu). For hazardous cloud areas within the satellite image, the risk of the clouds being Cb/TCu clouds is determined by relating cloud physical properties and reflectance to convective clouds in a statistical manner. Therefore, risk can be understood as the likelihood of harm and is expressed in terms of probability.

The structure of this thesis is as follows. In Chapter 2 background information is given on the formation and characteristics of convective clouds and associated weather as well as the basics of radiative transfer in a cloudy atmosphere. Furthermore, MSG and onboard SEVIRI will be treated followed by a small section on radar principles. In Chapter 3 a brief overview of historical and state-of-the art methods that use satellite data to detect and monitor convective initiation, convective clouds and convective precipitation will be given. Chapter 4 presents the MSG-SEVIRI cloud physical properties and reflectance dataset and METeorological Aerodrome Reports (METAR) used in this research. Furthermore, the two steps within the automated Cb/TCu cloud detection method, a convective cloud mask and logistic regression, are presented. In Chapter 5 the results of the Cb/TCu cloud detection method will be shown. A discussion and conclusion are provided for in Chapter 6.

2nd Chapter

BACKGROUND

2.1 CONVECTIVE CLOUDS

Not much was known about the structure of clouds until after World War II instrumented aircrafts for atmospheric measurements were used. In the late 1940s there was the Thunderstorm Project in Florida and Ohio, which was the first project to do quantitative measurements of precipitating convective clouds. Byers and Braham (1949) published an article describing a typical thunderstorm (principal diurnal convection over land) consisting of a number of individual convective cells, each evolving through a life cycle that has three stages: the cumulus stage, the mature stage and the dissipating stage. They observed that for a single cumulus cell it takes about one hour to complete the life cycle and that a thunderstorm consists of several cells, each at a different stage in the life cycle. Nowadays, measurements of clouds can be made using well-equipped aircrafts and remote sensing devices that can be operated from aircrafts, satellites and from the surface, such as radar and microwaves. Also lidar and in-situ measurements from rawinsondes are used.

In this section, deep, moist convection giving rise to towering cumulus and cumulonimbus clouds will be treated. First, convection and the formation of cumulus clouds will be addressed. Subsequently, a characterization of towering cumulus and cumulonimbus clouds is given. Finally, the occurrence of these types of clouds and associated weather in the Netherlands is treated.

2.1.1 CONVECTION AND THE FORMATION OF CUMULUS CLOUDS

Convection in the atmosphere is the transport of heat, moisture and momentum by the movement of fluid. Heat consists of sensible heat and latent heat. Sensible heat is the heat that can be measured with a thermometer, while latent heat is heat related to a substance changing its physical state, such as water vapour condensating into liquid water droplets. Convection in which no visible clouds are formed is called dry convection. Convection in which phase changes of water do play an important role is called moist convection. Both convection types remove excess heat from the earth's surface and transport it

into the atmosphere. When the depth of convective clouds extends to a substantial fraction of the troposphere, the convection is referred to as deep, moist convection (Bluestein, 1993).

Clouds can form when an air parcel is lifted upwards due to mechanical forces (low-level convergence, orography) or buoyant forces. If heat sources or sinks are not considered and the parcel is lifted mechanically, it undergoes adiabatic expansion and cools at the dry adiabatic lapse rate, which is about 10 K/1000 m. At a height where the parcel cools enough to become saturated, the water vapour in the air will condense into liquid water droplets. This height level is called the Lifting Condensation Level (LCL). Cumulus clouds [1] may arise from surface heating of a stable boundary layer. When the surface air is heated up to the convective temperature, a surface air parcel becomes very buoyant and accelerates upward. Warm parcels of air that rise upward from the surface are also referred to as thermals and have horizontal extents of 0.1 to 10 km (Houze, 1993). The buoyancy of an air parcel does not only arise from temperature and pressure differences, but also has contributions from water vapour and the weight of hydrometeors (precipitation particles) in the air (Houze, 1993). The buoyancy B can be approximated by

$$B \approx g \left[\frac{T^*}{T_0} - \frac{p^*}{p_0} + 0.61 q_0^* - q_H \right] \tag{2.1}$$

in which T^* and p^* are the temperature and pressure perturbations with respect to a reference state, respectively, q_0^* is the mixing ratio of water vapour (mass of water vapour per unit mass of air) and q_H is the mixing ratio of hydrometeors (total mass of liquid water and ice particles per unit mass of air). The temperature and pressure perturbations can have both a negative and positive contribution to the buoyancy. The water vapour only has a positive contribution to the buoyancy due to the fact that water molecules are lighter than other molecules found in the air. The hydrometeors always has a negative contribution to the buoyancy of an air parcel due to exerted drag of particles on the air, which reduces its updraft speed. In convective clouds, generally all four terms are of the same order of magnitude (Houze, 1993).

Once the air parcel has become saturated, the water vapour will condensate on very small particles in the atmosphere called aerosols. They have natural sources, such as dust and sea salt, and anthropogenic sources, such as smoke and industrial particles. Aerosol particles that serve as a nucleus for a cloud droplet are called Cloud Condensation Nuclei (CCN). Typically, their size is of the order 0.1 μm, which is about 1/100 of the size of a typical cloud droplet and 1/10000 of a typical rain drop (Pruppacher and Klett, 1997). The size distribution of the water droplets is initially controlled by the size distribution of the CCN (Smith, 1997).

During the process of water vapour condensating into water, latent heat is released and therefore the air parcel is warmed. The amount of released heat is equal to the amount of heat necessary to evaporate the water. This means that once the parcel is saturated and continues to rise after passing the LCL, the release of latent heat prevents the parcel from cooling as fast as it would at the dry adiabatic lapse rate (Smith, 1997). The new cooling rate is called

[1] Cumulus is a Latin word meaning 'heap'.

the moist adiabatic lapse rate or pseudo adiabatic lapse rate and is always less than the dry adiabatic lapse rate. It is not constant, but depends on the moisture content, which, in turn, depends on the temperature, and on air pressure. Observed values range from about 4 K/1000 m for warm humid air in the lower troposphere to about 6-7 K/1000 m in the middle part of the troposphere (Holton, 2004). If the environmental lapse rate, which is the lapse rate of the surrounding atmosphere, is larger than the moist adiabatic lapse rate and the parcel is forced to continue to rise, it will reach a level where it becomes positive buoyant relative to the surrounding air. From this level on, called the Level of Free Convection (LFC), it can freely accelerate upward (Holton, 2004). The parcel will continue to rise until the Equilibrium Level (EL) has been reached. At this level the temperature of the air parcel has become equal to the temperature of the surrounding air and therefore it does not experience any positive buoyancy anymore. Generally, the parcel will overshoot the EL, sometimes even by several kilometres, due to large updraft speeds and inertia. Then, the parcel experiences negative buoyancy and will undergo a damped oscillation (Doswell, 2001).

A quantitative measure of convection (or latent instability) often used is the Convective Available Potential Energy or CAPE. It is a measure of the maximum possible kinetic energy a statically unstable parcel can acquire neglecting the effects of water vapour and water droplets on the buoyancy, neglecting entrainment (mixing with the surrounding air) and assuming instantaneous adjustment to the surrounding pressure (Holton, 2004). CAPE can be written as

$$CAPE = \int_{LFC}^{EL} B dz \tag{2.2}$$

which is equal to the amount of work done by the bouyancy force. The maximum updraft speed, w_{max}, an air parcel could achieve is calculated from CAPE. Hereby all of the potential energy of the air parcel would be converted into kinetic energy (Emanuel, 1994).

$$w_{max} = \sqrt{2CAPE} \tag{2.3}$$

For moderate to strong convection, typical values of CAPE range from 1000 to 3000 $m^2\ s^{-2}$, but also values up to 7000 $m^2\ s^{-2}$ have been observed. For a CAPE of 2500 $m^2\ s^{-2}$, the maximum updraft speed is about 70 ms^{-1} (Bluestein, 1993).

When convective clouds are very shallow, meaning their vertical extents is limited, or they are short lived, the microphysical processes that can make small droplets grow into water drops that are large enough to fall as precipitation, are not very effective. This means that little or no precipitation will form and all of the condensed water will re-evaporate. Examples of these kinds of non-precipitating cumulus clouds are Cumulus humilis clouds [2], also called fair-weather cumulus, trade-cumulus and stratocumulus [3] (Smith, 1997). Fig. 2.1 shows cumulus humilis clouds. The clouds appear dense, very white in the sun and have fuzzy outlines. The vertical growth of small cumulus clouds is

[2] Humilis is a Latin word meaning 'humble'.
[3] Stratus is a Latin word meaning 'spread out'.

Figure 2.1: Cumulus humilis clouds, also called fair-weather clouds (Young, 2007).

generally limited by a thermal inversion and their horizontal extents hardly exceed a couple of hundred meters. Under favourable atmospheric conditions such as extra surface heating, small cumulus clouds can develop into towering cumulus and cumulonimbus [4] clouds (Maas, 2002). Within clouds that continue to grow vertically, the Liquid Water Content (LWC) increases and precipitation will form at the onset of the mature stage (Smith, 1997). For clouds containing mainly droplets with a radius smaller than 10 μm, condensation is the dominant growth process of the water particles (Rogers and Yau, 1989). For clouds containing larger droplets, growth by collision and coalescence (capture of smaller droplets by larger cloud drops) becomes increasingly important. When large droplets gain enough weight they fall down, and collide and stick together with smaller droplets to form new, larger droplets. For warm clouds, whose cloud top temperatures are not colder than $0\,^{\circ}\mathrm{C}$, coalescence is the main process for the formation of rain. The effectiveness of the coalescence process increases with an increasing range of droplet size. Typically, a cumulus cloud consisting of a cloud droplet concentration of 100 droplets per cm^3 with an average radius of 10 μm grows into a cloud containing a rain drop concentration of 1000 drops per m^3 with an average radius of 1 mm in about 20 minutes. This takes in the order of 10^5 collisions (Rogers and Yau, 1989).

Once a cloud has extended to heights with temperatures below freezing point, ice crystals may form. For pure water droplets homogeneous freezing does not occur until temperatures below $-40\,^{\circ}\mathrm{C}$ are reached. However, with the presence of ice nuclei, freezing can occur just below the freezing point (Rogers and Yau, 1989). Super-cooled water drops are frequently found in clouds, espe-

[4] Nimbus (or nimbo) is a Latin word meaning 'cloud' or 'rain storm'.

cially in clouds having a cloud top temperature above $-10\,^{\circ}\mathrm{C}$. At a cloud top temperature of $-20\,^{\circ}\mathrm{C}$ only 10 % of the clouds entirely consist of super-cooled water drops (Pruppacher and Klett, 1997). However super-cooled water drops have been observed at temperatures of $-35\,^{\circ}\mathrm{C}$ over Germany (Weickmann, 1949) and at a temperature of $-40.7\,^{\circ}\mathrm{C}$ in clouds over the Rocky Mountains (Heymsfield and Miloshevich, 1993). The presence of ice crystals is more common in decaying clouds than in developing clouds (Rogers and Yau, 1989). The part of the cloud only containing ice crystals is said to be glaciated . When ice crystals form in the presence of super-cooled water drops, an unstable situation exists due to the fact that the equilibrium vapour pressure over ice is less than over water at the same temperature. This allows the ice crystals to grow by diffusion of water vapour from the evaporated drops. This ice crystal mechanism is called the Bergeron-Findeisen mechanism, which is most efficient at temperatures near $-15\,^{\circ}\mathrm{C}$ (Young, 1993). After gaining enough weight, an ice crystal will fall relative to water drops and it is its fall speed that largely determines the formation of various precipitation types. The collision and coalescence of an ice crystal with a water drop is called accretion and leads to the formation of graupel and hail. When two ice crystals clump together, it is called aggregation and leads to the formation of snow (Rogers and Yau, 1989). Which of the processes (ice crystal or collision and coalescence) dominates the formation of precipitation depends on the cloud top temperature, the liquid water content, the updraft speed and to some extent on the droplet concentration, but they may act concurrently within one cloud (Rogers and Yau, 1989). In cumulus clouds that are relatively warm, the coalescence process will be the dominant process for the formation of precipitation. Most of the world's precipitation (especially in the tropics) is formed under these circumstances (Young, 1993). Outside the tropics, the ice crystal mechanism will be dominant in relatively colder, convective clouds.

2.1.2 TOWERING CUMULUS AND CUMULONIMBUS CLOUDS

Clouds can be classified according to their shape and the height at which they are encountered. For height classification three height classes are identified; low heights from 0 to 2 km, middle heights from 2-7 km and upper heights from 5 to 13 km. The towering cumulus cloud and the cumulonimbus cloud are classified to the group of clouds encountered at low heights, although they can extend into all three height levels (Bleeker, 1980). The base of these clouds is relatively flat, in contrast to the rest of the cloud that has a cauliflower shape due to bulbous towers, see Fig. 2.2. The upper part of a mature Cb cloud is usually composed of ice crystals and spreads out in the shape of an anvil (Houze, 1993).

Deep, moist convection is indicated by the presence of thick cumulonimbus clouds that reach high altitudes (Hees and Lelieveld, 2000). Usually they form from well-developed cumulus clouds (via TCu clouds) in the boundary layer. The Cb clouds than can have a cloud base height as low as 400 m, but sometimes also up to 4 km, depending on the depth of the boundary layer. Here surface heating does play an important role and generally one can say that the most intense convection cases start in the boundary layer (Bluestein, 1993). Ho-

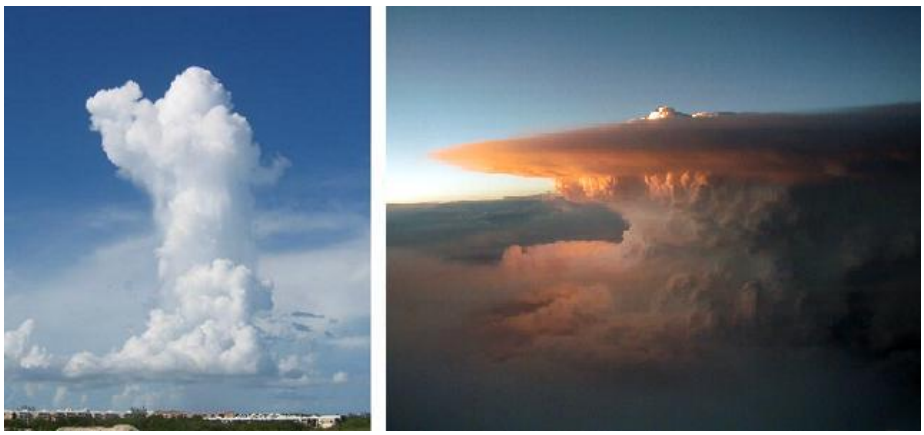

Figure 2.2: A towering cumulus cloud (left) (Lee, 2006) and a mature cumulonimbus cloud (Young, 2007).

wever, cumulonimbus clouds can also develop from altocumulus [5] or stratocumulus clouds. Altocumulus clouds are a manifestation of elevated convection, which occurs above the boundary layer (due to incoming colder air at elevated heights). Surface heating does not play any role of significance. Furthermore, cumulonimbus clouds can also be embedded in altostratus or nimbostratus clouds (Bleeker, 1980). The presence of hail, thunder or lightning classifies a large cumulus cloud as a cumulonimbus cloud (Bleeker, 1980). Thunderstorms always form from Cb clouds. If a Cb cloud reaches a height of 5 km it is very likely to become a thunderstorm (Maas, 2002). The TCu cloud develops from a well-developed cumulus cloud in which its vertical dimensions have extended more than its horizontal dimensions. It will mature into a Cb cloud under conditions of sufficient atmospheric instability. The transition of a TCu cloud into a Cb cloud can be seen by the presence of smooth, fibrous cloud edges at the top, which indicates the process of glaciation in the upper part of the cloud.

The cumulonimbus clouds can occur worldwide except in the Antarctic region, but they are most commonly found in the tropics. In the tropics warm Cb clouds are common, but most of the Cb clouds contain ice (Houze, 1993). Mature Cb clouds typically reach heights between 8 and 12 km. However, cumulonimbus clouds up to a height of 18 km have been observed in several parts of the world, e.g. Central India (Krauss *et al.*, 2007). At lower levels these clouds are composed of liquid water droplets. At higher levels mostly ice crystals are found due to the very cold temperatures at higher altitudes in the atmosphere. Individual clouds start with horizontal extents of several kilometres. Large complexes of cumulonimbus clouds, referred to as mesoscale convective systems (MCSs), can have horizontal extents of more than 100 km (Maas, 2002). The anvil shape of a mature Cb cloud can be explained by considering the tropopause ('boundary' between the troposphere and the stratosphere) as a rigid lid. In contrast to the troposphere, the temperature in the stratosphere increases with height. It is this temperature inversion at the tropopause which hinders the penetration of a vertically moving air parcel into the

[5] Alto is a Latin word meaning 'high'.

Table 2.1: Characteristics of the mean droplet size distributions for various cloud types (Liou, 1992).

Cloud Type	**Investigator**	N (cm^{-3})	r_m (μm)	Δr (μm)	LWC (g m^{-3})
St	Diem	260	4.5	0-20	0.44
Sc	Diem	350	4.0	0-12	0.09
Cu	Battan & Reitan	293	4.0	0-20	0.33
TCu	Durbin	207	3.5	0-40	0.66
Cb	Weickmann & Kampe	72	5.0	0-70	2.50

stratosphere. Instead, air is moved to the sides, creating the anvil shape. However, air parcels having enough momentum (in strong convective cases) still might penetrate the stratosphere for several kilometres, leading to the earlier mentioned observations of extremely high Cb clouds.

Between the 1940s and 1960s, extensive observational studies on droplet size distribution and liquid water content in various types of clouds have been conducted all over the world. Droplet size distributions were observed from aircrafts using a photomicrographic technique and oil-coated slides. From obtained droplet size distributions, the droplet number concentration N can be calculated (Liou, 1992).

$$N = \int_{\Delta r} n(r)dr \tag{2.4}$$

Here $n(r)$ is the number of cloud droplets n per volume per radius r. Thus $n(r)dr$ is the number of cloud droplets per volume that have radii in the interval $(r, r + \Delta r)$. From the droplet size distribution also the liquid water content can be calculated (Liou, 1992).

$$LWC = \frac{4}{3}\pi\rho_l \int_{\Delta r} r^3 n(r)dr \tag{2.5}$$

Here ρ_l is the density of liquid water. Table 2.1 gives an overview of values of the droplet size concentration, the mode radius r_m which is the radius corresponding to the peak of the droplet size distribution ($n(r)dr$) curve, the radius range Δr, and the LWC for various cloud type obtained by several investigators. The droplet size distribution varies with the position within the cloud and with time. The presented results therefore count for averaged conditions over a large volume of cloud. Results show that fair-weather cumulus clouds (Cu) have a narrow droplet size distribution compared to the TCu cloud. The Cb cloud droplet size distribution is even much broader. The droplet concentration decreases and the liquid water content increases from Cu to Cb clouds. The non-convective stratus clouds (St) and the weak convective stratocumulus clouds (Sc) are shown for comparison. These cloud types have relatively large droplet concentrations, but low liquid water contents and relatively narrow droplet size distributions.

Deep, convective clouds are associated with hazardous weather phenomena that are generally the result of phase changes of water due to great amounts of latent heat release. A cylindrical shaped cumulus cloud with a radius of 5 km and a height of 10 km contains about 8 x 10^8 kg of condensed water when assuming an average liquid water content of about 1 g m^{-3}. Given the fact that it takes about 2500 J of energy to evaporate 1 gram of water, it means that roughly 10^{14} J of latent heat energy is released when assuming a time scale of 25 minutes. This is comparable to a 25-kiloton bomb. Most of the energy is used to counteract gravity, but a part may create severe weather (Doswell, 2001). One of the most important factors for the formation of deep, moist convective clouds is the magnitude of the wind shear and the change of direction of the wind shear with height. To create severe storms, a minimum amount of wind shear is needed.

Cumulonimbus clouds can form isolated, in clusters or along fronts. An isolated cumulonimbus cloud, also called single-cell, has a relatively short lifetime of about half an hour (Bennetts *et al.*, 1986), usually develops just one main updraft and precipitation shower and occurs in atmospheric environments of low vertical wind shear (Houze, 1993). It is the most common type of thunderstorm. In the absence of significant vertical wind shear, a parcel of relatively warm air rises upward to form a vertically orientated updraft. Eventually, it will lead to the formation of precipitation particles in the form of rain, hail and/or snow that have a sufficient large size for their terminal fall speed to exceed the speed of the updraft. As the particles fall, they exert a drag force on the air within the updraft, thereby reducing its speed. In addition, rain drops may evaporate when falling out of the cloud and hail may melt during the fall, both cooling the air of the updraft and further reducing the buoyancy of the air. As a result, a downdraft, which is a mass of cold air, will form directly beneath the updraft. This mass of cold air will spread out horizontally when reaching the earth's surface, and therefore cutting of the inflow of warm (and moist) air into the updraft. The updraft will dissipate. Heavier ice particles will fall through the dissipating updraft, while smaller ice particles are transported upward and then laterally outward to form the anvil of the storm, which contains the maximum concentration of ice particles. At the end of the storm life cycle, these ice particles will slowly fall out of the anvil, aggregate and melt along the way and ultimately fall as rain with a stratiform appearance (Houze, 1993). Fig. 2.3 presents a schematic view of the three life cycles of single-cell storm: the growing stage, mature stage and the dissipating stage. The presence of a mature Cb cloud often is accompanied by lightning. Lightning is the manifestation of an electrified cloud. This means that within the cloud the positive and negative charges become separated, in which lightning is the transfer of charge between several regions within the cloud or between the cloud and the surface. Most of the lightning events occur after the cloud top rises above the -15 to $-20\,^{\circ}\mathrm{C}$ level (about 7 km). First Cloud-to-Cloud (CC) lightning occurs and after 5 to 10 minutes it is followed by Cloud-to-Ground (CG) lightning, which is less frequent (Houze, 1993). However rare, single cell storms can produce severe weather other than lightning, such as hail, downbursts (rapid, intense downward motion producing strong wind gusts at the surface) and occasionally also weak tornadoes. Usually this happens in atmospheric environments of extreme latent instability (Groenemeijer, 2003).

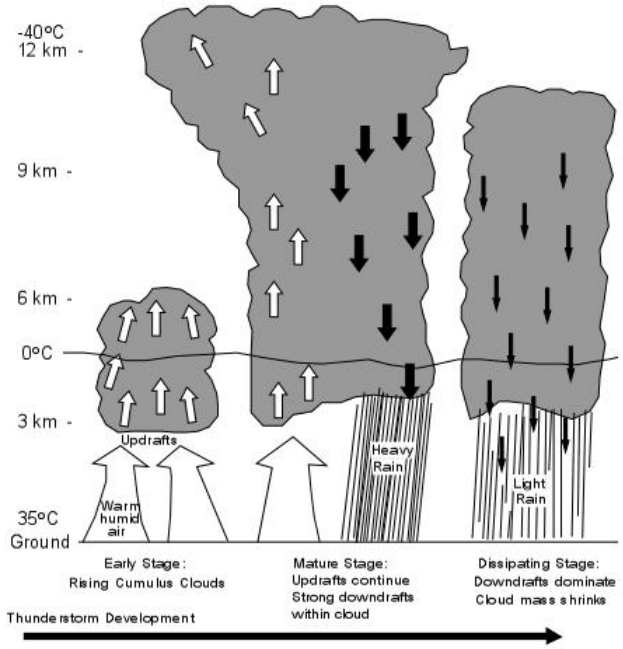

Figure 2.3: A schematic view of the three life cycles of a single-cell storm (Abbott, 1996).

When the downdraft is displaced from the updraft due to vertical wind shear, new convective cells will form along the boundary of the cold pool of air originating from an older dissipating cell. The boundary of the cold pool of air is often referred to as an outflow boundary or gust front (Groenemeijer, 2003). It typically has a depth of 500-1000 m and spreads out at a speed of about 5-10 ms^{-1} relative to the cloud (Bennetts *et al.*, 1986). Along the gust front convergence of air occurs and the warm, less dense environmental air is forced upward over the cold, dense air, inducing ascent. The forced ascending air parcel at the gust front will reach the LFC and turns into a new convective cell. This process can be noticed by observing small cumulus clouds near the base of a mature cumulonimbus cloud. If the gust front propagates slowly relative to the mature cloud, new cumulonimbus clouds can be triggered (Bennetts *et al.*, 1986)). Storms consisting of a number of cells in various stages of the life cycle are called Multi-Cell Storms or MCSs. These types of storms contain multiple convective updrafts and downdrafts. New cells have strong updrafts in which cloud particles rapidly grow into large precipitation particles. Mature cells have both an updraft and downdraft accompanied with intense precipitation. Dissipating or dying cells only consist of a downdraft and light precipitation. As with the single-cell storms, first CC lightning occurs followed by CG lightning. Lightning within a multi-cell storm can occur between regions of charge of neighbouring cells (Houze, 1993). A distinction is made between multi-cell storms that are formed of a cluster of cells called multi-cell clusters, and multi-cell storms that form of a line of cells, often referred to as squall-lines. The multi-cell cluster often consists of many single-cells, each at a different stage in

Figure 2.4: A multi-cell storm consisting of several single-cells indicated by the numbers 1 to 4, each at a different stage in the life cycle (NOAA, 2007).

the life cycle, see Fig. 2.4. The squall-lines often form along fronts or along the merged gust front of older cells (Groenemeijer, 2003). Multi-cell storms can last for several hours and sometimes the interaction of the gust front with the environmental vertical wind shear may lead to a stationary system. These types of storms than can produce extremely large amounts of localized rain over a long period of time, leading to flood events (Thorpe and Miller, 1978).

The most severe cumulonimbus cloud structure is the super-cell thunderstorm. A super-cell storm has a longer life time than single-cell storms and produces severe weather such as large hail, downbursts and tornadoes. They occur in atmospheric environments having both large CAPE and strong vertical wind shear (Emanuel, 1994). The main differences between the single-cell and the super-cell is the rotating updraft, referred to as mesocyclone, and very high vertical velocities in the updrafts and downdrafts. The very intense updraft (about 10-40 ms^{-1}), prevents the terminal fall velocity of relatively large particles to exceed the updraft speed and therefore very large hailstones can be produced. The super-cell storm is also electrically more active, producing overall lightning flash rates of 10-40 min^{-1} compared to 2-10 min^{-1} for ordinary thunderstorms (Houze, 1993). In Fig. 2.5 a schematic image of the structure of a severe super-cell is shown. The updrafts and downdrafts are indicated in red and blue, respectively. Beneath the rotating updraft a tornado has formed, which usually occurs at the beginning of the dissipating stage of the storm (Houze, 1993). At the north-east side the anvil has extended far away from the main mass of the storm due to the jet, a strong high-level wind stream in the mid-latitudes.

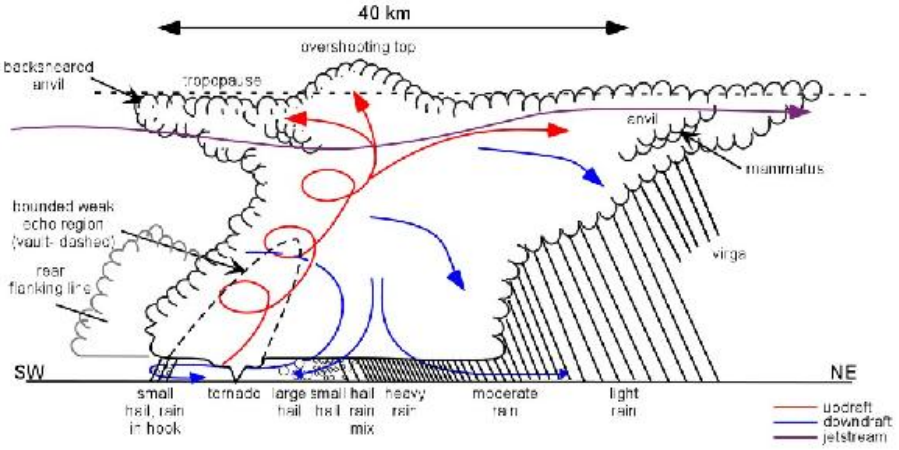

Figure 2.5: A schemtic image showing the structure of a severe super-cell storm (Kendall/-Hunt Publishing, 2002).

2.1.3 OCCURRENCE OF CONVECTIVE CLOUDS AND ASSOCIATED WEATHER IN THE NETHERLANDS

In regions having a maritime climate and no orography of significance such as in Southern England and the Netherlands, the convective instability and capping inversions are usually weak during convective events. High CAPE values are rare, still relatively large amounts of CAPE can be found in the lower part (1-3 km) of the troposphere (Browning *et al.*, 2007). High vertical wind shears occur on a frequent base in the Netherlands (Groenemeijer, 2003). However, most convective events in these regions originate from convective initiation in the boundary layer (Browning *et al.*, 2007). A characteristic outbreak of deep, moist convection occuring in the summer and leading to an isolated Cb cloud, can be described by a small layer of relatively warm and dry air beneath colder air in the middle and upper troposphere, trapping warm and moist air in the boundary layer. A parcel rising from the surface and encountering the small layer will become negative buoyant. To be able to penetrate the layer of Convective INhibition (CIN) a surface air parcel has to become warmer and/or more moist, for instance due to a diurnal trend in temperature. During the day, the surface continues to be heated by the sun and there will be a built-up of warm, moist air beneath the CIN, therefore also increasing CAPE. At some point in time the air warms and moistens so much that it becomes buoyant enough to penetrate the CIN and reach the LFC, which is usually located between 1 and 2 km. Fair-weather cumulus clouds will form. These clouds can grow into TCu clouds, which eventually can grow into Cb clouds that might become severe thunderstorms. Mesoscale forcing such as low-level convergence can lift the LCL, which makes the CIN thinner and weaker, therefore enhancing convective initiation (Browning *et al.*, 2007). Cb clouds can also form along cold fronts due to forced lifting of air along the front line (Maas, 2002). This usually leads to a lined formation of Cb clouds that travels with the speed of the overpassing front, which can be up to 70 km/h (VWKwww). They can also develop in the cold air behind a cold front due to cold air moving over a

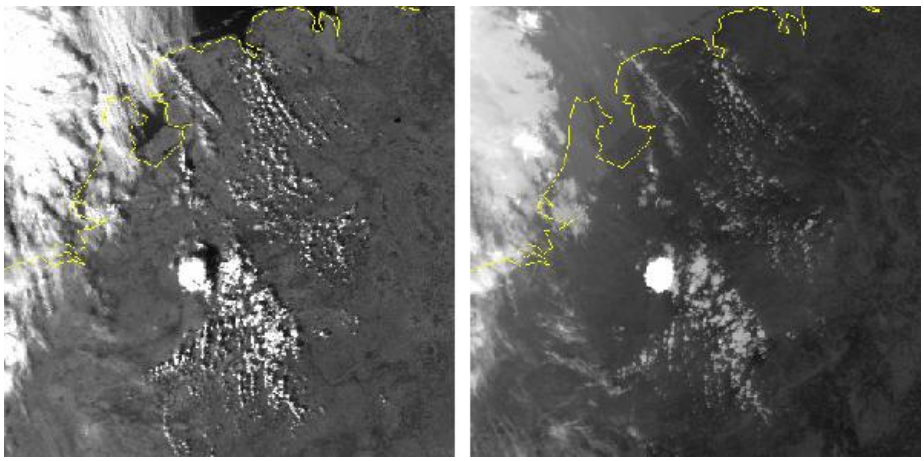

Figure 2.6: NOAA satellite visible (left) and an inverted infrared image (right) of a Cb cloud near Roermond on September 13 1999 at 14:06 UTC (Maas, 2002).

relatively warm surface. Also, occlusion fronts may trigger the formation of Cb clouds due to forced lifting of air (Maas, 2002). Although Cb clouds occur during the entire year, especially in the summer the isolated Cb clouds are responsible for most of the precipitation. During a summer day Cb clouds can produce intense showers with a rain rate of 2 mm per minute (Maas, 2002). Their horizontal size may vary between a diameter of about 5 km to diameters of 100 km, if they develop into multi-cell clusters (VWKwww). In the Netherlands they usually have a LWC of more than 0.5 gm^{-3} compared to the LWC of stratus clouds of about 0.1-0.5 gm^{-3} (Buishand and Velds, 1980).

Fig. 2.6 presents an example of a thunderstorm observed in the Netherlands. Shown are a visible and an infrared images taken on September 13 1999 14:06 UTC by the AVHRR (Advanced Very High Resolution Radiometer) instrument onboard of the American NOAA (National Oceanic and Atmospheric Administration) polar satellite having a horizontal resolution of about 1 km. Near the city of Roermond, which is in the Southeast part of the Netherlands, a cumulonimbus cloud with a diameter of about 30 km has formed. From the visible image it can be seen that the eastern part of the Netherlands is very sunny while the Western part is relatively cloudy (white colors) due to an incoming cold front from the northwest. In the East, temperatures of $31\,^{\circ}\mathrm{C}$ were reached during the day, giving rise to atmospheric instability. In the vicinity of the Cb cloud also many smaller cumulus clouds formed. From the length of the shadows in the visible image it can be clearly seen that the Cb cloud has a much larger vertical extent than the surrounding cumulus clouds. From the brightness in the (inverted) infrared image, it can be seen that the cloud top temperature of the Cb cloud is much lower (appears whiter) than the surrounding clouds, also indicating greater vertical growth.

Associated (severe) weather of Cb clouds in the Netherlands are intense showers of rain and/or hail, lightning, strong wind gusts, occasionally whirlwinds, water spouts, and even tornadoes. Thunderstorms that produce intense showers and strong wind gusts occur on a regular basis. However, severe thun-

derstorms, such as super-cell storms, which produce most of the severe tornadoes in the world, are rare. The Dutch criterion for a severe thunderstorm is a maximum total lightning intensity of at least 500 discharges per 5 minutes in an area of 50x50 km. On average, this criterion is met twice a year in the Netherlands (Schmeits *et al.*, 2006). Most lightning and large hail stones in the Netherlands, especially further inland, are observed in the summer (VWKwww).

2.2 OBSERVING CLOUDS FROM SATELLITE AND RADAR

Clouds can be observed from space using visible and infrared satellite data. From the visible and infrared satellite data, cloud physical properties can be derived and these can be used to characterize different cloud types. Especially nowcasting, detection and monitoring of (severe) convective clouds using visible and infrared satellite data has been given great attention since the use of meteorological satellites. Satellite data can be used to improve weather radar observations of precipitation or by using it as independent information outside the radar network. Furthermore, a weather radar dataset is often used as validation.

Basic physics of radiative transfer in a cloudy atmosphere will be treated in subsection 2.2.1. Subsequently, MSG and the onboard radiometer SEVIRI will be addressed in subsection 2.2.2. The process of converting satellite radiance measurements into cloud physcial properties, using the CPP algorithm and a radiative transfer model, will be explained in subsection 2.2.3. In subsection 2.2.4, radar principles will be treated.

2.2.1 RADIATIVE TRANSFER IN A CLOUDY ATMOSPHERE

The basic global energy balance of the earth is between energy that comes from the sun and energy from radiative emission from the earth and its atmosphere that is returned to space. Most absorption of solar radiation takes place at the earth's surface. However, most radiative emission takes place in the atmosphere. 99 Percent of the solar radiation consists of radiation having wavelengths in the visible (0.4-0.75 μm) and near-infrared (0.75-5 μm) part of the electromagnetic spectrum (Hartmann, 1994). Radiation at these wavelengths is also called shortwave radiation. The radiation emitted by the earth and atmosphere mainly comes from the infrared (5-200 μm) part of the spectrum and is called longwave radiation. The solar and infrared radiation at various wavelengths are shown in Fig. 2.7.

In the earth-atmosphere energy balance, clouds play a significant role by interacting with both solar and infrared radiation. The effects of clouds on solar and infrared radiation are determined by the cloud optical properties, such as cloud optical thickness and emissivity. In turn, these cloud optical properties depend on micro-physical properties, such as particle size, liquid water path and droplet concentration and on macro-physical properties, such as cloud thickness, cloud base height, cloud top height and cloud cover. The photons in a beam of solar radiation may interact with cloud particles by absorption or scattering. Absorption is the process in which the energy of the photon is taken up

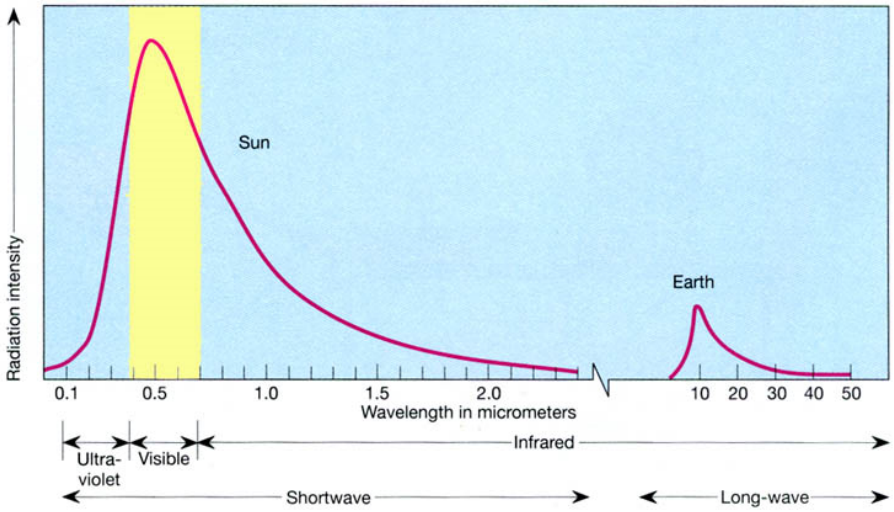

Figure 2.7: The solar and terrestrial sprectrum (McKnight, 1990).

by the cloud particle and scattering is the process in which the original direction of the photon and its energy changed into a new direction. Both processes move energy from a beam of solar radiation traversing a cloud. The intensity of the scattering process depends on the particle size. Particles with a size relatively small compared to the wavelength of the incident radiation (e.g. molecules) scatter according to the process called Rayleigh scattering (Rayleigh, 1871). For this type of scattering the scattering intensity is proportional to the inverse fourth power of the wavelength. Particles that have a comparable or relatively large size compared to the wavelength of the incident radiation, scatter according to the process called Mie-theory (Mie, 1908). It is applicable to cloud particles assuming that a cloud particle can be described as a single homogeneous sphere (of water). Because the distances between cloud particles in a cloud are much greater than the wavelength of the incident radiation, scattering of radiation from a beam by one particle may be treated independent of scattering of the same beam by other particles (Liou, 1992). The spectral dependence of the scattering intensity is much smaller, and forward scattering (in the propagation direction of the beam) is more pronounced. In the visible wavelength absorption is generally low. Therefore, photons may be scattered over 100 times before they are scattered out of the cloud. This multi-scattering process is influenced by micro and macro-physical properties of the cloud.

The energy of a beam of solar radiation is measured by its intensity or radiance ($\mathrm{Wm^{-2}sr^{-1}\mu m^{-1}}$). This holds for monochromatic light and taking into account the size area and direction of the beam. When traversing a medium like the atmosphere the intensity of the beam can be changed by scattering, absorption and emission. Scattering light out of the beam and absorption within the beam contribute to the reduction of the beams intensity. This is called extinction. Extinction can be quantified using the extinction cross-section $C_{ext,\lambda}$ (in $\mu\mathrm{m}^2$), which is the sum of the scattering cross-section $C_{sca,\lambda}$, and the absorption cross-section $C_{abs,\lambda}$, at wavelength λ. Table 2.2 shows extinction cross-sections for various cloud types at 0.5 μm. At this wavelength absorp-

Table 2.2: Extinction cross sections for several cloud types at a wavelength of 0.5 μm (Liou, 1992).

Cloud type	**Cu (fair-weather)**	**TCu**	**Cb**	**Sc**	**St**
$C_{ext,\lambda}$ (in μm^2)	165.9	468.3	481.6	120.4	473.1

tion may be neglected, so the extinction cross-section is nearly equal to the scattering cross-section. The extinction cross-section depends strongly on the droplet size distribution (compare Table 2.2 to Table 2.1). The relative importance of the extinction by scattering and by absorption is characterized by the single scattering albedo:

$$\omega = \frac{C_{sca}}{C_{ext}} \tag{2.6}$$

When only extinction processes in the beam are considered and interaction of cloud particles with monochromatic light is assumed, the reduction of intensity of a beam traversing the homogeneous atmosphere can be described by the Beer-Bouguer-Lambert law (Hartmann, 1994)

$$I_\lambda = I_\lambda(0) e^{-\tau_\lambda / \cos\theta_0} \tag{2.7}$$

in which I_λ is the intensity of the beam after traversing the atmosphere, $I_{0,\lambda}$ is the incoming solar radiation at the top of the atmosphere, τ_λ is the cloud optical thickness for wavelength λ and $\cos\theta_0$ is the cosine of the solar zenith angle. This reduced version of the general radiative transfer equation does not include a source function. From Eq. (2.7) it can be seen that the intensity of a beam traversing a homogeneous extinction medium decays exponentially, characterized by the cloud optical thickness. In a plane-parallel atmosphere, where the atmosphere is represented by infinite and horizontally uniform thin layers on top of each other, and along the vertical z-axis, this cloud optical thickness in turn is defined by

$$\tau_\lambda = \int_0^{z_{top}} k_{ext,\lambda}(z) dz \tag{2.8}$$

in which $k_{ext,\lambda}(z)$ (in m^{-1}) is the volume extinction coefficient. It is defined as

$$k_{ext,\lambda}(z) = C_{ext,\lambda} n(z) \tag{2.9}$$

where $n(z)$ (in m^{-3}) is the density of the scatterers (cloud droplets). The volume extinction coefficient is a measure of the optical density of the medium, and can be written as the sum of a scattering coefficient and an absorption coefficient.

To describe the scattering of photons by particles into various directions, so called phase functions are used. They describe the relationship between the amount of energy that is scattered at an angle Θ to the direction of the propagation of the incident radiation. A frequently used phase function for atmospheric radiative transfer applications is the analytical phase function $P(\Theta)$

written in terms of an asymmetry factor g and the scattering angle Θ (Henyey and Greenstein, 1941).

$$P(\Theta) = \frac{1}{4\pi} \frac{(1-g^2)}{(1+g^2-2g\cos\Theta)^{\frac{2}{3}}} \tag{2.10}$$

An asymmetry factor of 1 indicates only forward scattering. Cloud droplets and ice crystals usually have values of about 0.85 and 0.7, respectively. In the shortwave range (0.3-4 μm) this phase function does not work properly due to sharply peaked phase functions of realistic water droplets and ice crystals. Using Mie-theory, the phase function of spherical water droplets can be computed exactly. For scattering by ice crystals, which are non-spherical particles, the laws of geometric optics are often used to describe the angular distribution of the scattered light (Liou, 2002).

The reflectance of a cloud measured from a satellite shows spectral variation. This is due to spectral properties of clouds, Rayleigh scattering of molecules and absorption by gases in the atmosphere. Eq. (2.11) is used to calculate cloud spectral reflectances R_λ at the top of the atmosphere from measured reflected spectral radiance L_λ (in W m^{-2}sr$^{-1}\mu$m^{-1}) and spectral solar irradiance $F_{0,\lambda}$ (in W m^{-2} μm^{-1}) (Liou, 2002).

$$R_\lambda = \frac{\pi L_\lambda}{F_{0,\lambda} cos\theta_0} \tag{2.11}$$

The factor π arises from integrating the solid angle over a hemisphere. The amount of reflected spectral radiance L_λ depends on the sun-satellite geometry, which is shown in Fig. 2.8. Here, θ_0 is the solar zenith angle, ϕ_0 is the solar azimuth angle, θ is the satellite viewing zenith angle and ϕ is the satellite azimuth angle. Knowing these angles, the scattering angle Θ can be computed, which is the angle between the direction of the incoming solar radiation and the direction of the reflected solar radiation.

At thermal infrared wavelengths scattering by cloud particles is negligible, while absorption and emission dominate. Within a few scatter events most of the radiation is absorbed due to a low ω, while the remaining radiation is scattered forward due to large g. Optically thick clouds can be considered to radiate as a blackbody, which means they emit radiance B_λ near the cloud top according to the Planck function

$$B_\lambda(T) = \frac{2hc^2}{\lambda^5(e^{hc/K\lambda T}-1)} \tag{2.12}$$

where $B_\lambda(T)$ is the upwelling radiance at wavelength λ (μm) at a cloud top temperature $T(K)$, h is the Planck's constant, K is the Boltzmann's constant and c is the speed of light. An object is called a blackbody if it absorbs all radiation incident on it (Hartmann, 1994). It is the upper limit to the amount of radiation an object can emit at a given temperature.

At most infrared wavelengths, optically thin clouds can generally not be considered blackbodies. The upwelling radiance at the cloud top, I_λ, for optically thin clouds, can be described by (Roebeling *et al.*, 2008)

$$I_\lambda = \epsilon_\lambda B_\lambda(T_{cloud}) + (1-\epsilon_\lambda) B_\lambda(T_{surface}) \tag{2.13}$$

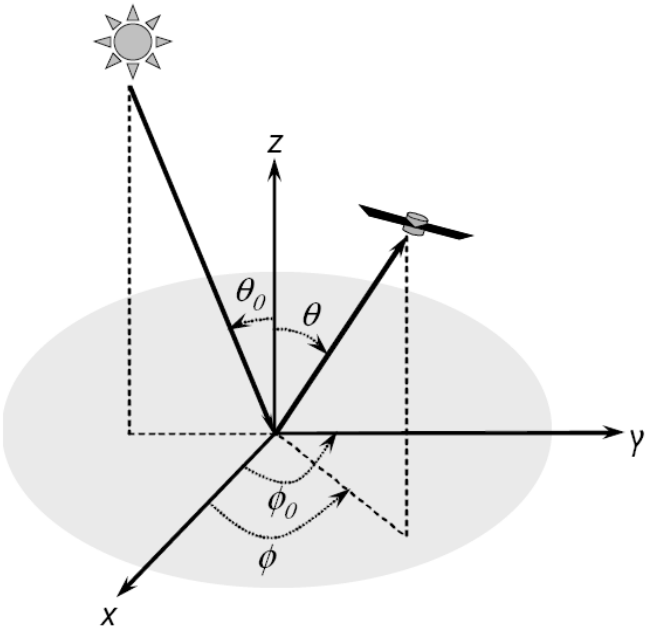

Figure 2.8: A schematic representation of the sun-satellite geometry (Roebeling *et al.*, 2008)

in which ϵ_λ is the emissivity of the cloud, $B_\lambda(T_{cloud})$ is the Planck radiance of the cloud and $B_\lambda(T_{surface})$ is the Planck radiance of the surface below, all at wavelength λ. The emissivity of an object is defined by the ratio of the amount of radiance emitted by the object to the amount of radiance the object would emit if it were a blackbody at a given wavelength. T_{cloud} and $T_{surface}$ are the brightness temperatures of the cloud and the surface, respectively. The brightness temperature is the observed temperature when assuming a surface emissivity of 1. A blackbody has emissivity values of 1 at all wavelengths. For all other objects, emissivity values range between 0 and 1. By not considering (multiple) scattering the emissivity can be approximated using the absorbing cloud optical thickness τ_λ at wavelength λ in the following equation (Minnis *et al.*, 1993)

$$\epsilon_\lambda = 1 - e^{-\tau_\lambda / \cos\theta} \tag{2.14}$$

This equation approaches 1 for clouds having a large absorption optical thickness. However, neglecting multiple-scattering may lead to an underestimation of cloud emissivity (Minnis *et al.*, 1993).

It is the analysis of the spectral differences in cloud reflectances (solar radiation) and brightness temperatures or emissivities (infrared radiation) that leads to the principle of cloud physical property retrievals for different types of clouds from satellite observations. The retrievel of cloud physical properties from SEVIRI observations will be explained in subsection 2.2.3.

2.2.2 THE MSG SATELLITE AND ONBOARD SEVIRI

Since the 1960s meteorological satellites are used in weather and climate studies. In the United States the National Aeronautics and Space Administration (NASA) and NOAA have been involved in developing and operating meteorological satellites, while in Europe the European Space Agency (ESA) and EUMETSAT operate the meteorological satellites. The first meteorological satellite (TIROS-1: Television InfraRed Observation Satellite) launched into space by NASA was a polar orbiting satellite. Polar satellites orbit at an altitude of about 800 km and pass each latitude at the same local solar time twice a day. With polar orbiting satellite data, long-term comparison and collections at consistent times are enabled. In 1974, the first geostationary meteorological satellite (GOES-1; Geostationary Operational Environmental Satellite) was launched, also by NASA. A geostationary satellite is always at the same position with respect to the rotating earth and orbits at an altitude of about 36,000 km. Geostationary satellites provide a continuous monitoring of large parts of the earth. Nowadays, tens of meteorological geostationary satellites are operated by the USA, Europe and countries such as China, India, Japan and Russia (Schmetz *et al.*, 2002). Together, the satellites form a global observation system for tropical storms, mid-latitude systems and a warning system for rapidly developing weather.

The European geostationary meteorological Meteosat satellites are a joint project between ESA and EUMETSAT. The first Meteosat satellite was launched in 1977. Since then, six other Meteosat satellites have been launched, all numbered from Meteosat-1 to Meteosat-7. In August 2002, the first satellite of the Meteosat Second generation (MSG), also called Meteosat-8, has been launched and became operational on 29 January 2004 (EUMETSAT, 2009). In December 2005, the second MSG satellite has been launched and a third and fourth satellite are expected to be launched in the years 2011 and 2013, respectively (EUMETSAT, 2009). With the new generation of Meteosat satellites, the information and observation service of the first generation has been greatly enhanced. The MSG satellites have an image-repeat cycle of 15 minutes compared to 30 minutes for Meteosat, 12 spectral channels compared to 3 for Meteosat and a sampling distance of 3 km at nadir for all channels except the high resolution channel (1km) compared to 5 km (and 2,5 km) for Meteosat. Expected operating life times of each satellite are about 7 years and together they are expected to provide service through around 2020 (EUMETSAT, 2009). Like Meteosat, MSG is a two-satellite operational service which means that two satellites will be in orbit at the same time, but one being available as a spare (Schmetz *et al.*, 2002). Furthermore they are spin-stabilized satellites, which means that they spin counter-clockwise at 100 revolutions per minute around their longitudinal axis, which is aligned with the earth's rotational axis (EUMETSAT, 2009). Both MSG satellites are located closely to where the equator meets the Greenwich meridian ($0\,^\circ$ longitude), but can be moved up to $50\,^\circ$ east and west (EUMETSAT, 2009).

The main instrument and payload on board of the MSG satellites is the Spinning Enhanced Visible and Infrared Imager, which is an optical imager radiometer observing the earth and atmosphere in 12 spectral bands. Eleven channels observe the full disk of the earth at a repeat-cycle of 15 minutes whereby

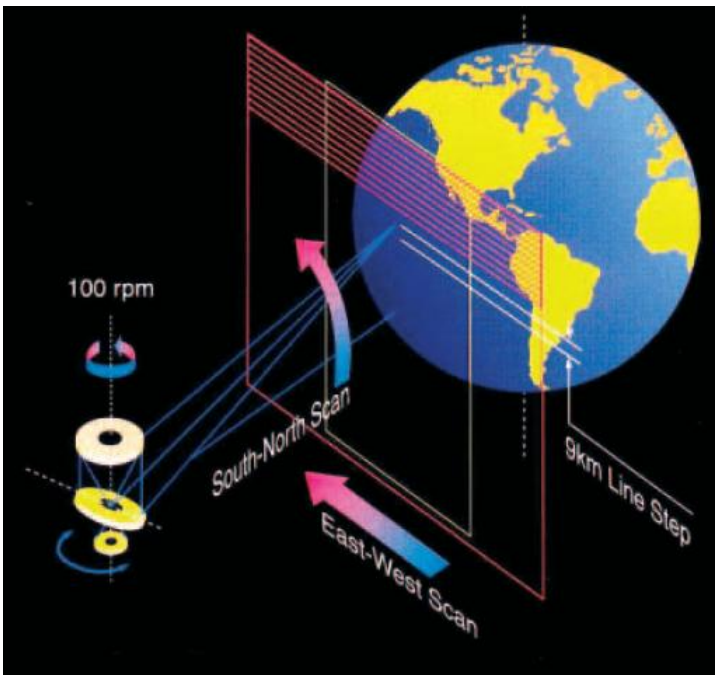

Figure 2.9: The scanning mechanism of the SEVIRI instrument (Aminou, 2002).

12.5 minutes include image acquisition and 2.5 minutes include retrace and stabilization (EUMETSAT, 2009). One channel, the High Resolution Visible channel (HRV), observes half of the full earth disk in the east-west direction and the full disk in the north-south direction. This is done in order to reduce data size. The earth disk is scanned from south to north and from east to west. The north to south scan is achieved by a scan mirror covering the earth disk with about 1250 scan lines. This means that for the eleven channels at lower resolution, an image consists of about 3750 scan lines since three detectors for each channel (nine for the HRV channel) are used together. The east to west scan is achieved by the rotational spin of the satellite mentioned before (Schmetz *et al.*, 2002). All images of SEVIRI are rectified to the 0° longitude (EUMETSAT, 2009). At nadir view the sampling distance for eleven channels is 3 km and for the HRV channel 1 km. Since the aperture angle for each Instantaneous Field Of View (IFOV) is constant, the viewing area at the surface (and therefore the sampling size) varies with the satellite viewing angle. In other words, the spatial resolution of a pixel decreases with increasing off-nadir viewing angle (Schmetz *et al.*, 2002). A complete image of the earth disk consists of 3712 x 3712 pixels for the eleven channels and 11136 x 11136 for HRV (Schmetz *et al.*, 2002). The number of scan lines can be reduced, which makes rapid scans possible. Fig. 2.9 shows the scanning mechanism of SEVIRI.

The spectral channels of the onboard SEVIRI have been selected in such a way that good information is provided on clouds, the earth's surface, water vapor, carbon dioxide and ozone. Most of these channels already have been operated before in radiance observation instruments on board of other satellites such as the AVHRR onboard NOAA and instruments on previous Meteosat satellites.

Table 2.3: SEVIRI channel characteristics; minimum, center and maximum wavelengths as well as main observational applications (Schmetz *et al.*, 2002).

No.	Channel	Spectral band Characteristics (min-cen-max λ in μm)	Main observational applications
1	VIS 0.6	0.56 - 0.635 - 0.71	Surface, clouds, wind fields
2	VIS 0.8	0.74 - 0.81 - 0.88	Surface, clouds, wind fields
3	NIR 1.6	1.50 - 1.64 - 1.78	Surface, cloud phase
4	IR 3.9	3.48 - 3.90- 4.36	Surface, clouds, wind fields
5	WV 6.2	5.35 -6.25 - 7.15	Water vapor, high level clouds, atmospheric instability
6	WV 7.3	6.85 - 7.35 - 7.85	Water vapor, atmospheric instability
7	IR 8.7	8.30 - 8.70 - 9.1	Surface, clouds, atmospheric instability
8	IR 9.7	9.38 - 9.66 - 9.94	Ozone
9	IR 10.8	9.80 - 10.80 - 11.80	Surface, clouds, wind fields, atmospheric instability
10	IR 12.0	11.00 - 12.00 - 13.00	Surface, clouds, atmospheric instability
11	IR 13.4	12.40 - 13.40 - 14.40	Cirrus cloud height, atmospheric instability
12	HRV	Broadband (0.4 - 1.1)	Surface, clouds

Table 2.3 shows all 12 channels of SEVIRI, 4 channels in the VISible (VIS) and Near-InfraRed (NIR), 8 in the InfraRed (IR) and Water Vapor (WV) and the HRV channel, with their spectral band characteristics and their main observational application.

The absorbing channels enable scientists to investigate the composition of atmospheric air masses. In the thermal channels, the contribution of an atmospheric layer to the measured radiance by the satellite is described using weighting functions. These weighting functions peak at different heights for each channel. The form of a weighting function depends on the actual atmospheric state and the satellite viewing angle (Schmetz *et al.*, 2002). Channels 1 and 2 are the two channels in the visible part of the solar spectrum. They can be used for daytime cloud, snow and ice detection due to reflected sun radiation, for land surface monitoring and for aerosol detection. Clouds can be discriminated into water and ice clouds. The visible 0.8 μm channel is more suitable for land surface and vegetation monitoring due to higher reflectances of soil and leafs, while in the 0.6 μm channel transparent clouds are better visible due to less reflectivity of the surface. In the visible channels, the cloud particle absorption is negligible and can therefore also be used to estimate cloud optical depth. In these channels there are an ozone absorption band around 0.6 μm and weak water vapor absorption lines. Channel 3 is in the near-infrared and can be used to discriminate between water and ice clouds due to stronger absorption in the ice phase at this wavelength. Also, water clouds above snow and ice can be

discriminated. Cloud particle absorption is moderate. There is a small amount of carbon dioxied absorption. The infrared channel 4 is used as a solar reflection channel as well as a thermal emission channel. It is primarily used for low cloud and fog detection (Lee *et al.*, 1997), but also to derive low level wind fields from cloud tracking (Velden *et al.*, 2000). Cloud particle absorption is strong. At night this channel in combination with channel 9 can be used to estimate cloud particle size and optical depth. There is some absorption of water vapor. The water vapor channels 5 and 6 are two channels that have water vapor as the principle absorper, but their weighting functions peak at different levels in the troposphere. They are used for water vapor and wind observations. Water vapor channels have also been used for the height location of semitransparent clouds (Nieman *et al.*, 1993). Channel 7 is an infrared channel which can be used to discriminate between water and ice clouds and to support thin cirrus cloud detection. Again water vapor is the principle absorber. Also Channel 8 is an infrared channel and an absorbing channel for ozone. It can be used to investigate ozone patterns in the atmosphere. The two infrared channels 9 and 10 are well-known split-window channels and are principally used for sea surface temperature estimations due to differential water vapor absorption at the two wavelengths. Differences in cloud emissivity are small, but might lead to differential brightness temperatures (cloud top temperature measurements) which can be used to detect thin cirrus clouds (Inoue, 1987). Furthermore, they can be used for volcanic ash clouds detection (Prata, 1989). The infrared channel 11 is an absorbing channel for carbon dioxide and can contribute to temperature information in the lower troposphere and height locating of cirrus clouds (Menzel *et al.*, 1983). The HRV channel 12 is, among others, used for improving spatial classification of clouds (Amato *et al.*, 2008). In Fig. 2.10 an example is given of four SEVIRI images of the earth in the 0.6 μm, 1.6 μm, HRV and 10.8 μm channels.

2.2.3 MSG-SEVIRI DERIVED CLOUD PHYSICAL PROPERTIES

Over the last couple of decades, a number of methods have been developed to derive cloud physical properties from satellite measurements. The common principle of these methods is that the cloud reflectances in the visible wavelength (0.6 or 0.8 μm) are primarily a function of Cloud Optical Thickness (COT)and that the cloud reflectances in the near-infrared wavelength (1.6 or 3.9 μm) are primarily a function of particle size (Nakajima and King, 1990). The differences in the methods mainly lie in the choice of satellite they were designed for, the visible and near-infrared wavelengths and the iteration and interpolation schemes used. Radiative transfer model simulations are used to relate observed radiances to cloud physical properties. Several models, based on different methods such as the Monte Carlo RTM (Macke *et al.*, 1999), Discrete Ordinates RTM (Stamnes *et al.*, 1988) and the Doubling-Adding KNMI —(DAK) RTM (De Haan *et al.*, 1987; Stammes, 2001) have been developed to approximate or solve the radiative transfer equation in a plane-parallel atmosphere. The RTM cloud reflectance simulations made with predefined cloud physical properties and viewing geometry are used to generate Look Up Tables (LUTs). Once generated, these LUTs can be used to compare the simulated reflectances to the satellite observed reflectances and to translate them into cloud

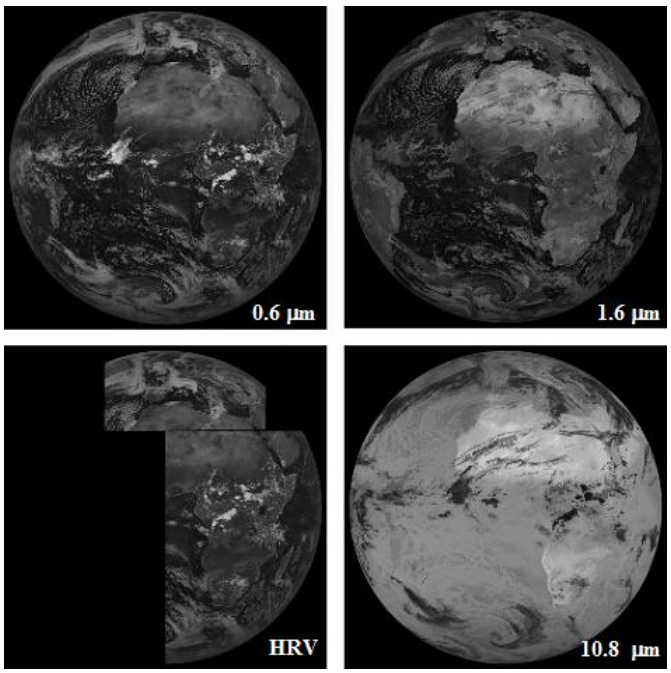

Figure 2.10: SEVIRI scan images of the earth in the 0.6 μm, 1.6 μm, HRV and 10.8 μm channels (EUMETSAT, 2009).

physical properties. In this study the cloud optical thickness, effective radius (REFF) and liquid water path (LWP) are retrieved from MSG-SEVIRI measurements using the DAK radiative transfer model and the CPP algorithm (Roebeling *et al.*, 2006).

The CPP algorithm is a two-step approach to retrieve cloud physical properties from visible and near-infrared satellite reflectances. The first step is to separate cloudy pixels from non-cloudy pixels in satellite images. Cloudy pixels are pixels that are (partly) filled with clouds. The algorithm used to separate these pixels is based on the MODIS (MODerate-Resolution Imaging Spectroradiometer, onboard of the Terra and Aqua satellites) cloud detection algorithm (Platnick *et al.*, 2003), but some modifications have been made for the SEVIRI cloud detection algorithm. The cloud detection algorithm does not depend on ancillary information, such as atmospheric profiles and surface temperature. After cloud pixel testing, a cloud mask is generated having four confidence levels: clear certain, clear uncertain, cloud uncertain, cloudy certain (Roebeling *et al.*, 2006). The second step is to relate the reflectances of cloudy pixels (cloudy certain and cloudy uncertain) to cloud physical properties by utilizing DAK. The CPP algorithm uses visible (0.6 μm) and near-infrared (1.6 μm) wavelengths to retrieve cloud optical thickness and particle size, respectively. Particle size will be measured in terms of the effective radius, which will be explained later on in this subsection. The retrieval of particle size from the 1.6 μm wavelength is weighted towards the upper part of the cloud (Platnick, 2001). This is due to the fact that the degree of penetration of photons into the cloud depends on wavelength, particle type and particle size. For optically thick clouds (COT $>$

8), the reflectance at 1.6 μm is mainly a function of particle size. For optically thin clouds (COT < 2) the 3.9 μm wavelength would be more appropriate to retrieve particle size. However, this wavelength has several disadvantages: at 3.9 μm the radiance consists both of reflected solar radiation and emitted thermal radiation, a low signal to noise ratio that increases the retrieval uncertainties and a less representative value for optically thick clouds, because the retrieval represents the particle size of the upper part of the cloud. Therefore, for optically thin clouds a climatologically averaged effective radius of 8 μm for water clouds and 26 μm for ice clouds is used (close to values used by Rossow and Schiffer (1999)). A weighting function is used to smooth the transition between the assumed effective radius and the observed effective radius.

The retrieval of COT and particle size is done in an iterative manner, which means that satellite observed reflectances at the two wavelengths are repeatedly compared to LUTs of the DAK simulated reflectances for predefined COT and particle size (Jovilet and Feijt, 2003). During this process, the retrieved COT at the 0.6 μm channel is used to update the retrieval of the particle size at the 1.6 μm channel and the iteration continues until both cloud physical properties converge to stable values. In the LUTs, values for COT are interpolated using polynomial interpolation and values for particle size are interpolated using linear interpolation.

Another cloud physical property which can be retrieved from satellite data is the Cloud Top Temperature (CTT). In the CPP algorithm the CTT is derived from the 10.8 μm Brightness Temperature (BT) and the emissivity of the cloud ϵ_λ. The brightness temperature is the apparent observed temperature assuming a surface emissivity of 1 (Roebeling *et al.*, 2006). For optically thick clouds, the brightness temperature can be regarded as the thermodynamic temperature of the upper part of the cloud in which the emissivity approaches a value of 1. For optically thin clouds having lower emissivity values, the observed brightness temperature also has a contribution from upwelling radiation from the surface below, see Eq. (2.13). The 10.8 μm brightness temprature is corrected for using the cloud (absorbing) optical thickness, $\tau_{10.8}$. It is related to the cloud (scattering) optical thickness that is obtained directly from visible reflectance measurements. The cloud (absorbing) optical thickness is derived as follows (Minnis *et al.*, 1998)

$$\tau_{10.8} = \tau_{0.6} \frac{Q_{10.8}}{Q_{0.6}} \tag{2.15}$$

in which $Q_{10.8}$ and $Q_{0.6}$ are the extinction efficiency factors at 10.8 and 0.6 μm, respectively. The extinction efficiency factors are normalized extinction cross-sections, which means that the extinction cross-section is divided by the area of a particle having radius r, πr^2.

To discriminate between water and ice clouds (thermodynamic phase), a consistency test of observed differences in cloud reflection at 0.6 and 1.6 μm is used, as well as a threshold test of the 10.8 μm brightness temperature. The consistency test compares observed and simulated differences in cloud reflectance at the two wavelengths. These differences arise from stronger absorption by ice particles than water particles at the 1.6 μm wavelength (Jolivet and Feijt, 2003). Cloudy pixels are labeled as ice clouds when they are identified as ice clouds by the consistency test and have a cloud top temperature below 265 K.

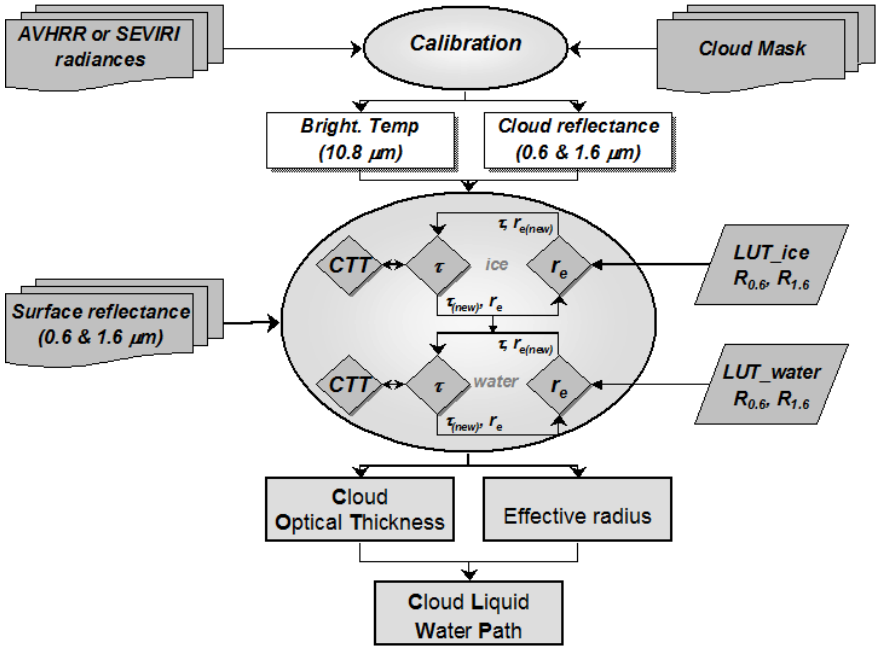

Figure 2.11: Flowchart of the CPP algorithm (Roebeling *et al.*, 2006).

All other cloudy pixels are labeled water clouds.

From the COT at 0.6 μm (τ_{vis}) and the effective radius, the liquid water path (LWP) can be calculated using the following equation (Stephens *et al.*, 1978), assuming a fixed vertical profile of the liquid water content.

$$LWP = \frac{2}{3}\tau_{vis} r_e \rho_l \tag{2.16}$$

Here, ρ_l is the density of liquid water. The (scattering) cloud optical thickness in the visible τ_{vis} is related to the (absorbing) cloud optical thickness in the infrared τ_{ir} and depends on particle size and thermodynamic phase. For large water and ice particles $\tau_{ir} \sim 0.5\ \tau_{vis}$ (Roebeling *et al.*, 2006).

Fig. 2.11 presents the flowchart of the CPP algorithm, which starts at the top with satellite measured radiances combined with a cloud detection scheme to create a cloud mask. For cloudy pixels, the 0.6 and 1.6 μm reflectances and the 10.8 μm brightness temperature are calculated. Using LUTs for both water and ice clouds, the measured reflectances are compared to retrieve COT and r_e. During an iteration process (indicated by the arrows in the center circle of the figure) the retrieved COT is used to update the r_e and to calculate the CTT until the cloud physical properties converge to a stable value. Finally, using the retrieved COT and r_e, the LWP can be calculated.

The DAK radiative transfer model is developed for narrowband multiple scattering calculations at the visible and near infrared wavelengths in a plane-parallel and multi-layer Rayleigh scattering atmosphere, containing plane-parallel and horizontally homogeneous clouds over a Lambertian surface. It solves the radiative transfer equation for solar radiation in the atmosphere mo-

nochromatically and takes polarization into account. Thermal emission, 3D cloud effects, multi-layer cloud effects and aerosols in the atmosphere are not taken into account. DAK starts with the calculations for reflection and transmission of an optically thin layer in which no more than two scattering events are allowed to occur. With this restriction, the radiative transfer equation can be solved analytically. Next, another identical layer is placed on top of the previous layer and the reflection and transmission of the combined layers are calculated by computing successive reflections back and forth between the two layers. This is called the doubling procedure and is continued until the actual optical thickness of the cloud is reached.

To describe the size distribution of the water particles in the clouds a modified gamma distribution is used, which is defined by the effective radius r_e and the mean effective variance ν_e. They are shown in Eq. (2.17) and Eq. (2.18) (Hansen and Hovenier, 1974). The particles in water clouds are assumed to be spherical droplets.

$$r_e = \frac{\int_0^\infty r^3 n(r) dr}{\int_0^\infty r^2 n(r) dr} \tag{2.17}$$

$$\nu_e = \frac{\int_0^\infty (r - r_e)^2 r^2 n(r) dr}{r_e^2 \int_0^\infty r^2 n(r) dr} \tag{2.18}$$

Here $n(r)$ is the size distribution of the particles and r is the radius of a particle. The effective radius is the parameter that represents the radiative properties of a size distribution of cloud droplets. The effective variance is a measure of the width of the distribution. In the generated LUTs the water particles in clouds are assumed to have effective radii between 1 and 24 μm and an effective variance of 0.15. For ice clouds a homogeneous distribution of imperfect hexagonal ice crystals type Cb, C1, C2 and C3, which are characterized by their Length (L), diameter (D) and volume equivalent effective radius r_e, is assumed (Hess *et al.*, 1998). They have volume equivalent effective radii between 6 and 51 μm.

The DAK simulations are first done for a black surface. The measured reflectances $R(\alpha_s)$ at 0.6 and 1.6 μm also have a contribution from the surface α_s, which is computed using the following equation (Chandrasekhar, 1960)

$$R(\alpha_s) = R_0 + \frac{\alpha_s t(\theta_0) t(\theta)}{1 - \alpha_s \alpha_A} \tag{2.19}$$

in which R_0 is the atmospheric reflectance above a black surface, $t(\theta_0)$ and $t(\theta)$ are the atmospheric transmission at the solar and viewing zenith angle, respectively, and α_A is the hemispherical sky albedo for upwelling isotropic radiation. Over land, a surface albedo map generated from MODIS white-sky albedo (bi-hemispherical reflectance in the absence of a direct component) data over one year is used, which is a good approximation of the surface albedo below optically thick clouds (Moody *et al.*, 2005). Over ocean, a surface albedo of 0.05 in both wavelengths is assumed (Roebeling *et al.*, 2006). Table 2.4 demonstrates the settings used in the DAK simulations to create the LUTs. The model for the mid-latitude summer was taken from Anderson *et al.* (1986) and the imperfect hexagonal ice crystals are taken from Hess *et al.* (1998).

Parameter	*Settings*				
Vertical profiles of pressure, temperature, and ozone	Midlatitude summer [a)]				
Aerosol model	none				
Cloud height	1000 - 2000 m				
Solar zenith angle (θ_0)	0 - 75°				
Viewing zenith angle (θ)	0 - 75°				
Relative azimuth angle (ϕ)	0 - 180°				
Cloud Optical Thicknesses	0 - 128				
Surface albedo (ocean)	0.05 (0.6 μm), 0.05 (1.6 μm)				
Surface albedo (land)	Modis white sky albedo [b)]				
	water clouds	*ice clouds*			
Cloud particle type	Spherical water droplet	Imperfect hexagonal ice crystal [c)]			
Cloud particle size	1 –24 μm	Type	D (μm)	L (μm)	r_e (μm)
		Cb	4.0	10.0	6.0
		C1	10.0	30.0	12.0
		C2	22.0	60.0	26.0
		C3	41.0	130.0	51.0
Size distribution	Modified gamma	-			
Effective variance (v_e)	0.15	-			

Table 2.4: Characteristics of the atmosphere and surface as well as sun-satellite geometry and cloud physical property intervals used to generate LUT's with DAK (Roebeling *et al.*, 2005).

Fig. 2.12 shows DAK simulations of 0.6 and 1.6 μm reflectances for water clouds and ice clouds. The slanted lines of COT values of 2, 4, 8 and 16 in the figure show that for optically thin clouds both the 0.6 μm and 1.6 μm depend on the COT. For optically thick clouds, the lines of COT values are almost vertically orientated and nearly perpendicular to the lines of effective radius values, showing little dependence on 1.6 μm reflectances and therefore reliable retrievals of particle size.

Roebeling *et al.* (2005) studied the sensitivity in radiative transfer calculations on cloud physical property retrievals. Differences arise due to different methods used to solve the radiative transfer equation and different iteration and interpolation schemes. Due to a nonlinear relationship between cloud properties and observed reflectances and the retrieval of cloud properties, small errors in simulated reflectances can result into larger errors in retrieved cloud physical properties. Four well-known RTMs were compared including DAK and the Monte Carlo method and relative mean differences of less then 3 % were found. From the simulation including the 3% error, the cloud optical thickness and droplet effective radius sensitivity were analyzed channel-wise. It showed that especially for thick clouds (COT $>$ 60) errors in the retrieved cloud optical thickness can increase up to 30% using a 3% error in 0.6 μm reflectances. The errors in the retrieved droplet effective radius were relatively small. However,

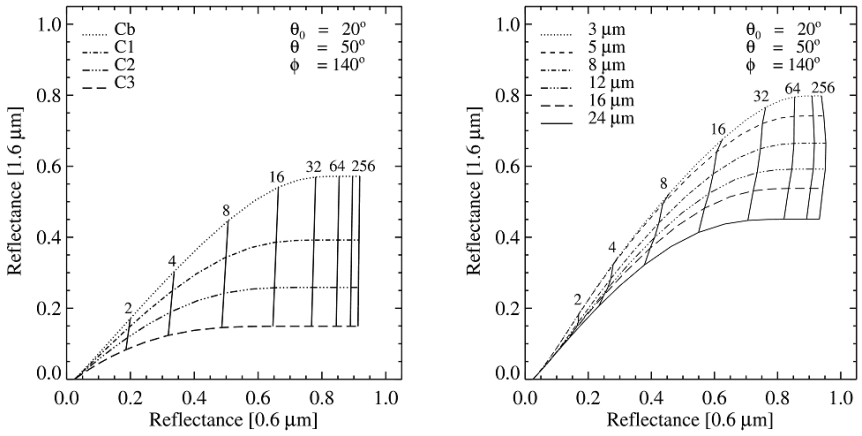

Figure 2.12: DAK simulations of 0.6 μm reflectances versus 1.6 μm reflectances for ice (left) and water clouds (right) (Roebeling *et al.*, 2005).

the accuracy of the retrieved cloud physical properties is also determined by other sources of error such as instrument calibration and cloud top elevations that strongly affect the observed visible and infrared signal (Hees and Lelieveld, 2000).

2.2.4 RADAR PRINCIPLES

A Radar (RAdio Detection And Ranging) is a type of radiometer instrument that uses electromagnetic waves to identify the range, altitude, direction and speed of objects. Since the end of World War II, radars have become available for meteorological research. From early on, successive radar images have been used to determine the motion of precipitating systems and to extrapolate their path into the future (Ligda, 1953). Radars can detect the most active convective cores within thunderstorms by looking at the intensities of the reflectivity factor in precipitation echoes. Also the shape of the area of the echo and its horizontal and vertical extents are used for convective storm identification and monitoring. Furthermore, Doppler radars can be used to monitor storm dynamics, such as mesocyclones. In contrast to satellites, developing convective activity can not be detected by radar until the precipitation stage has been reached. Also, radar networks that provide more than a local coverage are still limited to Western-Europe and North-America and even there the spatial coverage is limited due to ground shielding. However, radars do provide information about vertical profiles within clouds, while satellite data mostly contain information about the upper part of the cloud.

Weather radars transmit short pulses of electromagnetic energy from an antenna into the atmosphere. The signal travels at the speed of light until it hits a target and returns back to the antenna. Modern radars usally use one antenna to transmit and receive the signal. Most radar antennas rotate about a vertical axis aiming at the horizontal, but meteorological radars can also aim

Table 2.5: Radar bands, their associated frequencies and detectable hydrometeors (Walther, 2008).

Radar Band Designation	**Nominal Frequency**	**Appropriate meteorological scatterers (hydrometeors)**
L	1-2 GHz	
S	2-4 GHz	large precipitation droplets
C	4-8 GHz	precipitation
X	8-12 GHz	precipitation and cloud droplets
K_u	12-18 GHz	small precipitation and cloud droplets
K	18-27 GHz	cloud droplets
K_a	27-40 GHz	cloud droplets
V	0-75 GHz	cloud droplets
W	75-110 GHz	small cloud droplets

their antenna into the vertical. Weather radars have horizontal ranges of several hundreds of kilometers and a vertical range of several kilometers. They transmit their signal pulses at a rate varying from several hundreds of Herz to several thousends of Herz and can transmit signals of more than 1MW of power and receive powers as small as 10^{-14} W. The frequency of the electromagnetic signal varies from about 100 MHz to 100 GHz (Rinehart, 2006). Radars operating at lower frequencies do not experience a lot of signal attenuation, which is the reduction of power that any electromagnetic radiation experiences traversing a medium. The radiation beam can be attenuated by molecules in the atmosphere (relatively small), clouds and precipitation particles (Rinehart, 2006). However, to be able to operate at low frequencies, radars need quite big antenna dishes and large amounts of power. At higher frequencies attenuation effects increase, but radars require less power. Most weather radars work in so called X-band, S-band or C-band, which are shown in table Table 2.5. In North-America the standard is S-band, while for Europa mostly C-band weather radars are used (Walther, 2008).

At the physical basis of weather radars lies the radar equation. It can be applied to any radar, provided the spherical targets meet the Rayleigh scattering assumption. The amount of power that returns to the antenna, P_r, is given by

$$P_r = \frac{\pi^3 P_t G^2 \theta \phi h |K|^2 l}{1024 \ln(2) \lambda^2} \frac{z}{r^2} \tag{2.20}$$

in which P_t is the transmitted peak power, G is the gain of the antenna, θ and ϕ are the horizontal and vertical beamwidth, λ is the wavelength of the transmitted energy, h is the pulse length, l is the loss factor due to attenuation, $|K|^2$ depends on the dielectric constant of water or ice and r is the target range of the precipitate. All these variables are either known or can be measured directly. Events such as multiple scattering, mixed water phase of the targets and a partially or inhomogeneous filled radar beam are not accounted for in the equation (Walther, 2008). The primary interest of radar meteorologists is the radar reflectivity factor z and it is solved mathematically by the radar. In radar

Table 2.6: Derived empirical constants A and b using the typical $Z = AR^b$ relation, for several precipitation types (Walther, 2008).

Source	Precipitation type	a	b
Joss and Waldvogel (1990)	Stratiform	300	1.6
Rosenfeld et al. (1993)	Tropical Rain	250	1.2
Marshall and Palmer (1948)	Stratiform	200	1.6
Fujiwara (1969)	Thunderstorm	486	1.37

meteorology the radar reflectivity factor z (in mm^6m^{-3}) is used to describe the intensity of the measured signal that returns to the antenna. It is determined by the number and size of the particles and therefore is independent of the radar. Due to the wide range of values it can obtain, a logarithmic radar reflectivity factor Z (in dBZ) is used for convenience. For fog this reflectivity factor can become as small as -30 dBZ, while for large hail stones it can become as large as 75 dBZ (Rinehart, 2006). A radar image displaying the measured radar reflectivities within an area is called an echo. Non-precipitating clouds may be hard to detect due to the fact that the cloud droplets are too small to give rise to measurable reflectivity values. Rain, however is easy to detect. It should be noted that small droplets, even if they outnumber the larger drops by several magnitudes, contribute almost nothing to the reflectivity compared to the larger dropws. This is caused by the to-the-sixth-power dependence on the diameter of spherical targets in the calculation of the reflectivity.

There is a relation between the reflectivity and the rain rate and since several decades various Z-R relationships have been developed. Most of the Z-R relationships are of the mathematical form

$$z = AR^b \tag{2.21}$$

in which R is the rainfall rate (usually in mm/h), z is the radar reflectivity factor (in mm^6m^{-3}) and A and b are empirical constants. The empirical constants can be derived from calculating both radar reflectivity and rainrates from measured drop-size distributions.

Table 2.6 shows Z-R relationships for various precipitation types. The most commonly used drop-size distributions and Z-R relationship are the ones developed by Marshall and Palmer (1948).

$$z = 200R^{1.6} \tag{2.22}$$

Rain reflectivity factors vary from 20 dBZ to about 50 dBZ. Reflectivity factors higher than 55 dBZ are usually associated with hail (Rinehart, 2006).

Most weather radars also provide direct measurements of the speed of the targets moving away or towards the radar using the Doppler effect. Just as with a frequency shift of sound due to relative motion of the source and the listener, electromagnetic radiation will show a frequency shift for a relative motion of the radar and the targets. For a given radar, the amount of the frequency shift

only depends on the radial component of the velocity of the target. The distance a signal has to travel towards the target and back to the radar (2r) can be measured in wavelengths or radians. A phase shift in a given interval of time is a frequency shift. Within the radar, the phase of the received signal is compared to the phase of the transmitted signal to determine the amount of phase shift. This phase shift is translated into a radial velocity of the echo. The maximum phase shift is $\pm \pi$ radians and leads to a maximum velocity a Doppler radar can detect unambiguously, also called Nyquist velocity, and a maximum radar range.

3rd Chapter
SATELLITE CONVECTIVE CLOUD STUDIES

After the launch of the first geostationary meteorological satellite (GOES-1) in 1974, American scientists used the 30 minutes sequences of visible and infrared images to study convective initiation and the various convective systems such as thunderstorms and large mesoscale convective systems that may arise from it. However in 1969, Fujita already used the ATS (Application Technology Satellite), launched by NASA primarily to test out new technology in space communication, to derive cloud motion. Purdom (1976) concluded after a study of convective activity using GOES-1, that the high-resolution imagery (8 km for infrared and 1 km for visible) from the satellite could be used subjectively to detect the initiation and maintenance of convective systems by monitoring convergence lines, revealed by a thin line of cumulus clouds. From early on, attention has been given on combining satellite data and other sources of meteorological information, especially radar, for monitoring convective activity and forecasting severe weather.

3.1 IR AND VIS THRESHOLDS

In the 1970s and 1980s, much of the focus was on convective rainfall estimations on larger scales, especially convective precipitation in the tropics. IR and VIS data were used to define cloud types causing rain. Mainly IR-based methods were developed to make a distinction between convective and stratiform cloud areas in satellite imagery. The cloud areas then give information about the convective activity of the precipitation systems and help to identify regions that might be affected by hazardous weather. Principally, a relationship between cloud top temperature and cloud top height is assumed, as well as a relationship between cloud top height and the amount of precipitation. The simplest method is using fixed IR thresholds which yield the best relationship between cloud top brightness temperatures (BTs) in satellite imagery and ground-based rainfall observations (Arkin, 1979; Negri *et al.*, 1984; Adler and Negri, 1988). The Convective-Stratiform Technique (CST) of Adler and Negri (1988) first identifies local brightness temperature minima (very cold pixels) in the IR image. Then the slopes from the local brightness temperature minima are cal-

culated. Large slopes are associated with convective cores, while small slopes are associated with cirrus clouds. Using an empirical function (derived from a 1-dimensional cloud model), rain rate and convective rain area are calculated from the local brightness temperature minima. The results were compared to radar echoes. Convective rain fields from the CST technique were most similar to radar echoes for young, isolated storms. King *et al.* (1995) compared an IR-based technique, the GOES precipitation index GPI (Arkin and Meisner, 1987), to a technique that also includes VIS data, the supervised classification procedure RAINSAT (Lovejoy and Austin, 1979; Hogg, 1990; King *et al.*, 1989). The estimated rainfalls from these techniques were validated against radar and surface gauge data in Japan. The GPI technique assumes that all pixels colder than a Brightness Temperature (BT) of 235 K precipitate at a constant rate of 3 mmh^{-1} and was developed for rainfall estimations in the tropics. The RAINSAT technique was calibrated using radar data from southern Ontario. It does not show any significant rainfall for cloud albedos less then 0.5. It shows rapidly increasing rain rates above cloud albedos of 0.7 when only the VIS rain rate relationship is considered. The IR-only relationship shows a rapid increase in rain rates for temperatures colder than 220 K. Considerable improvement, especially a decrease in false alarm rate, can be achieved when VIS data is included. The VIS data is especially helpful in filtering out cirrus clouds. These clouds have cold cloud top temperatures, but appear transparent in the VIS images. However, during the night this VIS data is not available.

3.2 MULTI-SPECTRAL IR AND WV THRESHOLDS

Cirrus clouds can also be identified using the brightness temperature difference (BTD) between the 11 μm and 12 μm channel. These clouds show large values of BTD due to different emissivities in the wavelengths. Inoue (1985) identified cirrus clouds using a BTD_{11-12} of more than 2.5 K. Kurino (1997) found that a BTD_{11-12} of more than or equal to 3 K corresponds to cirrus with no rain. These multi-spectral techniques, also called split channel/window techniques, were first used on polar data (AVHRR), since the old geostationary satellites only had one VIS, IR and WV channel. Fig. 3.1 shows a cloud classification scheme based on two thresholds (Inoue, 1987). The height classification of the clouds is based on a BT threshold and on a BTD threshold. Clouds below a BT of $-20\,^{\circ}\mathrm{C}$ are high level clouds. The BDT of optically thick clouds, such as cumulonimbus clouds features $0\,^{\circ}\mathrm{C}$. Also the BTD of an IR and a WV channel are used in convective cloud studies. The BT in the water vapour over deep convective clouds is often higher than the BT in the infrared (Schmetz *et al.*, 1997; Tjemkes *et al.*, 1997). It is related to the presence and amount of stratospheric water vapor. The water vapour absorbs radiation emitted from the cold cloud top and emits it at a stratospheric temperature, which is usually higher than those at the top of the troposphere. Kurino (1997) documented that areas with $\mathrm{BT}_{11-6.7}$ less than or equal to 0 K correspond to deep convective clouds with heavy rain. Amorati *et al.* (2000) have related positive BDT values to the rainfall amount for deep convective storms in Northern Italy.

Fixed thresholds for VIS reflectances and NIR, IR or WV BTs or BTDs are usually designed in a specific context (synoptic/seasonal situation). There-

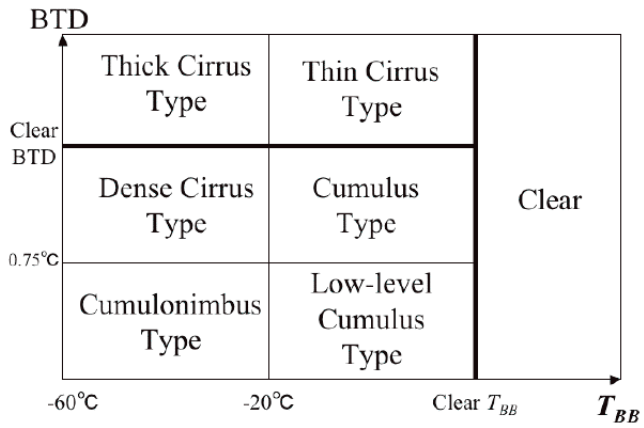

Figure 3.1: A cloud classification scheme using a brightness temperature threshold and a brightness temperature difference threshold (Inoue, 1987)

fore, the methods that use fixed thresholds may not be reliable for cloud/-precipitation classification and rainfall estimates outside this context. A coupling to ancillary data makes thresholds dynamical. Zinner *et al.* (2008) use the temperature of the tropopause determined by ECMWF model analysis for an adaptive threshold, T_{trop}-1.5 K for the WV channel, to find cloud tops near-tropopause heights. Clouds with near-tropopause heights are considered to be mature convective clouds. In the Enhanced Convective-Stratiform Technique (ECST), Reudenbach *et al.* (2001) use numerical model data, such as vertical profiles of temperature and humidity, for a better adjustment to the actual atmospheric situation.

3.3 SATELLITE DERIVED CLOUD PHYSICAL PROPERTIES

Multi-spectral techniques can also be used to derive optical and micro-physical cloud properties for upper cloud parts. In turn, these cloud physical properties can be related to cloud types and can therefore be used to improve cloud/precipitation classification and rainfall retrievals. Rosenfeld and Gutman (1994) used AVHRR channels 0.65 μm, 3.7 μm, 10.8 μm and 12.0 μm to derive cloud top properties and to relate them to the precipitation potential of clouds. The general idea is that tops of raining clouds reflect little solar radiation in the NIR 3.7 μm due to larger water droplets and ice particles in the upper part of the cloud. It was shown that optical thick clouds with an effective radius larger than 14 μm can be related to radar reflectivities that indicate precipitation. Rosenfeld and Lensky (1998) investigated the evolution of the effective radius with cloud top temperature (or cloud top height) to gain more insight on precipitation forming processes in convective clouds using AVHRR imagery. They developed a technique (RLT) based on two assumptions. The first states that the evolution of cloud top effective radius r_e with temperature T, observed by a satellite at a given time (snapshot) for a cloud ensemble, is similar to the $r_e - T$ time evolution of one specific cloud. This exchangeability between time and

space domains is called the ergodicity assumption. The second assumption states that the r_e in the upper part of the cloud is similar to the r_e well within a cloud at the same height, as long as no precipitation falls through that cloud volume. The second assumption is verified using in situ aircraft measurements (Rosenfeld and Lensky, 1998), while the first assumption is verified using rapid scan SEVIRI imagery of convective clouds over Africa (Lensky and Rosenfeld, 2006). The $r_e - T$ relations of a convective cloud field is stable over time and depends mainly on the thermodynamic state of the air mass and the present type and amount of aerosols. Thies *et al.* (2008) use the cloud top height, cloud water path and cloud phase in upper cloud parts to separate rainfall areas into sub areas of different precipitation processes and rainfall intensities. The rain area is separated into sub areas of convective and advective-stratiform precipitation using a pixel-based confidence function. The confidence function is determined by comparing the values of VIS, NIR and IR channels and IR and WV channel differences to ground-based radar observations. Subsequently, these sub areas are divided into sub areas of differing rainfall intensities. Classification of convective precipitation sub areas is based on the conceptual model that convective rain clouds with high rainfall intensities are characterized by a larger vertical extension and a cloud top reaching higher into the atmosphere. This is used to establish a relationship between cloud top temperature and rainfall probability and intensity. Classification of advective-stratiform precipitation sub areas is based on the conceptual model that advective-stratiform rain clouds with higher amounts of cloud water path and higher amounts of ice particles in the upper part of the cloud have higher rain intensities.

3.4 CONVECTIVE CLOUD FEATURES AND PATTERN RECOGNITION TECHNIQUES

Deep convective clouds show (above) cloud top features and patterns, such as cold-U/V shaped features (McCann, 1983) and plumes (Setvák and Doswell III, 1991), that can be recognized in VIS, NIR, IR and WV channels. Fujita (1981) was the first to describe significant cloud top structures, usually related to super-cell storms, using IR imagery. The plume-like shapes that are typically located downwind from the coldest cloud top and from that point expand (Levizzani and Setvák, 1996), show increased cloud top reflectivities in the 3.7 or 3.9 μm channels. This enhanced reflectivity may arise from very small ice crystals that are lifted up above the cloud top anvil, which has larger and therefore heavier ice crystals (Melani *et al.*, 2003). The BTD between WV and IR show positive values which might be caused by pumping of water vapour above cloud top heights. The BTD field is very closely related in a spatial sense to the 10.7 μm BT field. Highest BTD values were found above the coldest BT areas. Setvák *et al.* (2003) suggest a link between the observed plumes and warm wakes in the cold U/V signatures. Both features can be considered to be possible indicators for long-lasting storms such as super-cells. Fig. 3.2 shows satellite images of a severe storm with a plume originating from the warm area.

Pattern recognition can be done in an advanced manner using statistical clas-

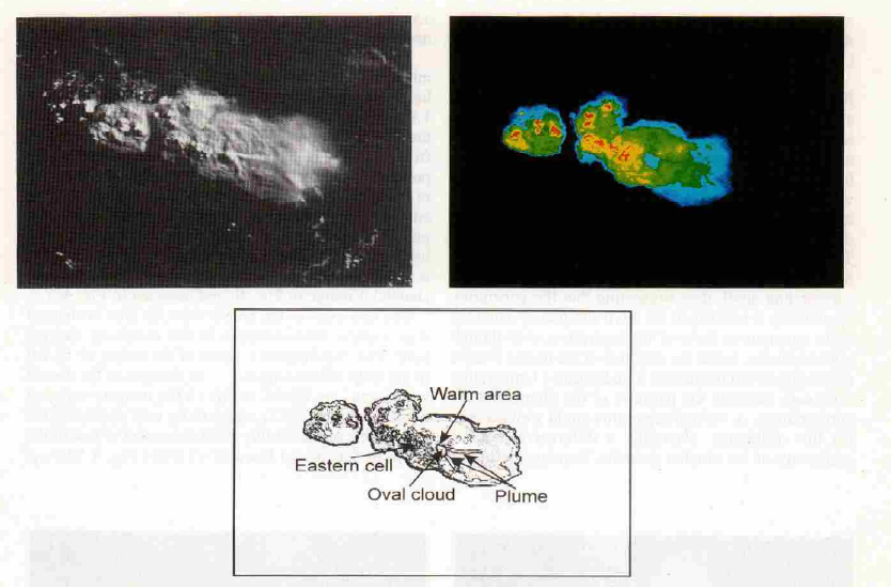

Figure 3.2: Images of a severe storm on 30 July 1994 over the English channel. The upper two images show AVHRR satellite images in the 0.725-1.1 μm channel (left) and 10.3-11.3 μm channel (right). The lower image presents a diagram of cloud top structure (Levizzani and Setvák, 1996).

sifiers whereby cloud pixels with similar spectral and textural properties are clustered. Methods such as neural networks and k-nearest neighbour can be used to compare pixel properties to a database selected by human experts (Tag *et al.*, 2000; Pankiewicz *et al.*, 2001). For supervised classification techniques, large amounts of training samples are selected from satellite imagery and labeled by experts to create a large database. One of the main limitations is that the method is trained for specific environments. Unsupervised classification techniques group statistically similar pixels. The obtained clusters are then labelled by experts. Berendes *et al.* (2008) use an unsupervised clustering algorithm, Standard Deviation Limited Adaptive Clustering (SDLAC), for convective cloud identification and classification in daytime satellite imagery. The focus is on classifying cumulus clouds in different stages of the life cycle. Spectral channels in the VIS, IR, NIR and WV from GOES 12, MODIS and SEVIRI were used as well as an 11 x 11 pixel neighborhood Grey Level Difference Vector (GLDV) derived from the HRV channel for each pixel. The GLDVs are used to measure the 'contrast' and is useful for identifying cumulus and stratocumulus clouds (Welch *et al.*, 1988). Statistically similar clusters are grouped into logical classes and therefore the cumulus cloud class may consist of several clusters. Each cluster consists of a mean and standard deviation for each spectral channel and features such as channel difference and texture. This information is not interpreted physically, but used to find the best fit for each cluster. The SDLAC algorithm has already been used as a detection algorithm for overshooting convective cloud tops.

3.5 TEMPORAL CLOUD INFORMATION

By tracking clouds and monitoring trends in spectral channels, convective cloud development can be observed for individual cloud systems. Roberts and Rutledge (2003) relate IR (10.8 μm) cloud top brightness temperature trends with radar reflectivity for quasi-stationary convection in eastern Colorado using GOES-8 and the Weather Surveillance Radar-1988 Doppler (WSR-88D). The Rate Of Change (ROC) of the BT is used to find active (large negative rates) and suppressed (positive or low negative rates) cumulus cloud growth over boundary layer convergence features. Results show that monitoring both the cloud growth and the occurrence of subfreezing cloud-top temperatures, which indicates the initiation of the ice nucleation process, via satellite, can lead to up to 30 minutes advanced notice of convective storm initiation over radar use only. Convective storm initation is defined as the initiation of storms that will eventually show radar reflectivities of > 35 dBZ. Also the false alarm rate is reduced when monitoring the ROC. For the separation between convective and stratiform cloud areas on the Southern side of the Alps, Bolliger *et al.* (2003) use spatial and temporal pixel (count: 0-255) information from Meteosat-6 data. Their method is based on the assumptions that convective cloud areas exhibit strong textural pixel variability in terms of count values and that they show a distinct temporal evolution due to strong up- and downdrafts within. The spatial variation is determined by calculating the variance of a 3 x 3 pixel array. A high variance indicates a strong textured cloud top associated possibly with convective activity. The temporal variation is calculated by determining the rate of change of individual pixel count values over a 10-minute period. Pixels showing strong cooling may indicate convective updrafts. The convective precipitation areas found by satellite are compared to radar results. Radar volumes containing convective precipitation are defined if the 90% quantile of the maximum reflectivity at a height interval 1.5 km above the $0\,^{\circ}\mathrm{C}$ reference height, i.e. 4.5-5.5 km, exceeds 30 dBZ. Fig. 3.3 shows a satellite and radar image of a deep convective cloud. The satellite image shows areas of cooling and warming, while the radar image shows areas of convective and stratiform precipitation. The localization of convection in the satellite image is only possible during the growing phase of the deep convection system, before the area is shielded by an anvil. Embedded convection is too weak to produce distinct signals. Data from the visible channel did not seem to improve the identification of convective areas.

Zinner *et al.* (2008) track and monitor severe convection from its initiation to the mature stage using Meteosat-8 SEVIRI channels IR 10.7 μm, WV 6.2 μm and VIS. Their method is called the Cumulonimbus Tracking And Monitoring (Cb-TRAM) algorithm. Before cell patterns are being detected and tracked, a motion field is extracted from two consecutive images using a so called pyramidal scheme. A disparity vector field is generated to interpolate images at time steps between two satellite images and to extrapolate images into the short-range future. An overlapping technique is used to track clouds. Detection of convective clouds is done in 3 stages. Stage 1 is the convective initiation and is detected by looking at rapid development of cloud areas in the HRV channel. Furthermore only HRV developments that are accompanied with cooling in the IR and HRV reflectivities of more than 0.5 are taken into account. From

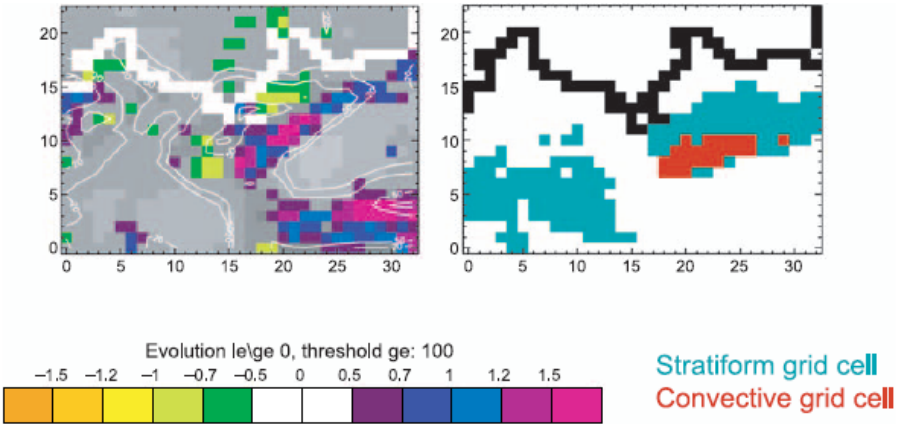

Figure 3.3: Satellite image (left) and radar image (right) of a deep convective cloud occuring on 4 October 1999 at 21:45 UTC in Switzerland (the thick white and black line in the images represent the country boarder). The coloured pixels in the satellite image indicate the intensity of the cooling (positive values) or warming (negative values). The blue colours in the radar image represent stratiform precipitation, while the red colours represent convective precipitation (Bolliger *et al.*, 2003).

the HRV t-1 image a first guess cloud structure without any additional cloud area development is made using the disparity vector field at t-1 for the current time step t HRV image. This first guess image is substracted from the current image. Positive areas represent gains in cloud area. The motion field, without changes in cloud amount, is approximated by using smoothed IR images of the previous two time steps. The same is done for the IR using the previous two WV images. A product field of the normalized ΔHRV and ΔIR is made and areas with values above a threshold are stored in the cloud mask and assigned development stage 1. Stage 2 is detected by looking at rapid cooling. The WV channel is used to detect rapid vertical development, due to growth of convective cells, by looking at the cooling of cloud tops in the upper troposphere. As in stage 1, ΔWV is obtained by subtracting the extrapolated image from time step t-1 to time step t from the current WV image whereby the disparity field is extracted from time steps t-1 and t-2. Again a threshold is used, but now to find areas of intense developments which are already likely to have hazardous intensities. Stage 3 represents mature thunderstorm cells. They are detected by looking at areas that exhibit WV temperatures close to the current temperature of the tropopause, obtained from the ECMWF model analyses, and large local gradients in reflectivities in the HRV channel. Marked are mature convective cells possible with cirrus anvil. For the measure of variability (regions of strongest updrafts generally exhibit strong cloud top height variability) a two dimensional gradient value from the surroundings of each pixel in the HRV channel is used. As in stage 1 the two thresholds are multiplied. The three development stages are combined into one mask showing all detected cell patterns and their stages. During night the marking of stage 1 cumulus clouds is de-actived and the marking of stage 3 cumulus clouds only uses the WV threshold. Thresholds where obtained from fuzzy logic using a data set containing convective events in Europe. Fig. 3.4 presents satellites images in the HRV, WV

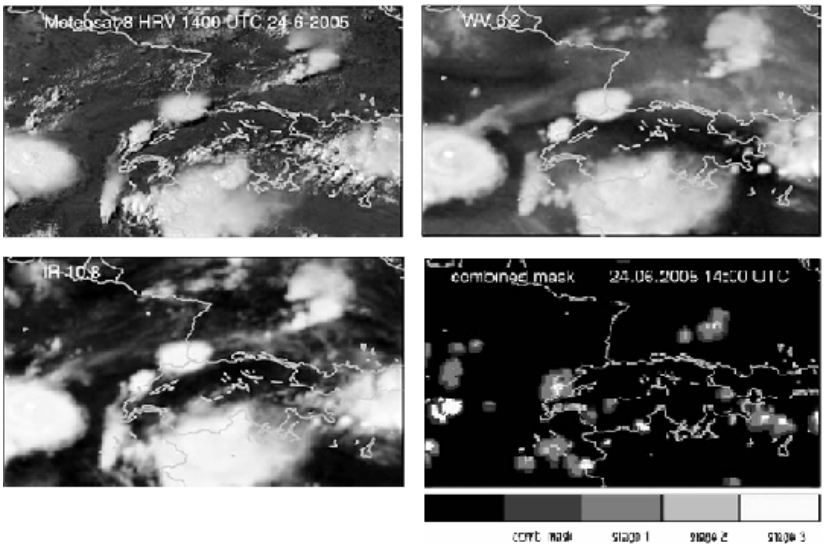

Figure 3.4: Satellite images from 24 June 2005 at 14 UTC over Central Europe in the HRV channel (upper left), WV channel (upper right) and in the IR channl (lower left). From these channels a combined mask of all three development stages (lower right) is created (Zinner *et al.*, 2008).

and IR channel and the mask that combines all three development stages. To validate the Cb-TRAM algorithm, German weather radar and lightning data are used. Radar reflectivities and the occurrence of lightning can be used to distinguish between smaller convective cells and large thunderstorms. The overall conclusion is that the algorithm is not only capable of correctly identifying thunderstorms and the cloud stages, but can also detect cell patterns which evolve into thunderstorms at a time when radar and lightning signals are not yet visible.

3.6 CONVECTIVE CLOUD MASKING

Next to Zinner *et al.* (2008) also Mecikalski and Bedka (2006) use cloud masking to define areas of (potential) convective clouds. They use near-real time geostationary satellite VIS and IR imagery to develop a nowcasting (0-1 h) Convective Initiation (CI) algorithm. GOES VIS (1 km resolution) and IR (4-8 km resolution) is used to identify cumulus clouds in the satellite imagery for which CI is likely to occur in the near future. Training data is used to evaluate satellite images prior to the occurrence of CI and to identify predictors of CI. Before IR-based 'interest fields' are developed a convective cloud mask is used to identify convective cloud pixels. The convective cloud mask includes a horizontal brightness gradient threshold in the VIS imagery to locate cumulus cloud edges and a dynamic (time-of-day, time-of-year) brightness threshold in the VIS imagery. The $-20\,^{\circ}\mathrm{C}$ 10.7 μm BT threshold is used to separate immature from mature cumulus clouds and cirrus. Above $-20\,^{\circ}\mathrm{C}$ it is assumed that the clouds are still immature and did not start to precipitate yet. Furthermore,

Table 3.1: The per-pixel interest fields and critical (threshold) values used in the CI-algorithm (Mecikalski and Bedka, 2006).

CI interest field	**Critical value**
10.7 μm T_b (1 score)	$< 0\,^{\circ}\mathrm{C}$
10.7 μm T_b time trend (2 scores)	$< -4\,^{\circ}\mathrm{C}$/15min ΔT_B/30 min$<\Delta T_B$/15 min
Timing of 10.7 μm T_b drop below $< 0\,^{\circ}\mathrm{C}$ (1 score)	Within prior 30 min
6.5 - 10.7 μm difference (1 score)	$-35\,^{\circ}\mathrm{C}$ to $-10\,^{\circ}\mathrm{C}$
13.3 - 10.7 μm difference (1 score)	$-25\,^{\circ}\mathrm{C}$ to $-5\,^{\circ}\mathrm{C}$
6.5 - 10.7 μm Time Trend (1 score)	$> -3\,^{\circ}\mathrm{C}$/15 min
13.3 - 10.7 μm Time Trend (1 score)	$> -3\,^{\circ}\mathrm{C}$/15 min

the standard deviation in the VIS imagery over a 5x5 pixel box is calculated and a threshold is set to assure enough spatial variation in the image. Only pixels identified as immature cumulus clouds are retained in the mask. Thick cirrus clouds(cold, little texture), mature cumulus clouds (cold, high texture) and stratus/thin cirrus clouds (warm, little texture) are removed. In total eight interest fields are chosen (see Table 3.1) and each pixel from the convective cloud mask is assigned one score if it satisfies the interest field. A pixel with at least a score of seven represents a cumulus cloud in a pre-CI state. To be able to use time trends, cloud motion has to be taken into account. From atmospheric motion vectors (AMVs) (identification algorithm of Velden *et al.* (1997)) Satellite derived Offset Vectors (SOVs) are formed. A SOV is defined as the number of pixels in the latitudinal and longitudinal direction that a given cumulus cloud pixel has moved in between two satellite images. The SOVs are calculated by decomposing the speed and direction of the velocity using the AMV algorithm, then multiplying the velocity components by the time interval (5-15 min) and divide the result by the pixel resolution. The results of CI cases are compared to the WSR-88D Doppler radar data for several cases (comprising of 3 different types of convective events) in the USA. Accuracies of 60/70% are obtained when comparing the CI nowcast pixels to radar reflectivities of > 35 dBZ. False alarms occurred due to small errors in the SOVs. Results show that moving convective storms can be predicted to 30/45 min in advance. The algorithm is designed to isolate larger cumulus clouds and will behave differently in different kind of environments. Ongoing work suggests that the trend in the 10.7 μm BT, the 10.7 μm BT itself and the trend in BTD for 13.3-10.7 μm are the most important interest fields. The CI nowcast algorithm can be improved by improving the cloud tracking algorithm, defining the correct interest fields and thresholds and their relative importance and better collocation of satellite and radar images. The CI algorithm could also be coupled to information about the lower tropospheric motion and atmospheric instability. For nighttime, a different algorithm has to be developed since VIS data is not available.

4th Chapter

DATA AND METHOD

This chapter describes the MSG-SEVIRI dataset, which includes cloud physical properties and HRV reflectances, and the METAR dataset which includes Cb/TCu reports. Both datasets are split into a training and validation dataset. Two steps in the Cb/TCu cloud detection method are presented. First, a convective cloud mask is used to construct a hazard map, which includes potential convective cloud pixels. Second, a logistic regression model is used to determine the risk, in terms of probability, that hazardous cloud areas consist of Cb/TCu clouds.

4.1 DATA

4.1.1 MSG-SEVIRI

From a number of studies presented in the previous Chapter, it has become clear that satellite data can be used to detect the presence of clouds as well as to distinguish between different types of clouds and precipitation. Most studies focus on the use of (multi-spectral) IR and WV thresholds. A few studies use satellite derived cloud physical properties to investigate precipitation processes within convective clouds and to estimate convective rainfalls. However, little effort has been done to directly relate satellite derived cloud physical properties to the presence of convective clouds, whether precipitating or not, within satellite images.

This research is focused on using MSG-SEVIRI derived cloud physical properties to detect convective clouds (Cb/TCu) within a defined area. The available satellite derived cloud physical properties are the cloud top temperature, the cloud optical thickness, the effective radius, the liquid water path and the Cloud thermodynamic PHase (CPH). They are derived using the DAK radiative transfer model and CPP algorithm as described in subsection 2.2.3. Furthermore, the reflectances in the visible wavelengths are used (HRV). Combined, they present a relevant set of cloud physical properties that can be used to distinguish between different types of clouds. Table 4.1 shows an (approximate) range of values of each cloud physical property. As mentioned in sub-

Table 4.1: MSG derived cloud physical properties and HRV reflectance: minimum and maximum values.

	Minimum	Maximum
CTT	200 K	300 K
COT	0	256
REFF water	1 μm	24 μm
REFF ice	6 μm	51 μm
LWP	0 g/m^2	8700 g/m^2
HRV	0	1

section 2.2.3, the effective radius depends on the thermodynamic phase of the cloud particles.

The MSG data are available for a box area of about 60 x 100 km centered around Schiphol, the main airport of the Netherlands. At the low spatial resolution, the MSG box area consists of 15 by 15 pixels. For the high resolution it is 45 by 45 pixels. Schiphol is located near the coast in the western part of the Netherlands at a latitude of $52.3\,^\circ$ and a longitude of $4.7\,^\circ$. The satellite viewing angle of MSG over the Netherlands is about $60\,^\circ$. The MSG box area is shown in Fig. 4.1. A large part of the MSG box area shows mainland. In this part of the country mainly cities and grass-lands are found and a neglegible orography (most part lies beneath the sea level). The north-west corner of the MSG box area shows a section of the North Sea. All MSG data are available at a time resolution of 15 minutes. The available data covers a period from the years 2004 to 2007 for the summer months May to September. Due to the preferred use of the HRV channel next to the derived cloud physical properties, only day-time data is considered. During the night no data from visible wavelength channels is available. In the CPP algorithm, retrievals are only made at solar zenith angles below $72\,^\circ$. Therefore, the length of the day-time period changes slightly from day to day through the year, but will be approximately between 6 a.m. and 6 p.m. This means that within this research the development of a Cb/TCu cloud detection method is focused on day-time summer period cases in the coastal area of the Netherlands. The cloud physical properties data are interpolated to the high resolution of the HRV data. By doing so, the cloud physical properties can be combined with the high detail of the visible channel. The HRV data is especially important for describing the textural characteristics (or spatial variability) within the MSG box area.

A few considerations should be made when using the MSG data. When observing high clouds at higher latitudes from a geo-stationary satellite, the parallax effect plays a role Due to the viewing condition (large angle between the satellite located above the equator and objects located at higher latitudes) there is a shift between the position of objects, such as clouds in the satellite image, and their real position. The maximum parallax for the highest clouds (>10 km) seen on a MSG satellite image, will be about 17 km to the north. This parallax effect will not be corrected for as explained in the next section. Furthermore, there

Figure 4.1: The MSG box area (red lines) with Schiphol Airport as the center pixel (red dot). The image has been taken from the Aqua satellite on 31 March 2003 (NASA/GSFC MODIS Land Rapid Response Team).

exists a shift between the HRV image and the images at other wavelengths due to the scanning mechanims of SEVIRI. The shift in the HRV image is corrected for using the 0.6 μm channel, which lies within the spectral broadband HRV channel. The HRV image is downscaled to the low resolution of the 0.6 μm channel by taking the average reflectance of a 3x3 pixel box. Next, the HRV image is shifted into all directions and compared to the 0.6 μm channel. The shift that results into the largest correlation between the two images is used. Almost all cases show the same shift and no more than one pixel to the west and two pixels to the north. This is consistent with the findings of Duerr *et al.* (2009) and Deneke and Roebeling (2009).

4.1.2 HRV-COT, RADAR AND LIGHTNING DATA

Next to the MSG-SEVIRI derived cloud optical thickness at low resolution, a high resolution cloud optical thickness (HRV-COT) has been derived, using observations from the high resolution visible channel. The CPP algorithm retrieves COT from the 0.6 μm channel, which observes radiances in a narrow band around 0.6 μm, see Table 2.3. The HRV channel observes radiances over a wider range around 0.6 μm, between 0.3 and 0.8 μm, but can be used to approximate COT at a higher spatial resolution. In this research, a simple procedure is adopted to estimate the COT of HRV pixels in three steps. First, a simple parameterization is defined to relate LUTs of 0.6 μm radiances to COT. Second, the radiances of nine HRV pixels are re-calibrated to radiances of the low reso-

lution 0.6 μm channel, using the ratio between HRV and 0.6 μm radiances as a correction factor. Third, HRV-COT is retrieved from the re-calibrated HRV radiances, using the simple parameterization defined at step one. The parameterization is constructed in such a way that the problem of the fast saturation of the HRV (reaching maximum reflectance values) with respect to the COT is minimized, see Fig. 2.12. Similar to the 0.6 μm low resolution COT values, the HRV-COT values range from 0 to 256. Note that the construction of the HRV-COT is a rough approximation and should be refined in future research, but suffice for the purpose of investigating usefulness of cloud physical properties on high resolution.

To investigate the combined performace of MSG satellite data and radar and lightning data, radar reflectivities from the KNMI weather radar have been used to calculate the mean, minimum and maximum dBZ values within the MSG box area. Also the number of pixels with values above 30 dBZ, which is similar to the 29 dBZ threshold value used in the present KNMI radar-based Cb/TCu detection method (Wauben *et al.*, 2006), and above 40 dBZ are combined with MSG satellite data. From the lightning detection network (SAFIR: Surveillance et Alerte Foudre par Interférométric Radioélectrique), the number of detected flashes, with a minimum of two, over the past ten minutes within the MSG box area is used.

4.1.3 METAR

METAR is a format of a weather report about the current state of the weather at and in the vicinity of an airport and is released on a routine bases. It is intended for external use and is predominantly used by pilots as part of the pre-flight preparations at other national and international airports. At Schiphol most meteorological information, such as wind speed and direction, has been automated. This means that meteorological quantities are measured by instruments located at the airport. However, at all times a human observer is present to monitor the current state of the weather and to report subjective information based on visual inspection. The METAR reports are generated twice an hour, namely at 25 and 55 minutes past the hour. The reports include information about the weather over the last 10 minutes.

A maximum of five cloud layers can be reported, whereby cloud cover and cloud base height are reported for each cloud layer. The degree of cloud cover increases with increasing cloud base height when several cloud layers are being reported. Cloud type is not reported. Exceptions are made for well-developed cumulus clouds, which are the cumulonimbus and towering cumulus clouds, because these clouds may pose a threat to flight safety. One layer consisting of both cumulonimbus and Towering cumulus cloud is reported as Cumulonimbus cloud. The METAR reports do not include information on the exact location of the reported Cb/TCu clouds.

Well developed cumulus clouds with greater vertical extents than horizontal extents are considered TCu clouds. The transition of a TCu cloud into a Cb cloud can be seen by observing the cloud top. For a TCu cloud this cloud top will show sharp edges. When enough vertical growth occurs, the cloud top will reach heights cold enough to form ice crystals. The presence of ice crystals

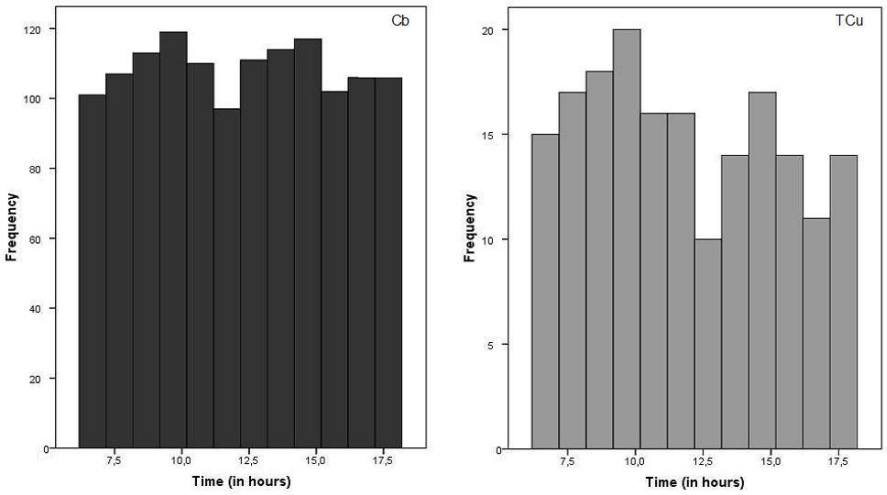

Figure 4.2: Daily spread of occurence of Cb (left) and TCu clouds (right) as observed at Schiphol airport for the day-time summer of the years 2004-2007.

in the cloud top changes the sharp edges into vague, fibre edges.

Besides weather at the airport, also weather phenomena within a radius of 8 km outside the airport area are reported (Postma, 2008). Cb/TCu cloud reports in METAR are likely not to be completely restricted by this radius. According to one of the meteorologists at the Schiphol weather station, an important criterion is the cloud base height. If the cloud base is still distinguishable at the horizon, the cloud is likely to be reported. Furthermore, convective clouds located outside the radius may be reported if it is believed that they may pose serious threat to flight safety in the near future. E.g., this might be the case for a clearly visible mature cumulonimbus cloud located at a large distance, but heading into the direction of the airport. The question whether or not a Cb/TCu cloud is reported remains subject to the professional judgement of the present meteorologist.

Fig. 4.2 shows the daily spread of Cb and TCu cloud reports from 6 a.m. to 6 p.m. (with a maximum of two reports per hour) for the entire period May 2004 to September 2007 at and in the vicinity of Schiphol airport. A dip can be seen around noon for both Cb and TCu clouds. Solar surface heating is considered to be one of the main formation processes of strong convective clouds over land during the summer. However, the expected increase of Cb reports during the day with a maximum in the late afternoon is not visible. Yet, there is an increase of both Cb and TCu cloud reports in the morning, followed by the dip at around 10 a.m.. At KNMI one explaination has been suggested: the increase of the reports in the morning followed by the dip in the noon might be explained by the formation of Cb/TCu clouds over the sea during the night due to relatively cold air above a warm sea surface. Due to the prevailing south-west wind direction at the Dutch coastline, these clouds are advected into the land and therefore might enter the MSG box area during the morning. Eventually they will die out due to the absence of the warm sea surface. After midday, the number of Cb/TCu reports may now increase again due to solar

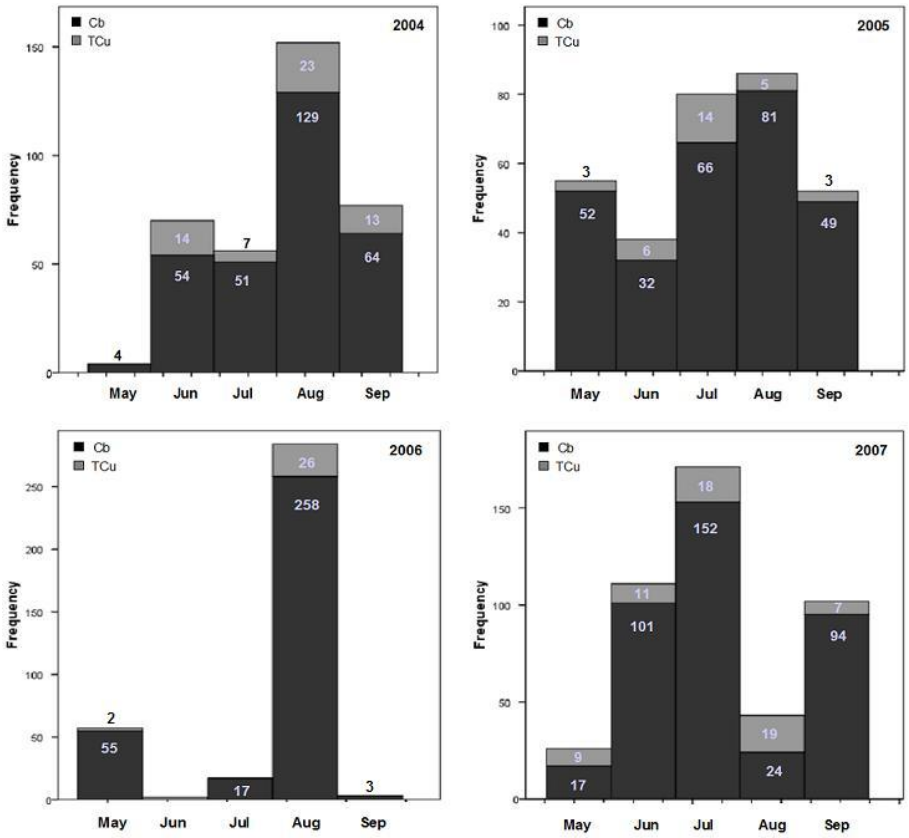

Figure 4.3: METAR Cb and TCu cloud reports observed at Schiphol airport for the daytime summer period of the years 2004-2007.

surface heating. In the late afternoon, the clouds may then again be advected into the land, therefore leaving the MSG box area. The formation of convective clouds above the sea occurs most often at the end of the summer and autumn. However, no clear evidence has been seen from the METAR data that most Cb/TCu clouds reported in the morning occur in late August or September.

Fig. 4.3 shows the monthly Cb/TCu reports for the years 2004-2007. The interannual variability is clearly visible, still for 3 out of 4 years most Cb reports occur in August. The year 2006 was a very warm year. However, August was very wet and relatively cold. In that month, convective clouds were produced almost on a daily basis in the Netherlands. Outside this month, almost no TCu reports were made in 2006. In contrast to August 2006, August 2007, which was a relatively dry month, only shows a few Cb reports. In this year, July was a very wet month with several big storms and the most Cb reports. For the entire period 2004-2007, least Cb/TCu reports were made in the month May, followed by June and September. Together, the reports represent 171 convective days (at least one Cb or TCu METAR report per day) out of 612 days over the entire period May 2004-Sept 2007, as observed at and in the vicinity of Schiphol airport.

Both figures show that much more Cb cloud reports than TCu cloud reports (about 14%) have been made. This can be explained by the longer lifetime of Cb clouds and their greater horizontal and vertical dimensions which makes it easier to observe them and more likely to report a Cb cloud than a TCu cloud. Since the number of TCu cloud reports is small compared to the Cb cloud reports and the transition from a TCu cloud to a Cb cloud may not always be obvious, it has been decided to group the two convective cloud types into one class. This means that the METAR dataset has been reduced to a dichotomous dataset. The two groups are: Cb/TCu present and no Cb/TCu present. Cases with presence of Cb/TCu clouds within the MSG box area at a time step are called the yes-events (1), while cases with no Cb/TCu presence are called the non-events (0). This dichotomous dataset now has to be matched to the MSG-SEVIRI dataset. The dimensions of the MSG box area exceed the formal maximum observing range of the 8 km radius around Schiphol airport. In the west-east direction the distance from the center pixel (Schiphol weather tower) to the MSG box area boarder is about 30 km. For the south-north direction it is 50 km. However as mentioned before, large convective clouds having a relatively high cloud base (which occurs especially during the summer due to boundary layer mixing) are likely to be reported as well when they are located at distances far beyond the formal maximum observing range. The parallax effect in the MSG data may shift the actual position of convective clouds up to 17 km to the north in the satellite images. Due to the relatively large distance of 50 km in the north-south direction from the center pixel in the MSG satellite images, it is assumed that reported Cb/TCu clouds that were located in the northern part of the MSG box area will still show up in the MSG satellite images. On the other hand, Cb/TCu clouds that were located south from the MSG box area and therefore too far to be reported at Schiphol, might show up in the MSG satellite images. At airports only having AUTO METAR, meaning no human observer is present, Cb and TCu clouds are detected using radar reflectivity data within a radius of 30 km around the weather station and lightning discharges data within a radius of 20 km around the weather station (Wauben *et al.*, 2006). The somewhat greater dimensions of the MSG box area compared to the formal viewing range of the observer may weaken the statistical relationship (treated in section 4.3) between the METAR reports and the cloud physical properties and HRV reflectance. It is assumed that almost all reported Cb/TCu clouds are located (at least partly) within the MSG box area.

The two hourly METAR time steps are matched to the four hourly MSG time steps by relating one METAR time step (25 or 55) to two MSG time steps (11 and 26 or 41 and 56), see Fig. 4.4. The four MSG time steps do not fall within the 10 minutes reporting time of the two METAR time steps. However, the difference between the METAR time period and the two corresponding MSG time steps only differ by one and four minutes, respectively. It is assumed that within those one minute and four minute periods the cloud fields within the MSG satellite image will change very little. Therefore, it will not have significant effect on the outcome of presence or no presence of Cb/TCu clouds within the MSG box area at that METAR time step.

Both the METAR and MSG-SEVIRI datasets are divided into a training (dependent) dataset and a validation (independent) dataset. This is done by randomly selecting about 70% of all days using a Bernoulli distributed random

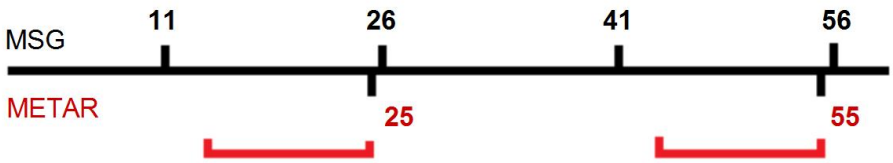

Figure 4.4: The four time steps of MSG (black) and the two 10 minute periods of METAR (red) for a one hour timeline. The numbers indicate the minute past the hour.

variate with a 0.7 probability parameter. Doing the random selection on days and assuming that cases on different days do not represent the same event (Cb/TCu cloud) provides for an independent validation dataset. The cases included in the 70 % selected days will be used to train the Cb/TCu cloud detection method. The cases from the remaining days will be used to validate the Cb/TCu cloud detection method. Part of the MSG-SEVIRI data are missing due to problems with the data reception system. The time steps for which the MSG data were missing have been removed from the MSG-SEVIRI and METAR dataset. This leads to a 18% reduction of Cb/TCu cases. A total of 1218 convective cases remain.

4.2 CONVECTIVE CLOUD MASK

The first step in the development of a convective cloud detection method is the Convective Cloud Mask (CCM). The cloud physical properties and HRV reflectance are used to construct a pixel-based mask for the entire MSG box area at each time step. Using a thresholding technique the CCM determines for each pixel whether or not it should pass the mask. The pixels that pass the CCM are considered to represent potential convective cloud pixels. Pixels that do not pass the CCM will not be considered in future calculations. The objective is to reduce as many of the non-convective cases (no Cb/TCu report) as possible, while at the same time retaining as many of the convective cases as possible. The cloudy pixels passing the CCM can be considered to form a hazard map, indicating which pixels might pose a risk to flight safety in the sense that they represent Cb/TCu clouds. The level of risk will be determined in the second step of the Cb/TCu cloud detection method.

The principle of the convective cloud mask is to use the cloud physical properties and HRV reflectance to characterize clouds and therefore also to discriminate between different cloud types in a satellite image. Cb and TCu clouds are dense clouds with great vertical extents. Therefore these clouds exhibit low cloud top temperatures and are optically thick. When enough vertical growth takes place ice crystals will be present in the cloud top. A glaciated cloud top with relatively small effective radius may indicate a mature Cb cloud (anvil). In satellite infrared imagery, Cb/TCu clouds will appear brighter compared to lower cumulus clouds. The effective radius of liquid water droplets increases until precipitation is initiated within the cloud. The presence of ice crystals in the cloud tops can also initiate precipitation, see subsection 2.1.1 The reflectance in the visible, also called cloud albedo, is closely related to the optical

thickness and is high for Cb/TCu clouds. Therefore, in visible satellite imagery Cb and TCu clouds will appear bright. Strong convective clouds often exhibit a lumpy texture, which is caused by shadow effects of the irregularly-shaped cloud tops. This results into a large spatial variability in satellite images. Mature Cb clouds often consist of an anvil. The anvil is relatively flat, but is usually interrupted by overshooting tops. This will again give a lumpy appearance in certain areas. A group of organized convective cells also shows a large spatial variablity in the visible satellite image. The spatial variability in the visible is included in the CCM by using a threshold for the HRV standard deviation (HRV std) within the MSG box area. The non-convective cirrus clouds are located at high altitudes and are mostly composed of ice crystals. Thin cirrus clouds are semi-transparent to sunlight and longwave radiation emitted at the surface. Therefore, they will have a small optical thickness and a low cloud top temperature, also due to contamination by the surface radiaton. Thick cirrus clouds might have a bright appearance in the visible and lower cloud top temperatures, but show little spatial variability. Stratus clouds can be optically thick and have a bright appearances in the visible, but have higher cloud top temperatures, are usually composed of liquid water droplets and show little spatial variability in the visible. Weak convective clouds such as stratocumulus clouds can be optically thick, highly reflective and have some vertical growth, but do not show the same distinct signals as Cb/TCu clouds do.

A combination of thresholds for the cloud physical properties and the HRV reflectance will be used to distinguish between well developed cumulus clouds and non-convective clouds. From the satellite derived cloud physical properties the cloud top temperature, optical thickness, effective radius and cloud phase are used. The 4-8 km cloud physical properties data are interpolated to the 1-2 km resolution of the visible channel; one pixel of CTT, COT and REFF is divided into 3x3 pixels, all having the same value. The optimal combination of thresholds for the cloud physical properties and the HRV reflectance will be determined using the training dataset. Criterium is that > 95 % of the convective cases pass the CCM. The combination that obeys this criterium and at the same time shows a maximum reduction of the non-convective cases will be used. Furthermore, a minimum number of 10 pixels (~ 0.005 %) that pass the CCM at each time step is required to assure statistic significance in future calculations. This means that the minimum detectable cloud size is about 20

Table 4.2: Values of the cloud physical properties and HRV reflectance that are used to investigate CCM thresholds.

	Range	Step
CTT	265 K - 285 K	5 K
COT	5 - 25	5
REFF	8 μm - 16 μm	2 μm
HRV	0.3 - 0.7	0.1
HRV std	0 - 0.1	0.025

km^2. This corresponds to a cloud with a horizontal radius of about 2.5 km, when assumed a circular shaped cloud. Table 4.2 shows the value ranges and steps of the cloud physical properties and the HRV reflectance that will be investigated, yielding 3125 different combinations. The effective radius is only considered for the liquid water phase. Pixels consisting of the ice phase do not need to pass the effective radius threshold.

4.3 LOGISTIC REGRESSION

Logistic regression is the second step in the convective cloud detection method. Logistic regression models are used in situations where one wants to predict the presence or absence of a characteristic or outcome based on values of a set of predictor variables. The variable of interest, or dependent variable, has to take on two values (dichotomous variable), while the predictor variables, or independent variables, can be of any type. For years, logistic regression has been used extensively in the medical and social sciences. In meteorological research, logistic regression has been applied to e.g. short-term forecasting of thunderstorms (Schmeits *et al.*, 2008), short-term forecasting of premonsoon convective developments (Dasgupta and De, 2007) and forecasting of large hail (Billet *et al.*, 1997). Furthermore, it has been used as a tool to investigate the difference between the present weather reported by a professional and present weather reports produced by automated weather stations (Merenti-Välimäki and Laininen, 2002).

In this research, the dependent variable, also called predictand, is the presence of Cb/TCu clouds at and in the vicinity of Schiphol airport. This is determined by the METAR reports. A set of predictors will be constructed from the MSG-SEVIRI derived cloud physical properties, HRV reflectances, HRV-COT and radar and lightning data. A physical relationship between these predictors and the presence of convective clouds is assumed. Logistic regression models return probabilities, which provide a measure of uncertainty. The logistic function is therefore bounded between 0 and 1 (or 0 and 100 %). This probability indicates the level of risk of Cb/TCu clouds being present in the MSG box area for the pixels within the hazard map.

4.3.1 LOGISTIC REGRESSION MODEL

Logistic regressions are fit to a dichotomous predictand using the nonlinear equation (Wilks, 2006)

$$P(y) = \frac{1}{1 + exp[-(a_0 + a_1x_1 + a_2x_2 + ... + a_nx_n)]} \tag{4.1}$$

in which $P(y)$ is the probability that an event y occurs, x_i (i=1, 2 , ..,n) is the set of predictors and a_i (i=0,1, 2, ..,n) are the regression coefficients. In contrast to linear regression, the dependent variable (y) does not need to be normally distributed and the residuals do not have to be Gaussian distributed with constant variance. In fact, in logistic regression models the residuals are Bernoulli variables. Furthermore, the independent variables (x_i) need not to be interval

variables and unbounded. The regression coefficients vary between plus and minus infinity. A zero regression coefficient indicates that the accompanying predictor does not contribute to the logistic regression function. The regression coefficient a_0 is the regression coefficient of the constant-only model (intercept), which is a logistic regression model without any independent variables. In the case of a model having only one predictor, Eq. (4.1) is an S-shaped curve that is a function of x_1. The fitting procedure of the regression coefficients is iterative and based on maximum likelihood method. The iterative maximum likelihood method determines the set of values for the regression coefficients which maximizes the product of all computed probabilities of the events (Wilks, 2006). Rearrangement of Eq. (4.1) into

$$ln\left[\frac{P(y)}{1-P(y)}\right] = a_0 + a_1x_1 + a_2x_2 + ... + a_nx_n \tag{4.2}$$

shows that the logistic regression coefficients can be viewed as linear with respect to the natural logarithm of the odds $\frac{P(y)}{1-P(y)}$. This rearrangement is called the logit transformation and the term on the L.H.S. is called the logit. The odds ratio is the ratio of the odds of an event y occurring in group 1, $\frac{P_1(y)}{1-P_1(y)}$, to the odds of the event occurring in group 2, $\frac{P_2(y)}{1-P_2(y)}$. An odds ratio of 1 indicates that the event is equally likely to occur in both groups. The impact of a predictor is often explained in terms of odds ratios. The exponent of a regression coefficient is the odds ratio for the accompanying predictor. For continuous variables, the odds ratio represents the factor by which the odds of an event change for a one-unit change in the variable. In general, this change is greater when the original probability is near 0.5, and smaller when the original probability is near 0 or 1 (also indicated by the shape of the S-curve).

The overall goodness-of-fit of a logistic regression model can be tested using the Hosmer-Lemeshow chi-square goodness-of fit test (Hosmer and Lemeshow, 2000). The fitted data is divided into deciles based on predicted probabilities. Using a chi-square distribution, the observed and expected frequencies are compared. The probability statistics (P-value) is computed from the chi-square distribution with 8 degrees of freedom. For adequately fitting models, the P-value should be greater than 0.05. This means that the null hypothesis, which says that the model predictions are not significantly different from the observed values, may not be rejected. It does not tell whether much of the variance is explained by the model, but what is explained is significant. For small sample sizes (small to moderate sample sizes: n $<$ 400), the Hosmer-Lemeshow test can be biased toward non-significance, which means that the model fit will be overestimated. On the other hand, for large sample sizes the Hosmer-Lemeshow test is likely to find significant P-values for smaller differences between observed and model predicted values, even though the model adequately fits the data. An alternative to the Hosmer-Lemeshow test is the likelihood ratio test. It is based on the -2 Log Likelihood (-2LL), also called deviance, which has an approximate chi-square distribution. The -2LL statistic is the likelihood ratio and is used to determine the significance of the unexplained variance in the dependent variable. The likelihood ratio test tests whether the model with a set of predictors is significantly different from the constant-only model. A finding of significance (P-value $<$ 0.05) indicates that the model

is significantly different from the constant-only model and leads to the rejection of the null-hypothesis that all of the regression coefficients are zero. The likelihood ratio test is not only used to test the overall model, but also to test nested models and therefore can be used to test individual independent variables. The difference in -2LL (the smaller, the better) between a model and its reduced model (dropping the independent variable of interest) should be significant in order to justify inclusion of that variable in the model. An alternative to the likelihood ratio test for testing significance of individual logistic regression coefficients for each independent variable is the Wald test. It is the squared ratio of the unstandardized logistic regression coefficient to its standard error. A non-significance of the Wald statistic suggests that the variable may be dropped from the model. The likelihood ratio test is generally preferred over the Wald test, which may lead easily to so called Type II errors (thinking there is no relationship when there is) due to inflated standard errors for large regression coefficients. The change in deviance can be used to identify cases that are poorly fitted by the model. Larger changes in deviance indicate poorer fit. The deviance statistics are based on the likelihood ratio.

The overall predictive strength, or effect size, of the predictors in a logistic regression model can be described using the odds ratio. The ratio of the odds ratios of the independent variables indicates the relative importance of the independent variables with respect to the odds of the dependent variable. Also, inspecting the 95% Confidence Interval (CI) of the odds ratios (exponent of the regression coefficient) can be useful. If this interval includes the value 1 (exp[0]) , the effect on the odds of the dependent variable is (near) zero for certain values of the independent variable. In that case, the independent variable is mostly not considered a useful predictor. Another way of measuring strength of association is the use of R^2-like measures. In linear regression models, the R^2 measures the percent of variance explained. However, for dichotomous dependent variables the variance depends on the frequency distribution of that variable and will be maximum for a 50-50 split. Several R^2-like measures for logistic regression have been proposed. The Nagelkerke's R^2 is a modified Cox and Snell coefficient and can vary between 0 and 1. The R^2-like measures usually take on relatively low values. There is no consensus on what a good R^2 value is and it is generally not used to asses goodness-of-fit but to compare several (nested) models fit to the same data. According to this measure the model with the largest value is the best model. The discriminative power of a logistic regression model can be measured by the area under the curve in a Receiver Operating Characteristic diagram (ROC). In a ROC diagram the 1-

Table 4.3: Values of the area under the ROC curve.

Area	**Discriminative power**
0.5	No discrimination
0.7-0.8	Acceptable discrimination
0.8-0.9	Excellent discrimination
> 0.9	Outstanding discrimination

FAR (probability that a "negative case" is correctly identified) is plotted against the POD (probability that a "positive case" is correctly identified), producing a curve. The area under this curve varies between 0 and 1.0. The predicted probabilities for correct cases are always higher than the predicted probabilities for incorrect cases. An area of 0.5 indicates that the predicted probabilities are not better than chance. It is the percent of all possible pairs of the dependent variable (0 and 1) where the correct cases have higher predicted probabilities than the incorrect cases. Table 4.3 shows general rules suggested by Hosmer and Lemeshow (2000). It should be noted that the area under the ROC curve does not provide information about goodness-of-fit. A poor-fitted model may still have good discriminative power. Furthermore, a frequency histogram of predicted probabilities, an Attributes diagram and a contingency table can be used to verify predictions. The contingency table shows the practical results of using the logistic regression model and will be discussed in the following section.

4.3.2 PREDICTOR SELECTION

The available MSG-SEVIRI derived cloud physical properties (CTT, COT, REFF and LWP), as well as the HRV reflectance, are considered potential predictors as well as the HRV-COT and radar and lightning data. To create a number of potential predictors several statistics have been calculated, see Table 4.4. The statistics of the potential predictors have been calculated only for pixels flagged as convective clouds in the first step of the detection method (CCM). A minimum of 10 cloudy pixels is required for proper statistical calculations. The standard deviation is calculated for the entire MSG box area and gives an indication of spatial variation within the box The median and percentiles are a measure of proportions of the data that fall below and above certain values and may be indicative to whether or not (and in what sense) a group of cloudy pixels posses (relatively) strong signals. The minimum and maximum present the extreme values present in the MSG box area and the range is the difference between those values. The use of trends in time of cloud physical properties as predictors has been investigated. An attempt has been made to create a cloud tracking algorithm within the MSG box area. However, the spatial resolution and the MSG box area size were too small for proper cloud tracking and trends in time for the entire MSG box area showed too much fluctuations to be of any use.

To get an indication of which set of the derived predictors might result into a well-performing model, a forward stepwise selection method is used. The method starts with the constant-only model. At each step the predictor with the largest score statistics (here: likelihood ratio) and a significance value less then 0.05 is added to the model. This will continue stepwise until non of the variables left have a significance value less then 0.05. Predictors that were included, but at some step show a significance value above 0.1, are excluded again. The forward stepwise selection method will be performed on randomly selected parts (25%) of the training dataset as well as on parts of the dataset representing different time-of-year and time-of-day periods. The method is performed over 100 times and selected predictors will be counted. It should be

Table 4.4: Statistics derived from the MSG-SEVIRI cloud physical properties, HRV reflectance, HRV-COT and radar and lightning data for the collection of pixels in the CCM to create potential predictors.

Cloud Physical Properties	**Radar**	**Lightning**
Mean	Mean	# flashes (10 min)
Median	Minimum	
Standard deviation	Maximum	
Minimum	Range	
Maximum	$>$ 30 dBZ	
Range	$>$ 40 dBZ	
percentiles: 2.5, 17, 25, 75, 83, 97.5		

stressed that the forward stepwise selection method is solely based on statistical criteria and is only used as an indicative method for finding a useful set of predictors. No perfect model exists and different sets of predictors may result into (near) equally well-performing models. Furthermore, individual predictors that have weak explanatory power may have large explanatory power as a group.

Nested models will be compared using the likelihood ratio test, the Nagelkerke's R^2 value, the Hosmer-Lemeshow test and the value of the area under the ROC curve. The number of predictors in the model needs to be limited in order to prevent over-fitting. Once a useful set of predictors with enough explanatory power has been identified, the independent variables have to be examined more closely. For continuous variables the assumption of linearity in the logit has to be checked. This is done by splitting the continuous variables into quartiles. The lowest quartile serves as a reference state (assuming a regression coefficient of zero) while for the other three quartiles a dummy variable is created. The dummy variables will take on a value of 1, if the value of the independent variable lies within the quartile of the associated dummy variable, and will be zero otherwise. The regression coefficients of the three dummy variables will be determined by newly performing the logistic regression and plotted against the mid-points of the quartiles. For linearity, the increase or decrease in the regression coefficients should be linear with respect to the quartiles. When the relation is not linear, a correct parametric relationship has to be found. Incorrect parametric relationships may reduce the statistical relationship between the predictors and the predictand. Interaction between two independent variables can be tested in the same manner as nested models. An interaction term can be created by multiplying the two independent variables. The model chi-square, which is -2LL for the model including the interaction term minus -2LL for the reduced model, should have a significant reduction in order to include a interaction term in the model.

4.4 VALIDATION

The validation of the Cb/TCu cloud detection method will be performed on the validation dataset using predicted probabilities and predicted group membership.

4.4.1 PREDICTED PROBABILITIES

Once the logistic regression function has been determined from the training dataset, it will be used to calculate predicted probabilities for the cases in the validation dataset. A common scalar accuracy measure for verification of probabilistic forecasts of dichotomous events, which here will be used to verify detection, is the Brier Score (BS) and it is given by (Wilks, 2006)

$$BS = \frac{1}{n}\sum_{k=1}^{n}(y_k - \sigma_k)^2 \tag{4.3}$$

in which y_k and σ_k are the predicted probability and observation respectively of n detection-event pairs. The observation is $\sigma = 1$ if the event occurs and $\sigma = 0$ if the event does not occur. The Brier score is the mean squared error of the detection probabilities. Since the probabilities and observations are both bounded by zero and one, so is the BS. It is negatively orientated which means that for a perfect forecast BS=0. The BS can be algebraically decomposed (Murphy, 1973) into three terms:

$$BS = I + II + III \tag{4.4}$$

in which

$$I = \frac{1}{n}\sum_{i=1}^{I} N_i(y_i - \bar{\sigma}_i)^2 \tag{4.5}$$

$$II = -\frac{1}{n}\sum_{i=1}^{I} N_i(\bar{\sigma}_i - \bar{\sigma})^2 \tag{4.6}$$

$$III = \bar{\sigma}(1 - \bar{\sigma}) \tag{4.7}$$

with

$$n = \sum_{i=1}^{I} N_i \tag{4.8}$$

Here y_i is the predicted probability, N_i is the number of event-pairs and $\bar{\sigma}_i$ is the subsample relative frequency of one of the I subsamples. Furthermore, $\bar{\sigma}$

is the sample climatology of the observations. Usually the predicted probabilities and observed relative frequencies are compared by dividing the data into deciles, which leads to 10 subsamples. The first term I, is called the Reliability and should be as small as possible. It is the weighted average of the squared difference between the predicted probability y_i and the observed relative frequency of the event in each subsample. The relative frequency of the event should be small for low values of the predicted probability y_i (near 0) and should be large for high values (near 1). For perfect reliable detections the subsample relative frequency should be equal to the predicted probability in each subsample. The second term II, is called the Resolution and should be as large as possible. It is the weighted average of the squared difference between the subsample relative frequencies and the overall sample climatological relative frequency and measures the ability of the predicted probabilities to discern subsample predicted probability with different relative frequencies of the event. For large values of the Resolution, the predicted probabilities resolve the event well. The third term III, is called the Uncertainty and only depends on the sample climatological relative frequency, meaning the variability of the observations. It will be small when the event almost never happens or almost always happens. For a climatological probability only, the Reliability will be zero as well as the Resolution term. Then, the BS equals the Uncertainty term.

From the Brier score the Brier Skill Score (BSS), a relative accuracy measure, can be computed using a BS score of a reference probability (Wilks, 2006).

$$BSS = 1 - \frac{BS}{BS_{ref}} \tag{4.9}$$

Climatological relative frequencies are often used as reference probabilities. If the reference probability is defined by the sample climatology, the BSS can be rewritten into

$$BSS = \frac{Resolution - Reliability}{Uncertainty} \tag{4.10}$$

Since the Uncertainty is always positive, the predicted probabilites will exhibit positive skill when the Resolution term is larger than the Reliability term. In this research the sample climatology of the available cases in the METAR dataset are used as the reference probability.

4.4.2 CLASSIFICATION

To analyse and validate the results of this study for parctical applications, the probabilities from the logistic regression model have been converted into a dichotomous dataset describing cases of presence or absence of Cb/TCu clouds within the MSG box area at a given time step. These cases can be classified by converting the predicted probabilities into predicted group memberships using probability threshold. A probability threshold of 0.5 says that cases with a predicted probability of less then 0.5 will be assigned a value of 0, while predicted probabilites of 0.5 and above will be assigned a value of 1. What is considered a useful probability threshold may differ for different application areas and objectives. Once the predicted probabilites are converted into group

Table 4.5: The contingency table for a dichotomous predictand.

	Observed 1	Observed 0
Detected 1	*Hits*	*False Alarms*
Detected 0	*Misses*	*Correct negatives*

membership, a contingency table can be used to determine verification scores, see Table 4.5.

The data in the contingency table can be displayed in counts or relative frequencies, which is counts divided by the number of predictions n. The hits are the yes-events that are predicted correctly, while the false alarms are the non-events that were predicted as yes-events. Misses are the yes-events that were predicted as non-events and the non-events that were predicted correctly are the correct negatives. From the contingency table several scalar attributes can be calculated: ACCuracy (ACC), Probability Of Detection (POD), False Alarm Rate (FAR), Critical Succes Index (CSI) and the Bias (Wilks, 2006).

$$ACC = \frac{Hits + Correct\ negatives}{n} \tag{4.11}$$

$$POD = \frac{Hits}{Hits + Misses} \tag{4.12}$$

$$FAR = \frac{False\ alarms}{Hits + False\ alarms} \tag{4.13}$$

$$CSI = \frac{Hits}{Hits + Misses + False\ alarms} \tag{4.14}$$

$$BIAS = \frac{Hits + False\ alarms}{Hits + Misses} \tag{4.15}$$

All scalar attributes, except the Bias, have values between 0 and 1. The ACC, POD and the CSI are positively oriented, which means that 1 is the best score, while the FAR is negatively oriented, which means that 0 is the best score. The accuracy is just the proportion correctly predicted cases. Correctly predicted yes-events and non-events are equally credited and false alarms and misses are equally penalized. The conditional probabilities POD and FAR are used to asses discrimination. The POD is the fraction of the cases were a yes-event was predicted and also observed. The FAR is the fraction of the cases were a yes-event was predicted but not observed. When the yes-events are rare compared to the non-events the dataset is unbalanced and correct predictions of the non-events can be made easily, which results into a large number of correct negatives. Including the correct negatives may lead to overoptimistic result,

therefore the ACC may not be the most desirable scalar attribute to asses performance of the detection method. The CSI does not include the correct negatives and therefore is a more useful scalar attribute when yes-events are rare. It is the proportion correctly predicted cases after the removal of the correct negatives. The Bias is the ratio of the number of predicted yes-events to the number of observed yes-events and compares the average prediction with the average observation. An unBiased detection method has Bias=1, while a Bias $>$1 indicates overwarning of the yes-events. A Bias between 0 and 1 indicates underforecasting.

Two methods for finding a useful probability threshold of the predicted probability often used are based on the CSI and the Bias (Wilks, 2006). When the CSI is used, the probability threshold which maximizes the CSI is selected, while using the Bias the probability threshold which produces a Bias closest to 1 is used. Objective of this research is to decrease FAR and to increase POD. However, a decrease in FAR is accompanied with a decrease in POD. In this study, priority is given to an increase of the POD and therefore to accept an increase in the FAR. This will lead to overwarning, but is considered to be safer to aviation than underwarning. Since the maximum CSI and Bias closest to 1 do not necessarily occur at the same probability threshold, both CSI and the Bias, with respect to the POD and FAR, will be examined to find the optimal probability threshold.

5th Chapter

RESULTS

This chapter describes the results obtained from the convective cloud mask and the logistic regression analysis. The Cb/TCu cloud detection method is developed using the training dataset and is validated using the validation dataset.

5.1 CONVECTIVE CLOUD MASK

Investigation of the different threshold combinations of the MSG-SEVIRI cloud physical properties and HRV reflectance and the requirement of at least 95% retained yes-events (in the training dataset) yielded the following 'best' threshold combination as shown in Table 5.1.

Pixels passing the CCM represent clouds that have a maximum cloud top temperature of 275 K, a minimum optical thickness of 10, a minimum effective radius of 12 μm for liquid water droplets or presence of ice crystals in the cloud top and a minimum cloud albedo of 60%. The standard deviation of the HRV within the box should be 0.025 minimum. A cloud top temperature threshold of 275 K does not seem very strict, since it is a few degrees above zero. However in summer, cloud top temperatures will be higher at same heights than in winter. Clouds with an optical thickness > 8 are considered thick clouds. The effective radius of 12 μm is close to the threshold of 14 μm ,which is often considered to be the threshold at which particles have grown large enough to initiate the precipitation process, see Chapter 3. The HRV reflectance is well above the 40% threshold value used in the convective cloud mask for detection of convective initiation (not full-grown TCU or Cb clouds) of Mecikalski and

Table 5.1: Best threshold combination CCM.

CTT	COT	REFF	HRV	HRV std
275 K	10	12 μm	0.6	0.025

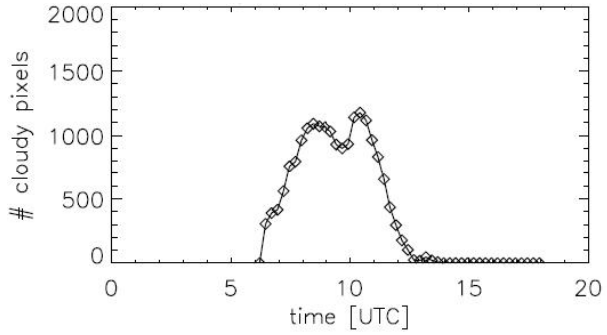

Figure 5.1: Number of convective cloudy pixels within the MSG box area per time step for 7 August 2004.

Bedka (2006), see Chapter 3. It is below reflectance values usually assumed for thick convective clouds (>80%).

For the training dataset, this best threshold combination resulted into the retainment of 96,5% of the yes-events and 34,3 % of the non-yes-events. For the validation dataset, 95.9% (53 out of 54 days with yes-events) of the yes-events pass the CCM while it is only 35,3% of the non-events. With a POD of 95.9% for the yes-events, the FAR and CSI become 74.54 % and 25.18 %, respectively. The total time steps of 11928 have been reduced by 60%, leaving 4887 time steps which are assigned a hazard map (1173 yes-events and 3714 non-events). From the hazard maps, the probability of risk is determined in the second step of the Cb/TCu cloud detection method.

On average 17,6% of the pixels in the MSG box area pass the CCM. For yes-events passing the CCM the average cloudy pixel percentage is 21,7%, while for non-events it is 16,3%. The average of the percentage of cloudy pixels is highest for time steps in the late morning (10-12h) for yes-events (24,6%) and is lowest for time steps in the early morning (6-10h) for non-events (15,0 %). The 4% of the yes-events that do not pass the CCM mostly occur on different days. Relatively many non-events have been filtered out after 15 p.m. and between 8 and 10 a.m.

The day 7 August 2004 is presented to demonstrate the Cb/TCu cloud detection method. On these day two Cb reports were made, one at 10.55 a.m. and one at 11.25 a.m.. These yes-events are part of the validation dataset. A number of thunderstorms have been reported in the southern half of the Netherlands during the morning (Weerspiegel, Aug 2004). Fig. 5.1 shows a graph of the number of pixels passing the CCM during the day, with a maximum around 11 a.m.. This maximum coincides well with the time of the Cb reports. Fig. 5.2 shows the pixels that pass the HRV reflectance threshold, CTT threshold and COT threshold at 10.56 a.m. The lower right image shows the result of the CCM. About 55 % (1118) of the pixels passed the CCM. Together, these cloudy pixels construct the hazard map for that specific time step. The level of risk for the hazard map is determined in the second step of the Cb/TCu cloud detection method.

Radar data within the MSG box area show that over 300 cloudy pixels have

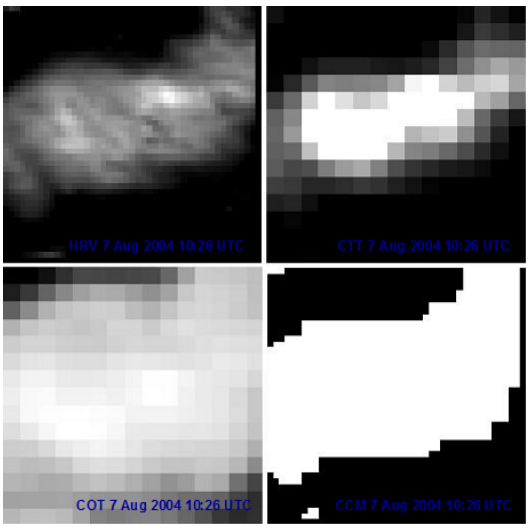

Figure 5.2: An example of the CCM for 7 August 2004 at 10:26 UTC. The HRV mask (upper left), the CTT mask (upper right), the COT mask (lower left) and the end result of the CCM (lower right) are shown.

dBZ values above 30 dBZ and 19 pixels have dBZ values above 40 dBZ, indicating moderate to heavy rain rates, see subsection 2.2.4. Fig. 5.3 shows rain rates derived from radar reflectivity data. An area of moderate to heavy rain rates is located over Schiphol and seems to coincide well with the cloudy pixels in the CCM, keeping in mind the parallax effect for satellite data. Data from the lightning detection network shows that 24 flashes have been detected within the MSG box area over the last 10 minutes.

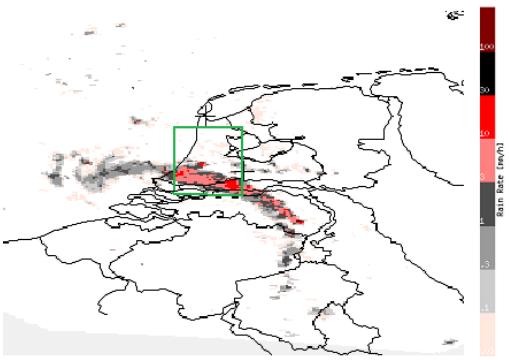

Figure 5.3: Rain rates (mm/h) developed from radar reflectivity data on 7 August 2004 at 10.25 UTC (KNMI weather radar). The green lines indicate the MSG box area around Schiphol.

5.2 LOGISTIC REGRESSION

The construction of a logistic regression model has been performed in 3 steps. The first step only considers potential predictors derived from the MSG-SEVIRI cloud physical properties and HRV reflectance. The second step also includes a HRV cloud optical thickness. In the third step, lightning and weather radar data are included as well.

5.2.1 STEP 1: MSG-SEVIRI CLOUD PHYSICAL PROPERTIES AND HRV REFLECTANCE

Forward stepwise selection method is performed over 100 times for randomly selected parts (25%) of the training dataset as well as for parts of the dataset sorted by day-of-time and day-of-year. The predictors derived from the HRV reflectance are selected most frequently. In fact, the HRV range predictor is chosen >95% of the time. It is followed by the REFF median, CTT range and CTT median predictors (all >75%). Predictors derived from COT and LWP were selected least frequently and about 20 % of the predictors have not been selected at all. The forward stepwise selection method did not show any significant difference in the set of selected predictors for different periods during the day (morning, midday, afternoon) or the year (spring, early summer, late summer).

Performing logistic regression on the complete training dataset and using the likelihood ratio test reveals that the HRV range predictor leads to the largest significant reduction in the -2LL value. It is again followed by the REFF median, CTT range and CTT median, see Table 5.2. Comparing nested models shows that a number of other predictors show a significant statistic in the likelihood ratio test and an increase in the explained variance (Nagelkerke's R^2).

For the four most frequently selected predictors, the Hosmer-Lemeshow test shows significant statistics ($P < 0.05$), which states that the model does not adequately fit the data. However, when the number of cases is randomly reduced by 50%, the Hosmer-Lemeshow statistic always becomes non-significant. Despite the fact that more predictors contribute to a significant contribution to the -2LL value, the maximum number of predictors is limited in order to

Table 5.2: The comparison of nested models for the four most frequently selected predictors in the forward stepwise selection method.

	-2LL	N. R^2	H.&L. stat.	ROC (val=1)
Constant-only	3822,953	-	-	-
+ HRV range	3098,901	0.281	0.000	0.818 (0.802-0.833)
+ REFF median	2994.378	0.300	0.000	0.817 (0.801-0.833)
+ CTT range	2923.893	0.341	0.000	0.826 (0.810-0.843)
+ CTT median	2877.675	0.356	0.003	0.834 (0.818-0.850)

prevent the problem of over-fitting. Furthermore, a large number of sets of MSG-SEVIRI derived predictors might result into (near) equally performing models, since all cloud physical properties and the HRV reflectance have a scientific relation to the predictand. Due to correlations among the predictors, several subsets of predictors may essentially give similar information about the predictand. Therefore, as a final set of predictors, the set consisting of the four most frequently selected predictors (as listed in Table 5.2) is chosen, and the subsequent logistic regression function is examined more closely.

First, the linearity in the logit for the continuous independent variables has been checked. Fig. 5.4 shows graphs were the regression coeffiecients for the last three quartiles (taking the first quartile as a reference state with a regression coefficient of zero) are plotted aginst the mid-points of the four quartiles. For linearity in the logit, the increase/decrease of the regression coefficient should be linear with the mid-points of the quartiles. The HRV range and CTT range predictors show reasonable linearity and significant regression coefficients according to the -2LL and Wald statistics. The J-shaped curve of the REFF median predictor shows the existence of a turning point. The regression coefficient changes from a negative to a positive sign, which means that the predictand becomes inversely related to the predictor above a certain point. To overcome the non-linearity with the logit for a continuous indepedent variable, it can be converted into a categorical variable whereby seperate regression coefficients are calculated for the different categories. For the REFF median predictor, the regression coefficients of the second and third quartile have non-significant -2LL and Wald statistics and therefore are removed from the logistic regression model. This means that only for cases with high median values in the REFF (above $\approx 16\mu$m), the predictor contributes (positively) to the logistic regression function. The regression coefficients of the CTT median quartiles all have negative values, but do not show linearity with the logit. Now only the first quartile has a significant -2 LL and Wald statistic and the other two regression coefficients are also removed from the model.

In terms of the logit transformation the logistic regression function looks as follows:

$$ln\left[\frac{P(y)}{1-P(y)}\right] = -2.333 + 0.063 * x_1 + 1.222 * x_2 + 0.044 * x_3 - 0.494 * x_4 \quad (5.1)$$

where x_1, x_2, x_3 and x_4 represent the independent variables HRV range, REFF median, CTT range and CTT median respectively, as listed in Table 5.3. The sixth column lists the 95% confidence intervals of the regression coefficients. The third column shows the value of the Wald test and the fourth column its significance statistics. All four predictor have a significant (statistics < 0.05) contribution to the model. This is also reflected by the values in the sixth column, which lists the 95% confidence intervals of the regression coefficients. For non of the regression coefficients the value 1 is included within their confidence interval.

The first term on the R.H.S. of Eq. (5.1) is the constant of the model. The HRV range, REFF median and CTT range show an increase in the odds for a one unit increase. The positive relation of the HRV range to the predictand is possibly

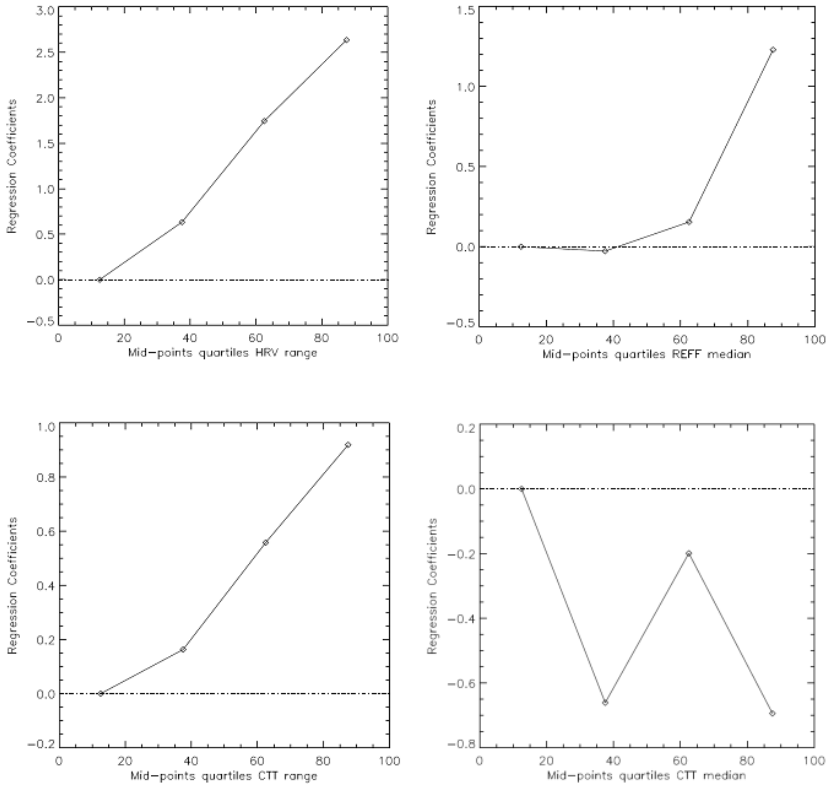

Figure 5.4: Linearity check for the four predictors of step 1 with respect to the regression coefficients of the quartiles. The dotted line represents the zero regression coefficient (first quartile) line.

related to the shadow effects at convective cloud tops. Due to the bulbuous towers or overshooting tops, some parts of the cloud tops will have a reflectance close to one (or 100 %) for the sun-satellite geometry. Other parts of the cloud top will be located in shadowed areas and therefore will have low reflectance values. The increase of reflectance in certain areas and the decrease of reflectance in other areas leads to a larger HRV range value. Also the presence of convective clouds in different stages of convective development in a satellite image may lead to larger ranges. The REFF median is positively related to the predictand for high values (> 16 μm). This means that for clouds already exibiting areas with particles with relatively large effective radius, an increase of the area with larger particles or an increase of the effective radius will lead to an increase in odds of the yes-event (Cb/TCu present) occuring. The relatively large particles may be related to the presence of relatively large ice crystals (here between 6 and 51μm) in the cloud top, especially in the convective regions (not the anvil). A large CTT range may also be evidence of variation in cloud top heights, for example the difference between the temperature of the overshooting top and lower clouds within the MSG box area. The overall cloud top temperature however, should decrease when convective clouds are present within the MSG box area. This can be seen by the negative relation of the CTT median to the predictand.

Table 5.3: Regression coefficients and their statistics for the training dataset: step1

	a	Wald	Sig.	Exp(a)	C.I. 95%
x_1: HRV range	0.063	283.354	0.000	1.065	1.057-1.072
x_2: REFF median	1.222	116.772	0.000	3.395	1.037-1.053
x_3: CTT range	0.044	142.681	0.000	1.045	2.778-4.149
x_4: CTT median	-0.494	16.795	0.000	0.610	0.482-0.773

In terms of odds and probabilities, the function can be understood as follows. For the HRV range (reflectance in %) an increase of 10 % in reflectance, with other variables held constant, results into an increase in the odds of the event occuring by a factor of $exp(0.063)^{10} = 1.88$. For CTT range an increase of 10 K is an increase in odds by a factor of $exp(0.044)^{10} = 1.55$. For the REFF median and CTT median predictors the odds change by a factor of $exp(1.222)^1 = 3.39$ and $exp(-0.494)^1 = 0.610$ when values are within the third and first category, respectively. A HRV range of 30%, a CTT range of 40 K, a REFF median of 18 μm and a CTT median of 250 K within the MSG box area result into odds of 12.67 and a subsequent probability of 92.7%.

The 6 possible interaction terms have been investigated, but non were considered to have a significant contribution to the logistic regression model. The statistics of the final logistic regression models are shown in Table 5.4.

Table 5.4: Statistics of the final logistic regression model for the training dataset: step 1

-2LL	N. R^2	H.&L.	ROC
2843.713	0.367	0.001	0.823

The area under the ROC curve has a value of 0.823 (95% confidence interval: 0.797-0.848) for the validation dataset, which can be considered excellent discrimination according to Hosmer and Lemershow. Table 5.5 shows the Brier and Brier skill score. The Brier skill score is clearly positive indicating skill over sample climatology.

Fig. 5.5 shows the frequency histogram of the predicted probabilities for the validation dataset. The predicted probalities have been divided into deciles. A

Table 5.5: Brier score and Brier skill score for the validation dataset: step 1

BS	BSS	REL	RES	UNC
0.139	0.455	0.004	0.055	0.190

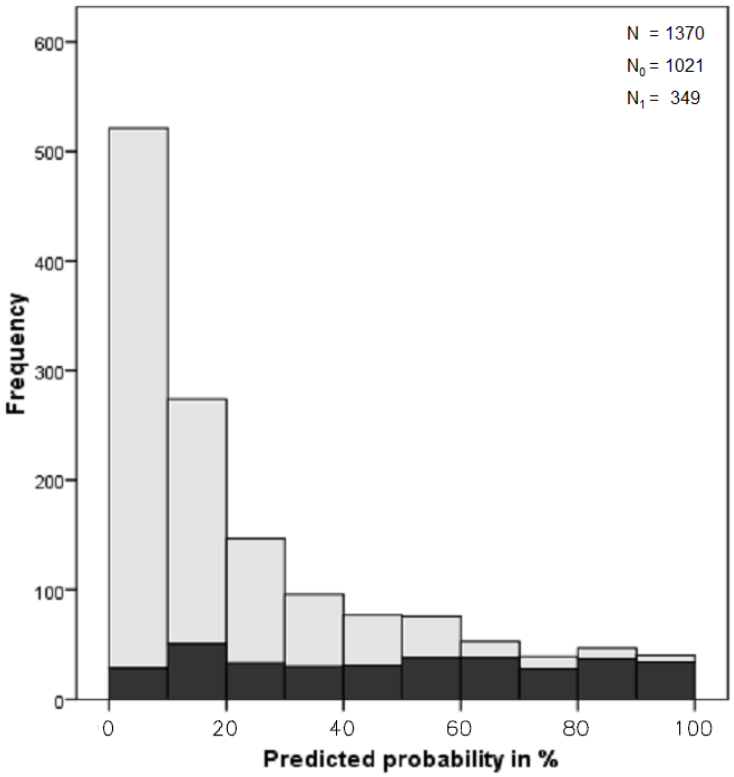

Figure 5.5: Histogram of the predicted probabilities for the validation dataset: step 1. The light grey bars show the frequency distribution of the predicted probabilities for the non-events. The dark grey bars show the frequency distribution of the predicted probabilities for the yes-events. N, N_0 and N_1 are the total number of events, non-events and yes-events, respectively.

desired U-shape (larger bins at lower and higher deciles) is not visible. This is often the case when yes-events are relatively rare. The predicted probabilities of the yes-events do not show a tendency towards the higher values. However, for the higher predicted probabilities the relative frequency of the yes-events is larger than the frequency of the non-events. Furthermore, over more than a half of the non-events is located within the 0-10 % bin and over more than three quarters is located within the 0-20 % bins.

The attributes diagram in Fig. 5.6 compares the predicted probabilities to the observed relative frequencies. The predicted probabilites have been divided into deciles, and the numbers within brackets in the diagram represent the number of cases within each decile bin. The no-resolution line relates to the Resolution term of the BSS and represents the level of the sample climatology. Points in the attributes diagram that have a relatively large distance to that line will have large contributions to the Resolution. The no-skill line is midway between the 1:1 perfect-reliability and no-resolution line. Points that are closer to the perfect-reliability line than to the no-resolution line contribute positively to detection skill. Here, the subsamples show good Resolution and all have

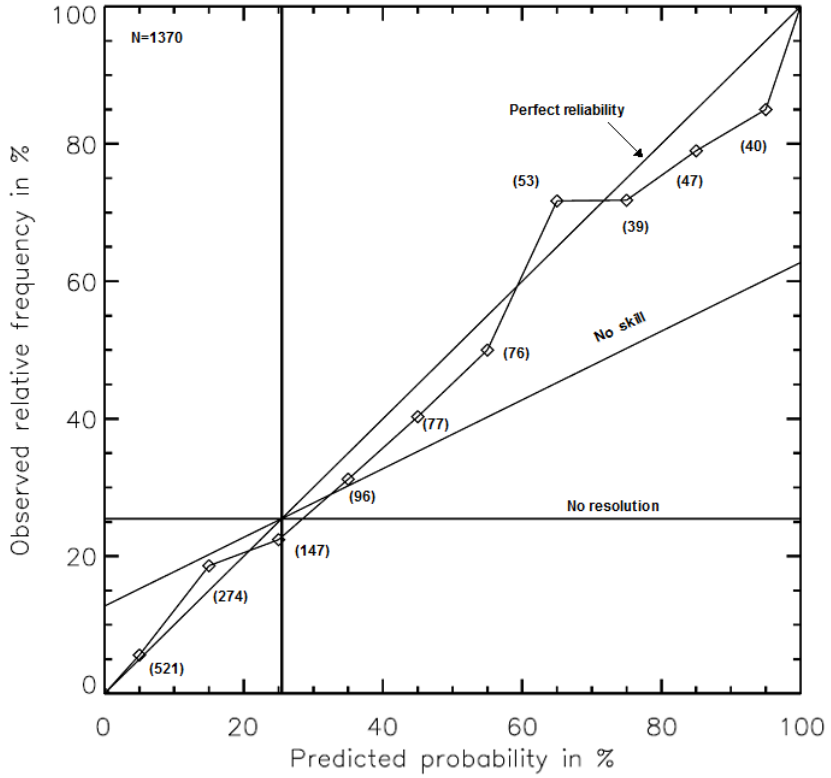

Figure 5.6: Attributes diagram for the validation dataset: step 1. The number in the brackets represent the number of events found in the decile. N is the total number of events.

a positive contribution (Resolution $>$ Reliability). Most points lie to the right of the perfect-reliability line indicating that the predicted probabilities are too large relative to the observed relative frequency. The average predicted number of the yes-events is larger than the observed number of yes-events, which signals overwarning (Bias 1).

A probability threshold is used to convert the predicted probabilities into the dichotomous predictand: presence or absence of Cb/TCu clouds within the MSG box area at a given time step. Fig. 5.7 presents several verification scores for probability thresholds between 5 % and 95 %, as well as the dependence of CSI on FAR and bias. Cases with predicted probabilites below the probability threshold are labeled as non-events, while cases with predicted probabilites above the probability threshold are labeled as yes-events. The POD and FAR decrease for increasing probability thresholds. The ACC reaches maximum values at probability thresholds around 50-60 %. The CSI has a maximum value of 44.8 % at a probability threshold of 35 %. At this probability threshold the Bias, with a value of 1.05, is closest to 1. The value indicates slight overwarning for the yes-events. The corresponding ACC, POD and FAR are 80.1 %, 63.3 % and 39.6 %, respectively. Finally, the results from the logistic regression model have to be combined with the results from the CCM. This leads to a final POD of 60.7 % and a FAR of 39.6 %.

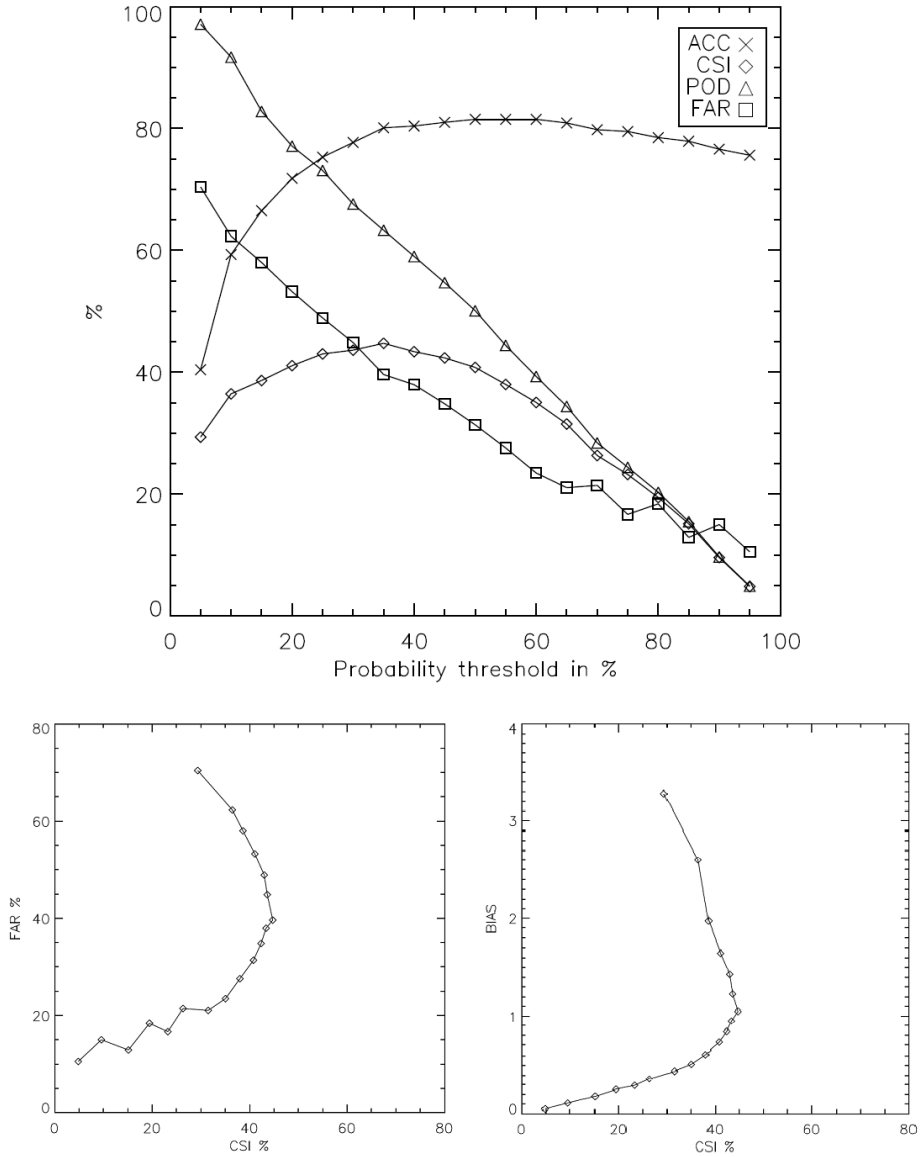

Figure 5.7: Verification scores for the validation dataset: step 1. The upper panel shows several verification scores as a function of probability threshold (5 % to 95 % in steps of 5 %). The lower left panel shows FAR as a function of CSI for several probability thresholds. The lower right panel shows Bias as a function of CSI for several probability thresholds. For the two lower panels, the probability threshold increases from upper to lower points.

5.2.2 STEP 2: HRV-COT

The frequent selection of the HRV derived predictors in the previous section very possibly reflects the importance of a high spatial resolution in satellite images. The frequent selection of the HRV range can be understood by looking at high resolution satellite images in the visible, see Fig. 2.2 and Fig. 2.6. Convective clouds exhibit geometrical structures (bulbuous towers) that cause shadow effects due to differences in height. When looking from a satellite (with a certain angle) at the top of these clouds, very bright and also some dark areas will be visible. The difference between the maximum reflectance (in highlighted areas) and the minimum reflectance (in shadowed areas) will be large. Even for mature Cb clouds with a relatively flat anvil, dark pixels may be present due to shadow effects caused by an overshooting top. For a layer of non-convective clouds, the cloud tops exhibit less variation in height, therefore creating less shadow effects. The MSG-SEVIRI cloud physical properties are not derived on a high spatial resolution. To investigate the predictor potential that high resolution cloud physical properties might have, an estimated high resolution cloud optical thickness has been derived from the HRV channel.

Performing forward stepwise selection shows that the HRV-COT derived predictors are the most frequently selected predictor. The HRV-COT range is selected most frequently followed by the HRV-COT minimum. Again, CTT median and REFF median are selected over 75% of the times. In contrast, CTT range does not have any significant contribution to the model anymore. The HRV-COT range and minimum and the CTT median and REFF median predictors are included in the logistic regression model. Again the linearity in the logit is checked using dummy variables derived from the quartile values of the predictors. From Fig. 5.8 it can be seen that the HRV-COT range predictor shows an acceptable linear relationship with the logit. The HRV-COT minimum predictor shows a deminishing decrease of the regression coefficient for increasing values and will be converted into a new parametric relationship by taking the square root of the values. The REFF median again shows the J-shaped curve and a significant regression coefficient only for the higher REFF median values. The CTT median does not seem to have a very convincing linear relationship, but shows increasing negative regression coefficents for increasing values of the CTT median and all regression coefficients have significant contribution to the model. Therefore, the CTT median predictor will be left unchanged. No significant interaction terms have been identified.

Table 5.6: Regression coefficients and their statistics for the training dataset: step 2

	a	Wald	Sig.	Exp(a)	C.I. 95%
x_1: HRV-COT range	0.33	201.571	0.000	1.033	1.029-1.038
x_2: CTT median	-0.055	186.273	0.000	0.947	0.930-0.954
x_3: HRV-COT minimum	-0.775	164.430	0.000	0.463	0.412-0.521
x_4: REFF median	1.212	120.971	0.000	3.361	2.708-4.171

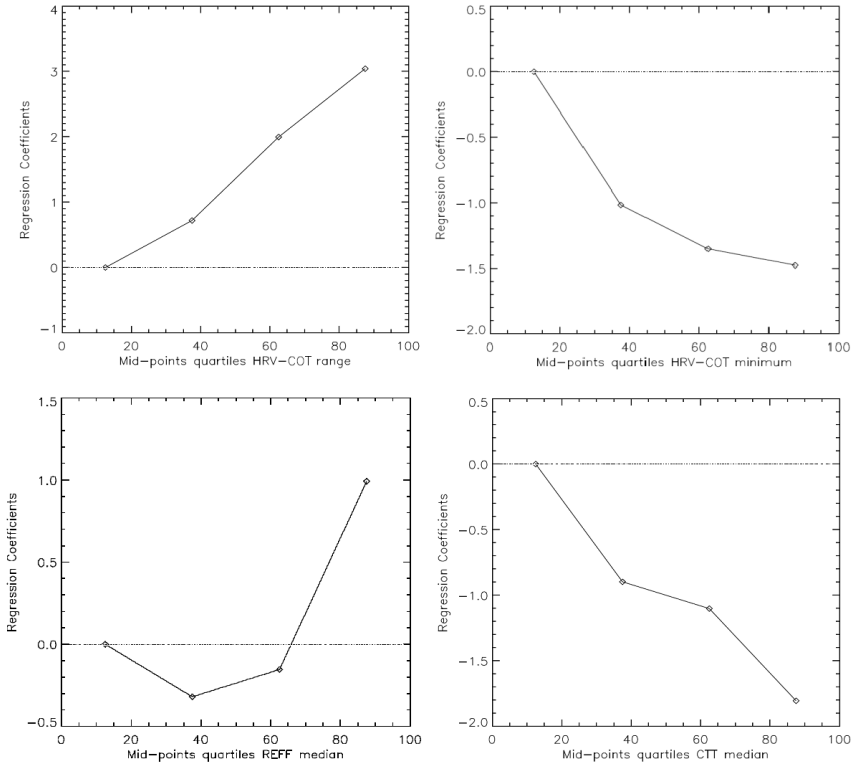

Figure 5.8: Linearity check for the four predictors of step 2 with respect to the regression coefficients of the quartiles. The dotted line represents the zero regression coefficient (first quartile) line.

The regression coefficients of the predictors are shown in Table 5.6. Just as the HRV range predictor, the HRV-COT range predictor has a positive regression coefficient. The REFF median predictor shows a regression coefficient close to the regression coefficient in step 1. The regression coefficient of the CTT median predictor is now much smaller, but still negative. The HRV-COT minimum has a negative regression coefficient, indicating that the odds of the yes-event occuring decrease for an increasing minimum value of the HRV-COT. This may be related to parts of the anvils of Cb clouds, which may have relatively low minimum cloud optical thickness (less dense and thick), see Fig. 2.2.

The statistics of the final logistic regression models are shown in Table 5.7. With respect to step 1, the -2LL decreased and the Nagelkerke's R^2 and value of

Table 5.7: Statistics of the final logistic regression model for the training dataset: step 2

-2LL	N. R^2	H.&L.	ROC
2670.932	0.422	0.146	0.862

Table 5.8: Brier score and Brier skill score for the validation dataset: step 2

BS	BSS	REL	RES	UNC
0.130	0.491	0.005	0.065	0.190

the area under the ROC curve increased, which indicates an improved model performace. Furthermore, the Hosmer-Lemeshow statistic now indicates an adequate data fit of the model. The area under the ROC curve has increased to a value of 0.852 for the validation dataset. The reliability term in the BSS shows a little decrease, however the increase in the resolution term is larger, which results into an increase in the BSS, see Table 5.8.

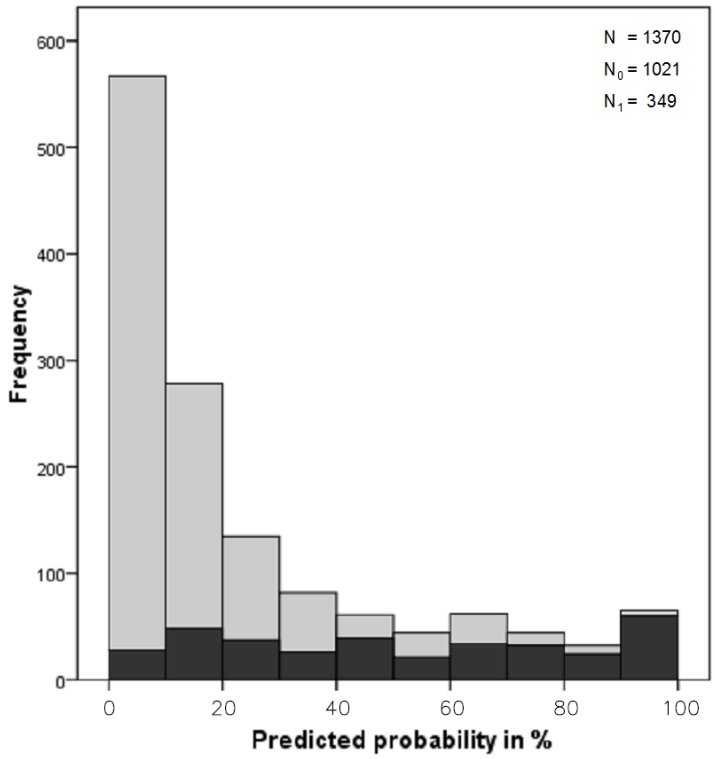

Figure 5.9: Histogram of the predicted probabilities for the validation dataset: step 2. The light grey bars show the frequency distribution of the predicted probabilities for the non-events. The dark grey bars show the frequency distribution of the predicted probabilities for the yes-events. N, N_0 and N_1 are the total number of events, non-events and yes-events, respectively.

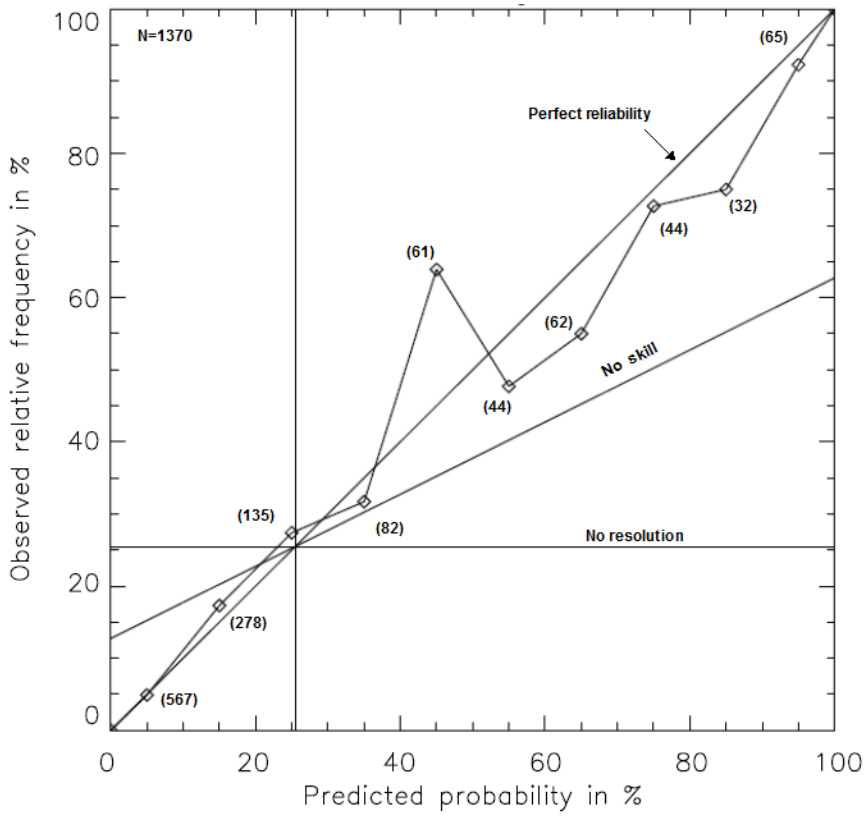

Figure 5.10: Attributes diagram for the validation dataset: step 2. The number in the brackets represent the number of events found in the decile. N is the total number of events.

With respect to the probability histogram of step 1, the predicted probabilities for the yes-events in Fig. 5.9 show more variation between the deciles, especially for higher values of the predicted probabilities. Over 80% of the non-events are located in the two lowest deciles.

The attributes diagram in Fig. 5.10 shows overwarning for the higher predicted probabilities and slight underwarning for the lowest predicted probabilities. A relatively large anomaly can be seen for the fifth decile.

Fig. 5.11 presents the verification scores for probability thresholds between 5 % and 95 %. All verification scores show for increasing probability thresholds the same behaviour as in step 1. A maximum CSI, with a value of 47.5 %, can be found at a probability threshold of 25 %. However, between probability thresholds 25 % and 40 % the CSI changes less then 1 %. For the final results, the probability threshold of 35 % will be taken, since at this value the Bias, which is 0.98, is closest to 1. This Bias indicates very slight underwarning of the yes-events. At this cut-off the CSI and ACC values are 46.1 % and 81.6 %, respectively. This is an increase for both scores with respect to the scores from step 1. The FAR shows a decrease of several percent, while the POD, with a value of 63.0, % is almost unchanged. The decrease in the FAR can also

be understood from a visual inspection of the probability histograms. In the second step, more non-events have moved to the left side of the probability threshold, while the number of yes-events at the right side of the probability threshold almost remained unchanged. Combining the results with the results from the CCM leads to a final POD and FAR of 60.4 % and 35.8 %, respectively.

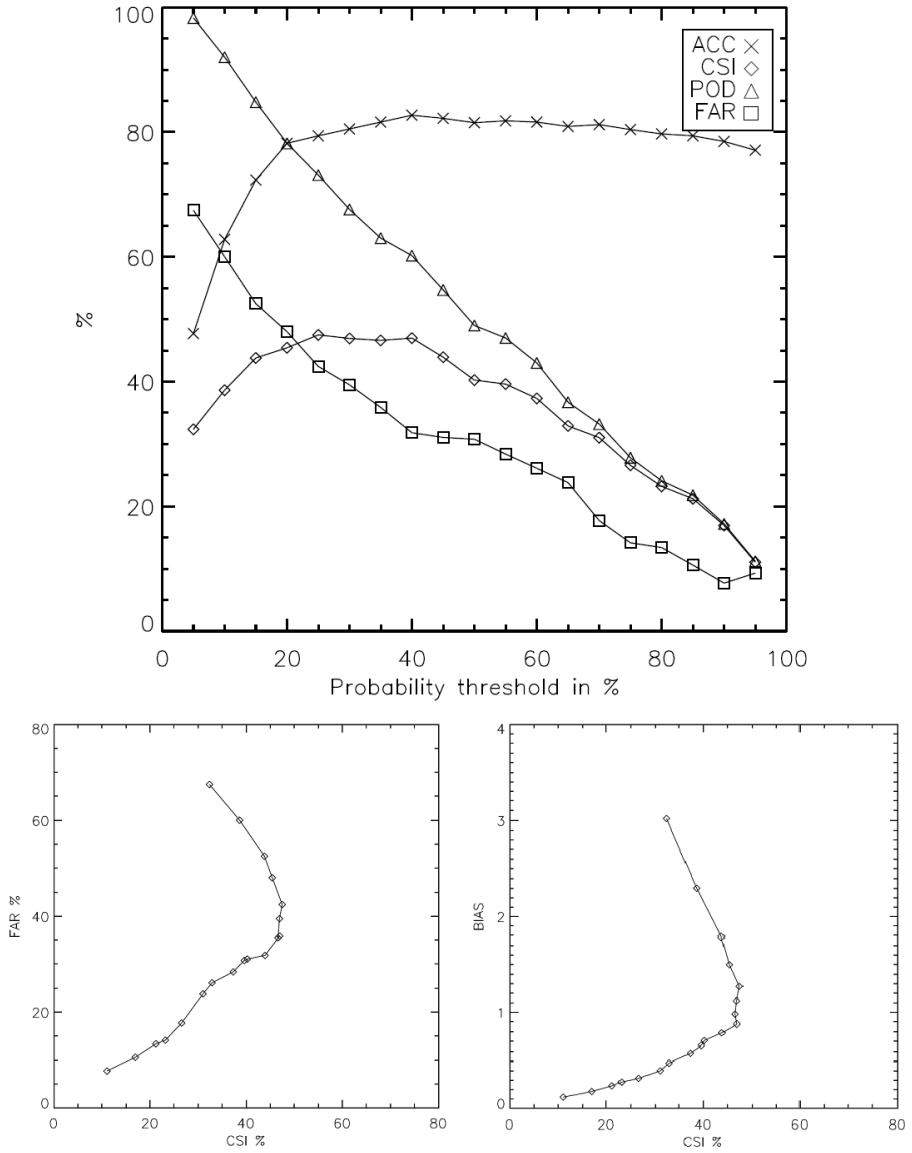

Figure 5.11: Verification scores for the validation dataset: step 2. The upper panel shows several verification scores as a function of probability threshold (5 % to 95 % in steps of 5 %). The lower left panel shows FAR as a function of CSI for several probability thresholds. The lower right panel shows Bias as a function of CSI for several probability thresholds. For the two lower panels, the probability threshold increases from upper to lower points.

5.2.3 STEP 3: RADAR AND LIGHTNING DATA

As a final step in this research, predictors derived from weather radar and lightning data are included in the forward stepwise selection method. Due to errors within the new dataset, the number of available correct cases has been reduced by 16 % (49 days) for the yes-events and 12 % for the non-events.

The forward stepwise selection method revealed that the maximum dBZ value (RR maximum) within the MSG box area is an important predictor within the logistic regression model. In contrast, the lightning derived predictor is selected $< 5\%$ of the time. This is consistent with the results from a KNMI report, which states that data from the lightning detection network had little effect on the performance of the automated detection method (Wauben *et al.*, 2006). Next to the maximum dBZ value, the predictors from the previous step are the most frequently selected predictors. Furthermore, the REFF standard deviation will be included in the model, since now its contribution is considered significant.

The linearity with the logit is checked for the six predictors in the new logistic regression model. The HRV-COT range, HRV-COT minimum, REFF median and CTT median predictors show the same relationship to the logit as in step 2 (not shown). Again only the third category of the REFF median will be included as an predictor. In contrast, now all categories of the CTT median predictor show significant contribution to the logistic regression model and the regression coefficient of the first quartile of the HRV-COT range predictor is non-significant. The HRV-COT minimum is again converted into a new parametric relation by taking the square root of the values. The RR maximum shows the same J-shape curve as the REFF median predictor. The non-linearity with the logit is overcome by only taking the regression coefficient of the fourth quartile (> 31 dBZ) as a predictor. The regression coefficients of the first two quartiles do not show a significant contribution to the model. This means that for a maximum dBZ value above 31 dBZ, the RR maximum predictor has a positive contribution to the calculated probability. It is close to the value of 29 dBZ used in the present KNMI automated detection method. The REFF standard deviation has a possitive regression coefficient for all quartiles, but does not show a linear relationship with the logit. Only the regression coefficient of the first quartile has a significant contribution to the model and will be included in the model. This means that for REFF standard deviations between 1.7 and 3.3 μm, the predictor has a positive contribution in the model, while for values below 1.7 and above 3.3 μm no contribution is made. Too low standard deviation may suggest the presence of homogenous cloud layer such as a layer of thick stratus cloud with high enough reflectance, vertical growth, optical thickness and effective radius to pass the CCM. Convective clouds, especially a mature Cb cloud with anvil, may not have very large spatial variabilities for the effective radius.

The regression coefficients of the predictors are shown in Table 5.9. The HRV-COT minimum and CTT median predictors have similar regression coefficients compared to step 2. However, the regression coefficients of the REFF median predictor decreased a little and the regression coefficient of the HRV-COT increased. The RR maximum predictor is positive which means that for increasing maximum dBZ values within the MSG box area, the odds of the yes-event

Table 5.9: Regression coefficients and their statistics for the training dataset: step 3

	a	Wald	Sig.	Exp(a)	C.I. 95%
x_1: HRV-COT range 1	1.262	64.413	0.000	3.554	2.607-4.845
x_2: HRV-COT range 2	2.050	152.835	0.000	7.700	5.614-10.755
x_3: HRV-COT minimum	-0.61	86.283	0.000	0.538	0.472-0.614
x_4: CTT median	-0.052	131.881	0.000	0.949	0.940-0.957
x_5: REFF median	1.022	63.241	0.000	2.779	2.160-3.575
x_6: REFF std	0.112	22.118	0.000	1.118	1.067-1.171
x_7: RR maximum	1.022	77.852	0.000	2.821	2.241-3.552

occuring increase. The same is true for the REFF standard deviation predictor.

From Table 5.10 it can be seen that model performance increased substantially compared to step 1 and step 2. The -2LL value has made a large decrease and the Nagelkerke's R^2 and ROC value show a relatively large increase. The Hosmer-Lemeshow test statistics indicates that the model adequately fits the (training) data.

Table 5.10: Statistics of the final logistic regression model for the training dataset: step3

-2LL	N. R^2	H.&L.	ROC
2123.154	0.489	0.540	0.882

Again over 80% of the non-events are located in the two lowest deciles. Compared to the predicted probability histograms of step 1 and step 2, more yes-events have moved to the higher predicted probabilities, which indicates better discrimination between the non-events and yes-events.

The area under the ROC curve has a value of 0.872 for the validation dataset, which shows more discriminative power than step 1 and 2. Just as in step 1 and step 2 the values of the area under the ROC curve for the training dataset and validation dataset only differ by a value of about 0.01. This means that the model has near-equal discrimanative power for both training and validation dataset.

The reliability term in the BSS has decreased compared to step 2, leading to an

Table 5.11: Brier score and Brier skill score for the validation dataset: step 3

BS	BSS	REL	RES	UNC
0.123	0.496	0.003	0.065	0.186

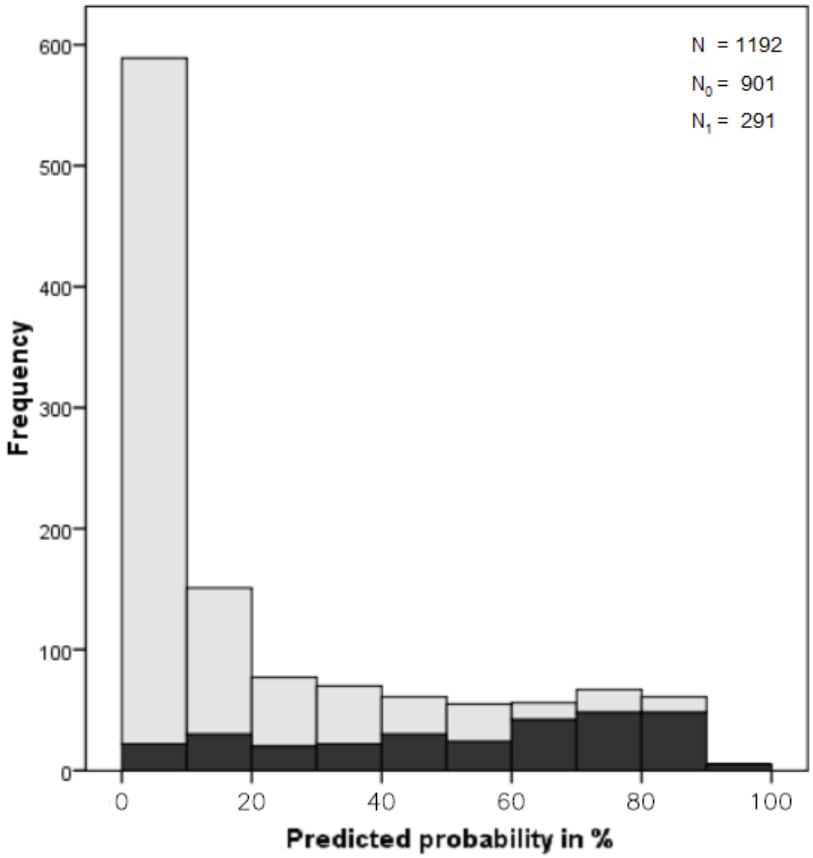

Figure 5.12: Histogram of the predicted probabilities for the validation dataset: step 3. The light grey bars show the frequency distribution of the predicted probabilities for the non-events. The dark grey bars show the frequency distribution of the predicted probabilities for the yes-events. N, N_0 and N_1 are the total number of events, non-events and yes-events, respectively.

increase in the BSS. The resolution is unchanged. However, the reliability and resolution terms from step 3 can not be compared directly to the ones from step 1 and 2 due to a different uncertainty. The BSS shows an increase with respect to the BSS from step 3.

The attributes diagram in Fig. 5.13 shows slight under- and overwarning for different deciles of the predicted probabilities. However, the decrease in the reliability term can be visually seen by noticing that all points are located close to the 1:1 perfect-reliability line. Furthermore, all points have a positive contribution to the BSS over sample climatology.

Fig. 5.14 shows that the maximum CSI, with a value of 49.8 %, is located at a probability threshold of 35 %. However, for this probability threshold the Bias is 1.16, which indicates substantial overwarning. To reduce this overwarning, the probability threshold of 40 % is taken. At this probability threshold, the CSI value (49.4 %) shows a decrease of less then 0.5 %, while overwarning has been

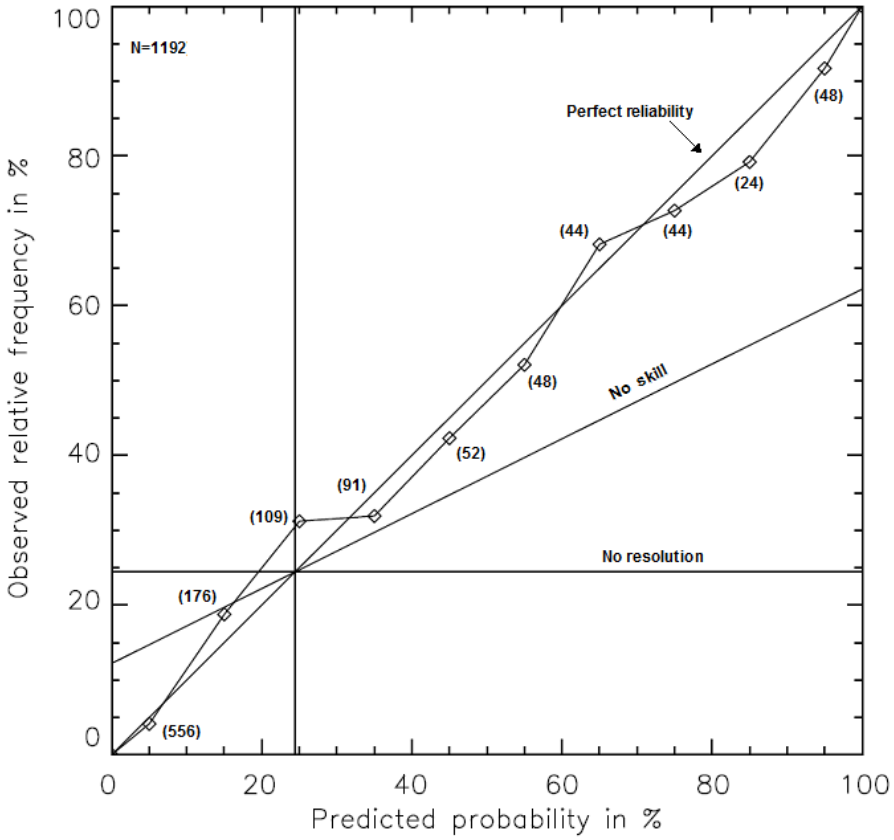

Figure 5.13: Attributes diagram for the validation dataset: step 3. The number in the brackets represent the number of events found in the decile. N is the total number of events.

reduced significantly (Bias=1.05). With respect to step 2, the POD has increased to a value of 67.7 %, while the FAR did not change (35.4 %). Comparing the probability histograms of both steps shows that more yes-events have moved to the right side, explaining the increase of the POD. Combined with the results from the CCM, the Cb/TCu cloud detection method leads to a final POD of 65.2 % for the yes events and a FAR of 35.4 %.

The case study of 7 August 2004 at 10.56 UTC has a predicted probability of 51% when using this logistic regression model. Using a probability threshold of 0.4, the Cb/TCu cloud detection method has identified the pixels in the CCM as Cb/TCU clouds.

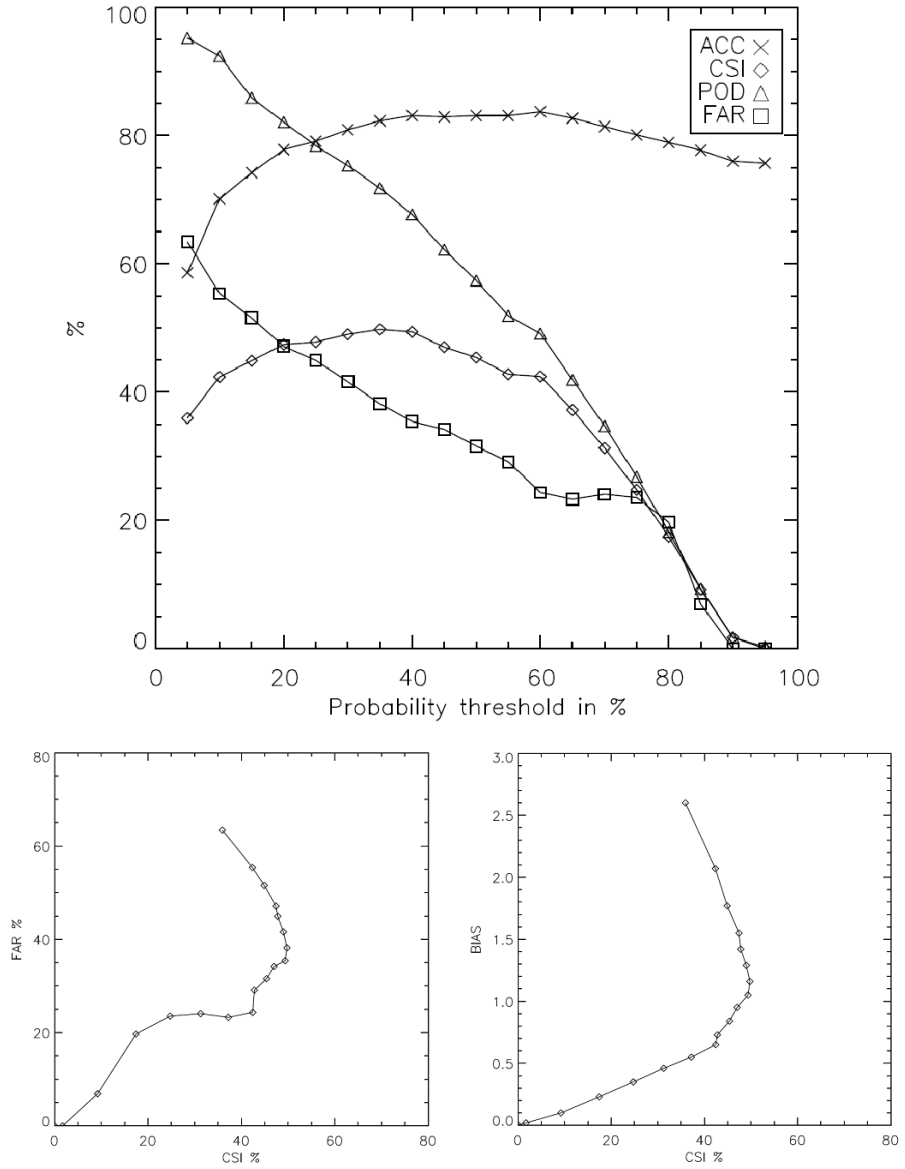

Figure 5.14: Verification scores for the validation dataset: step 3. The upper panel shows several verification scores as a function of probability threshold (5 % to 95 % in steps of 5 %). The lower left panel shows FAR as a function of CSI for several probability thresholds. The lower right panel shows Bias as a function of CSI for several probability thresholds. For the two lower panels, the probability threshold increases from upper to lower points.

5.3 SUMMARY

In Fig. 5.15 values of CSI and Bias are shown as functions of POD and FAR. For the three steps, the four verification scores are shown for six probability thresholds between 25 % and 50 % (increasing probability threshold from upper right crosses to lower left crosses). Best verification scores are located in the upper left corner of the figure near the bias=1 line. The improvement of step 3 over step 1 and 2 can be clearly seen by a shift of the scores towards higher CSI values. The red cross in the figure shows the scores of the present radar-based automated Cb/TCu cloud detection method at the KNMI. However, only one year (2005) of METAR data has been used for verfication. Therefore, the verification scores of the radar-based KNMI detection method might be somewhat different when using other or more METAR data. The green cross indicates the scores that are preferred at the KNMI for a responsible replacement of human observers by an automated detection method at airport weather stations. It can be seen that the verification scores of the new Cb/TCu cloud detection method lie much more to the left and a little above the scores of the present Cb/TCu cloud detection method, showing improvement due to decreasing FAR and increasing POD.

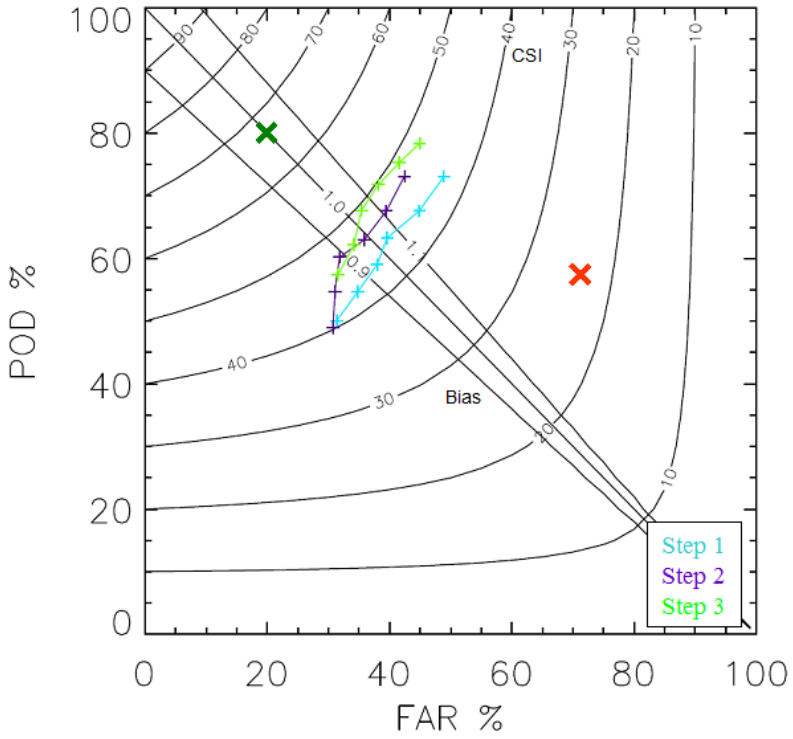

Figure 5.15: CSI (bent contour lines) and bias (straight contour lines) as functions of POD and FAR. The four verification scores for the three steps for six probability thresholds between 0.25 (upper right crosses) and 0.5 (lower left crosses) are shown. Red cross: scores of the present KNMI automated Cb/TCu detection method. Green cross: required scores.

A flow chart of the results of the Cb/TCu cloud detection method for the validation dataset is presented in Fig. 5.16. The research started with 364 avaible yes-events (1) and 2888 non-events (0) for the validation dataset. After the convective cloud mask, 349 (95.9%) yes-events remained and 1022 (35.4%) of the non-events. Combined with the logistic regression model with only MSG-SEVIRI derived cloud physical properties on low spatial resolution results into a POD of 60.7% and FAR of 39.6%. The logistic regression model with the HRV-COT on high spatial resolution reduces the FAR to 35.8 %, while the POD of 60.4 % is nearly the same. The final logistic regression model, which also includes radar data, leads to an increase in the POD, which now is 65.2 %, and a FAR of 35.4%.

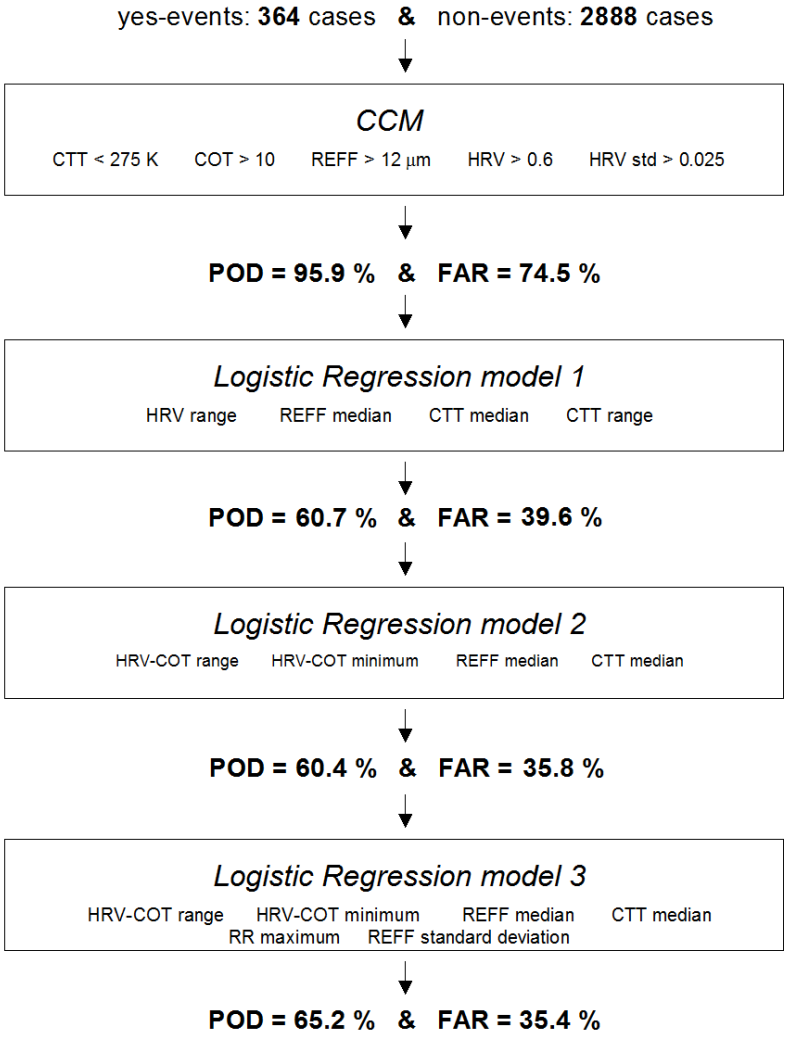

Figure 5.16: Flow chart of the investigated Cb/TCu cloud detection method for the validation dataset.

6th Chapter
Discussion and Conclusion

An automated Cb/TCu cloud detection method has been developed for the coastal area of the Netherlands, centered around Schiphol airport and for daytime summer period, using MSG-SEVIRI derived cloud physical properties, HRV reflectance and weather radar data. The method has been constructed in two steps: the convective cloud mask to construct a hazard map and a logistic regression model to determine the level of risk. This approach is novel with respect to earlier studies in the sense that satellite derived cloud physical properties are directly related, physically and statistically, to the presence of convective clouds in a satellite image. The convective clouds need not to be precipitating clouds.

The convective cloud mask is designed using a thresholding technique for the cloud physical properties and HRV reflectance. Hereby, optically thin and low reflecting clouds with too warm cloud tops and no presence of ice crystals or too small effective radii within the cloud top are filtered out. The mask works well as a first filter since two third of the non-events are removed while over 95 % of the yes-events remain. The hazard map, created by the potential convective cloud pixels, indicates the areas of possible risk. This is the only available information about the location and dimensions of the possible Cb/TCu clouds within the MSG box area. This information is not included in the METAR dataset and can therefore not be verified. In many convective cloud studies, radar data is used to verify satellite detection methods. However, a lack of performance of the KNMI automated Cb/TCU detection method based on radar data has been the motive of this research. Therefore, radar data can not be used for verification, but may serve as an indication of performance, e.g. due to visual inspection. Doing so, one has to keep in mind the parallax effect.

From the cloud physical properties and HRV reflectance of the pixels in the hazard map, a number of potential predictors has been derived. It is assumed that a physical relationship exists between these predictors and the predictand (Cb/TCu clouds) and therefore logistic regression is used to determine the level of risk for the hazard map. It is very likely that several subsets of predictors have near equal performance due to correlations among the predictors. Therefore, forward stepwise selection method is used to reveal a well-performing and independent set of predictors. The frequent selection of the HRV reflec-

tance predictor over the predictors derived from the cloud physical properties indicates the importance of satellite data on high spatial resolution. This has been confirmed by the frequent selection of the HRV derived COT on high resolution. Adding radar data as a predictor showed an increase in model performance with respect to the first two models. The Hosmer-Lemeshow test and area under the ROC curve show adequate data fit for the final model and excellent discriminative power. Furthermore, the difference in model performance between the training and validation dataset is very small, indicating that no over-fitting occurred. A few predictors have been given new parameterisations or have been categorized to increase the statistical relationship between the predictors and the predictand. The Brier skill score is clearly positive, due to both good reliability and good resolution. This can also be seen in the attributes diagram. This shows positive skill of the predicted probabilities with respect to sample climatology. The optimal probability threshold, with large CSI and bias close to 1, are located between 25 % and 40 % due to a large number of non-events ($> 75\%$) that have low probabilities (0-20 %) and the spread of yes-events over all probability deciles.

The use of data from numerical weather prediction models (convective indices such as CAPE), lidar, data from soundings, and ww codes to define a predictand has been rejected. The METAR dataset is considered to give the best information about the presence of Cb/TCu clouds at and within the vicinity of Schiphol airport and is therefore chosen as 'ground truth'. However, despite the fact that reports are made by professional meteorological observers, uncertainties remain. The reports are made by at least ten different human observers and are mainly based on visual inspection. Therefore, reports are subject to the opinion of the present observer. Opinions may differ on the maximum distance of convective clouds at which a report should be made. Also the timing of the reports may differ since no exact rules exist on the time of transition of a cumulus cloud into a towering cumulus and a towering cumulus into a cumulonimbus cloud. Furthermore, errors may arise from the matching of the MSG time steps to the METAR time steps and the requirement of at least 10 pixels in the hazard map. Small convective clouds may not pass the convective cloud mask. The skill of the model may also be influenced by the MSG box area size, which is likely to be larger than the viewing/reporting range of the observer, and the parallax effect. These might lead to weaker statistical relationships between the predictors and the predictand.

The obtained thresholds in the convective cloud mask and the set of predictors and their regression coefficients in the logistic regression model may differ for different regions, time-of-day and time-of-year. For example, the aerosol distribution around Schiphol may be different compared to the aerosol distribution in other parts of the country due to presence of sea particles or even particles from contamination produced by air planes. This has a direct and indirect effect on the effective radius, optical thickness and reflectance. For night time detection, the HRV reflectance can not be used in the set of predictors. Furthermore, relationships between the predictors and the predictand may be different in winter time.

From the verification results obtained in this study it can be concluded that a good first step of improvement has been made. The POD of 65.2 % shows an

increase with respect to the POD of 58 % for the KNMI Cb/TCu cloud detection method. The FAR of 35.4 % has been decreased by a half with respect to a FAR of 70%, which is a substantial reduction. However, for a responsible replacement of human observers by an automated Cb/TCu cloud detection method at airports, a POD of at least 80% and a maximum FAR of 20% is required.

Several things can be done to improve the Cb/TCu cloud detection method in future studies. For a more effective use of the spatial variability that convective clouds exhibit in satellite images, the MSG-SEVIRI cloud physical properties should be retrieved on the high spatial resolution. At presence, the retrieval of high resolution cloud physical properties is not possible. Also, new predictors can be derived from trends in time of cloud physical properties (e.g. decrease in cloud top temperature, which indicates vertical growth), using a cloud-tracking algorithm. Furthermore, useful predictors (e.g. CAPE) might be derived from data from numerical weather prediction models and soundings. Persistence, whereby present detection is related to previous observations, might also be very useful to take into account in future model development. Finally, the effect of the choice of the MSG box area size on the model performance can be investigated.

Acknowledgements. First of all, I would like to thank Rob Roebeling and Erwin Wolters for supervising my Master research. It was great working with you and I really enjoyed my time at the KNMI! I am excited that I can stay a bit longer now. I also thank Geert-Jan Roelofs for supervising my Master thesis on behalf of IMAU. Further, from the KNMI I thank Maurice Schmeits for helping me out with logistic regression and supervising the logistic regression section of the Master thesis, Iwan Holleman for providing radar data and Wim de Rooy for supervising my thesis section about convective clouds. I would also like to thank Joop Konings, Paul de Valk and Rudolf van Westrhenen from the KNMI for their general interest in my Master research. Furthermore, I thank Jan Hemink for contacting Joost Postma, who I thank for having me over at the Schiphol weather station and showing me around. I am very grateful to my mother, who has always been a great support and provided me with a carefree and joyful student life. Thanks! My father has given me the 'science genes' and tried to teach me about science from early on. Although I haven't been always that pacient to listen to all explanations, gracias! Finally, I would like to thank Niels for being a great roommate at the KNMI, Tim for helping me out with Latex and Hans for his everlasting trust in me!

A List of Acronyms and Abbreviations

ACC	ACCuracy
AVHRR	Advanced Very High Resolution Radiometer
BS	Brier Score
BSS	Brier Skill Score
BT	Brightness Temperature
BTD	Brightness Temperature Difference
CAPE	Convective Available Potential Energy
Cb	Cumulonimbus
CCN	Cloud Condensation Nuclei
CIN	Convective INhibition
COT	Cloud Optical Thickness
CPH	Cloud (thermodynamic) PHase
CPP	Cloud Physical Properties
CSI	Critical Succes Index
CTT	Cloud Top Temperature
DAK	Doubling Adding KNMI
ESA	European Space Agency
EUMETSAT	EUropean METeorological SATtellite organisation
FAR	False Alarm Rate
GOES	Geostationary Operational Environment Satellite
HRV	High Resolution Visible
IR	InfraRed
KNMI	Koninklijk Nederlands Meteorologisch Instituut
LCL	Lifting Condensation Level
LFC	Level of Free Condensation
LUT	Look Up Table
LWC	Liquid Water Content
LWP	Liquid Water Path
(AUTO) METAR	(AUTO) METeorological Aerodrome Reports
MODIS	MODerate resolution Imaging Spectroradiometer
MSG	Meteosat Second Generation
NASA	National Aeronautics and Space Administration
NIR	Near-InfraRed

NOAA	National Oceanic and Atmospheric Administration
POD	Probability Of Detection
REFF	EFFective Radius
ROC	Receiver Operating Characteristic
RTM	Radiative Transfer Model
SAF (CM)	Satellite Application Facility (Climate Monitoring)
SEVIRI	Spinning Enhanced Visible and InfraRed Imager
TCu	Towering Cumulus
UTC	Coordinated Universal Time
VIS	VISible
WV	Water Vapour

Bibliography

Abbott (1996). *http://www.tulane.edu/ sanelson/geol204/exceptweath.htm*.

Adler, R. and Negri, A. (1988). A satellite infrared technique to estimate tropical convective and stratiform rainfall. *Journal of Applied Meteorology*, **27**(1), 30–51.

Amato, U., Antoniadis, A., Cuomo, V., Cutillo, L., Franzese, M., Murino, L., and Serio, C. (2008). Statistical cloud detection from SEVIRI multispectral images. *Remote Sensing of Environment*, **112**(3), 750–766.

Aminou, D. (2002). MSG's SEVIRI instrument. *ESA Bulletin(0376-4265)*, pages 15–17.

Amorati, R., Alberoni, P., Levizzani, V., and Nanni, S. (2000). IR-based satellite and radar rainfall estimates of convective storms over northern Italy. *Meteorological Applications*, **7**(1), 1–18.

Anderson, G., Clough, S., Kneizys, F., Chetwynd, J., and Shettle, E. (1986). AFGL Atmospheric constituent profiles (0-120 km). *AFGL atmospheric constituent profiles (0-120km), by Anderson, GP Hanscom AFB, MA: Optical Physics Division, Air Force Geophysics Laboratory,[1986]. AFGL-TR; 86-0110.. US Air Force Geophysics Laboratory. Optical Physics Division.*

Arkin, P. (1979). The relationship between fractional coverage of high cloud and rainfall accumulations during GATE over the B-scale array. *Monthly Weather Review*, **107**(10), 1382–1387.

Arkin, P. and Meisner, B. (1987). The relationship between large-scale convective rainfall and cold cloud over the western hemisphere during 1982-84. *Monthly Weather Review*, **115**(1), 51–74.

Bennetts, D., McCallum, E., and Grant, J. (1986). Cumulonimbus clouds, an introductory review. *Met. Mag*, **115**, 242–56.

Berendes, T., Mecikalski, J., MacKenzie Jr, W., Bedka, K., and Nair, U. (2008). Convective cloud identification and classification in daytime satellite imagery using standard deviation limited adaptive clustering. *Journal of Geophysical Research-Atmospheres*, **113**(D20), D20207.

Billet, J., DeLisi, M., Smith, B., and Gates, C. (1997). Use of regression techniques to predict hail size and the probability of large hail. *Weather and Forecasting*, **12**(1), 154–164.

Bleeker, W. (1980). *Wolkenatlas*. Koninklijk Nederlands Meteorologisch Instituut.

Bluestein, H. (1993). *Synoptic-dynamic meteorology in midlatitudes. Volume II: Observations and theory of weather systems*. Oxford University Press New York.

Bolliger, M., Binder, P., and Rossa, A. (2003). Tracking cloud patterns by METEOSAT rapid scan imagery in complex terrain. *Meteorologische Zeitschrift (Stuttgart)*, **12**(2), 73–80.

Browning, K., Blyth, A., Clark, P., Corsmeier, U., Morcrette, C., Agnew, J., Ballard, S., Bamber, D., Barthlott, C., Bennett, L., *et al.* (2007). The convective storm initiation project. *Bulletin of the American Meteorological Society*, **88**(12), 1939–1955.

Buishand, T. and Velds, C. (1980). *Neerslag en verdamping*. Koninklijk Nederlands Meteorologisch Instituut.

Byers, H. and Braham, R. (1949). *The thunderstorm: report of the Thunderstorm Project*. US Dept. of Commerce:[for sale by the Superintendent of Docments, US Government Printing Office], Washington, DC.

Chandrasekhar, S. (1960). *Radiative transfer*. Courier Dover Publications.

Dasgupta, S. and De, U. (2007). Binary logistic regression models for short term prediction of premonsoon convective developments over Kolkata (India). *International Journal of Climatology*, **27**(6).

De Haan, J., Bosma, P., and Hovenier, J. (1987). The adding method for multiple scattering calculations of polarized light. *Astronomy and Astrophysics (ISSN)*, **183**(2), 371–391.

Deneke, H. and Roebeling, R. (2009). Downscaling of METEOSAT SEVIRI 0.6 and 0.8 micron channel radiances utilizing the high-resolution visible channel. Submitted to Atmospheric Chemistry and Physics - Papers in Open Discussion.

Doswell, C. (2001). *Severe convective storms*. American Meteorological Society Boston, USA.

Duerr, B., Zelenka, A., Mueller, R., and Philipona, R. (2009). Verification of CM-SAF and MeteoSwiss satellite based retrievals of surface shortwave irradiance over the Alpine region. Accepted for publication in International Journal of Remote Sensing.

Emanuel, K. (1994). *Atmospheric convection*. Oxford University Press, USA.

EUMETSAT (2009). *http://www.eumetsat.int/Home/Main/Access_to_Data/Meteosat_Image_Services/SP_1123237865326*.

Fujita, T. (1981). Tornadoes and downbursts in the context of generalized planetary scales. *Journal of the Atmospheric Sciences*, **38**(8), 1511–1534.

Groenemeijer, P. (2003). Three events of strong deep moist convection in The Netherlands. *KNMI report*.

Hansen, J. and Hovenier, J. (1974). Interpretation of the polarization of Venus. *Journal of the Atmospheric Sciences*, **31**(4), 1137–1160.

Hartmann, D. (1994). *Global physical climatology*. Academic Press.

Hees, v. R. and Lelieveld, J. (2000). Retrieving cloud top structure from infrared satellite data. *Journal of Geophysical Research*, **105**, 15.

Henyey, L. and Greenstein, J. (1941). Diffuse reflection in the Galaxy. *Astrophysical Journal 93*, **70**.

Hess, M., Koelemeijer, R., and Stammes, P. (1998). Scattering matrices of imperfect hexagonal ice crystals. *Journal of Quantitative Spectroscopy and Radiative Transfer*, **60**(3), 301–308.

Heymsfield, A. and Miloshevich, L. (1993). Homogeneous ice nucleation and supercooled liquid water in orographic wave clouds. *Journal of the Atmospheric Sciences*, **50**(15), 2335–2353.

Hogg, W. (1990). Comparison of some VIS/IR rainfall estimation techniques. In *Conference on Satellite Meteorology and Oceanography, 5 th, London, England*, pages 287–291.

Holton, J. (2004). *An introduction to dynamic meteorology*. Academic Press.

Hosmer, D. W. and Lemeshow, S. (2000). *Applied Logistic Regression*. Wiley-Interscience.

Houze, R. A. (1993). *Cloud Dynamics*. Academic Press.

Inoue, T. (1985). On the temperature and effective emissivity determination of semi-transparent cirrus clouds by bi-spectral measurements in the 10 μm window region. *Journal of the Meteorological Society of Japan*, **63**(1), 88–99.

Inoue, T. (1987). A cloud type classification with NOAA 7 split-window measurements. *Journal of Geophysical Research-Atmospheres*, **92**(D4).

Jolivet, D. and Feijt, A. (2003). Cloud thermodynamic phase and particle size estimation using the 0.67 and 1.6 μm channels from meteorological satellites. *Atmospheric Chemistry and Physics Discussions*, **3**(4), 4461–4488.

King, P., Yip, T., and Steenbergen, J. (1989). RAINSAT. A One Year Evaluation of a Bispectral Method for the Analysis and Short-Range Forecasting of Precipitation Areas. *Weather and Forecasting*, **4**(2), 210–221.

King, P., Hogg, W., and Arkin, P. (1995). The role of visible data in improving satellite rain-rate estimates. *Journal of Applied Meteorology*, **34**(7), 1608–1621.

Krauss, T., Sinkevich, A., Veremey, N., Dovgalyuk, Y., and Stepanenko, V. (2007). Study of the development of an extremely high cumulonimbus cloud (Andhra Pradesh, India, September 28, 2004). *Russian Meteorology and Hydrology*, **32**(1), 19–27.

Kurino, T. (1997). A satellite infrared technique for estimating deep/shallow precipitation. *Advances in Space Research*, **19**(3), 511–514.

Lee, J. W. (2006). *http://www.srh.noaa.gov/key/HTML/galleries/Jim_Clouds/CloudTypes/low.html%/*.

Lee, T., Turk, F., and Richardson, K. (1997). Stratus and Fog Products Using GOES-8–9 3.9-μ m Data. *Weather and Forecasting*, **12**(3), 664–677.

Lensky, I. and Rosenfeld, D. (2006). The time-space exchangeability of satellite retrieved relations between cloud top temperature and particle effective radius. *Atmospheric Chemistry and Physics*, **6**, 2887–2894.

Levizzani, V. and Setvák, M. (1996). Multispectral, high-resolution satellite observations of plumes on top of convective storms. *Journal of the Atmospheric Sciences*, **53**(3), 361–369.

Ligda, M. (1953). Horizontal Motion of Small Precipitation Areas as Observed by Radar. *Thesis (PH. D.) Massachusetss Institute of Techonology.*

Liou, K. N. (1992). *Radiation and Cloud processes in the Atmosphere*. Oxford University Press New York.

Lovejoy, S. and Austin, G. (1979). The delineation of rain areas from visible and IR satellite data for GATE and mid-latitudes. *Atmosphere and Ocean*, **17**, 77–92.

Maas, A. (2002). *http://www.knmi.nl/satrep/synmeteo/hoofdstukken/hfst6wolkentype.pdf*.

Macke, A., Mitchell, D., and Bremen, L. (1999). Monte Carlo radiative transfer calculations for inhomogeneous mixed phase clouds. *Physics and Chemistry of the Earth, Part B*, **24**(3), 237–241.

Marshall, J. and Palmer, W. (1948). Relation of raindrop size to intensity. *Journal of Meteorology*, **5**, 165–166.

McCann, D. (1983). The enhanced-V: A satellite observable severe storm signature. *Monthly Weather Review*, **111**(4), 887–894.

McKnight, T. (1990). *Physical Geography*. Prentice Hall, NJ.

Mecikalski, J. and Bedka, K. (2006). Forecasting convective initiation by monitoring the evolution of moving cumulus in daytime GOES imagery. *Monthly Weather Review*, **134**(1), 49–78.

Melani, S., Cattani, E., Torricella, F., and Levizzani, V. (2003). Characterization of plumes on top of deep convective storm using AVHRR imagery and radiative transfer simulations. *Atmospheric Research*, **67**, 485–499.

Menzel, W., Smith, W., and Stewart, T. (1983). Improved cloud motion wind vector and altitude assignment using VAS. *Journal of Applied Meteorology*, **22**(3), 377–384.

Merenti-Välimäki, H. and Laininen, P. (2002). Analysing effects of meteorological variables on weather codes by logistic regression. *Meteorological Applications*, **9**(02), 191–197.

Mie, G. (1908). Pioneering mathematical description of scattering by spheres. *Annalen der Physik*, **25**, 337.

Minnis, P., Liou, K., and Takano, Y. (1993). Inference of cirrus cloud properties using satellite-observed visible and infrared radiances. Part I: Parameterization of radiance fields. *Journal of the Atmospheric Sciences*, **50**(9), 1279–1304.

Minnis, P., Garber, D., Young, D., Arduini, R., and Takano, Y. (1998). Parameterizations of reflectance and effective emittance for satellite remote sensing of cloud properties. *Journal of the Atmospheric Sciences*, **55**(22), 3313–3339.

Moody, E., King, M., Platnick, S., Schaaf, C., and Gao, F. (2005). Spatially complete global spectral surface albedos: Value-added datasets derived from Terra MODIS land products. *IEEE Transactions on Geoscience and Remote Sensing*, **43**(1), 144–158.

Murphy, A. (1973). A new vector partition of the probability score. *Journal of Applied Meteorology*, **12**(4), 595–600.

Nakajima, T. and King, M. (1990). Determination of the optical thickness and effective particle radius of clouds from reflected solar radiation measurements. Part I: Theory. *Journal of the Atmospheric Sciences*, **47**(15), 1878–1893.

Negri, A., Adler, R., and Wetzel, P. (1984). Rain estimation from satellites: An examination of the Griffith-Woodley technique. *Journal of Applied Meteorology*, **23**(1), 102–116.

Nieman, S., Schmetz, J., and Menzel, W. (1993). A comparison of several techniques to assign heights to cloud tracers. *Journal of Applied Meteorology*, **32**(9), 1559–1568.

NOAA (2007). *http://www.erh.noaa.gov/rnk/SKYWARNonline_files/textonly/slide21.html*.

Pankiewicz, G., Johnson, C., and Harrison, D. (2001). Improving radar observations of precipitation with a Meteosat neural network classifier. *Meteorology and Atmospheric Physics*, **76**(1), 9–22.

Platnick, S. (2001). A superposition technique for deriving mean photon scattering statistics in plane-parallel cloudy atmospheres. *Journal of Quantitative Spectroscopy and Radiative Transfer*, **68**(1), 57–73.

Platnick, S., King, M., Ackerman, S., Menzel, W., Baum, B., Riedi, J., and Frey, R. (2003). The MODIS cloud products: Algorithms and examples from Terra. *IEEE Transactions on Geoscience and Remote Sensing*, **41**(2), 459–473.

Postma, J. (2008). *Luchtvaartmeteorologische berichtgeving*. KNMI.

Prata, A. (1989). Observations of volcanic ash clouds in the 10-12 μm window using AVHRR/2 data. *International Journal of Remote Sensing*, **10**(4), 751–761.

Pruppacher, H. and Klett, J. (1997). Microphysics of Clouds and Precipitation. *D. Reidel, Norwell, Mass*.

Purdom, J. (1976). Some uses of high-resolution GOES imagery in the mesoscale forecasting of convection and its behavior. *Monthly Weather Review*, **104**(12), 1474–1483.

Rayleigh, L. (1871). On the scattering of light by small particles. *Philosophical Magazine*, **41**, 447–451.

Reudenbach, C., Heinemann, G., Heuel, E., Bendix, J., and Winiger, M. (2001). Investigation of summertime convective rainfall in Western Europe based on a synergy of remote sensing data and numerical models. *Meteorology and Atmospheric Physics*, **76**(1), 23–41.

Rinehart, R. (2006). *Radar for meteorologists*. Rinehart Publications.

Roberts, R. and Rutledge, S. (2003). Nowcasting storm initiation and growth using GOES-8 and WSR-88D data. *Weather and Forecasting*, **18**(4), 562–584.

Roebeling, R., Berk, A., Feijt, A., Frerichs, W., Jovilet, D., Macke, A., and Stammes, P. (2005). Sensitivity of cloud property retrievals to differences in narrow band radiative transfer simulations. *Scientific Report WR*, **2**.

Roebeling, R., Feijt, A., and Stammes, P. (2006). Cloud property retrievals for climate monitoring: Implications of differences between Spinning Enhanced Visible and Infrared Imager (SEVIRI) on METEOSAT-8 and Advanced Very High Resolution Radiometer (AVHRR) on NOAA-17. *Journal of Geophysical Research*, **111**, D20210.

Roebeling, R., Holtslag, A., Feijt, A., and Stammes, P. (2008). *Cloud Physical Properties Retrieval for Climate Studies using SEVIRI and AVHRR data*. PhD thesis Wageningen Universiteit.

Rogers, R. and Yau, M. (1989). *A Short Course in Cloud Physics*. Pergamon, New York.

Rosenfeld, D. and Gutman, G. (1994). Retrieving microphysical properties near the tops of potential rain clouds by multispectral analysis of AVHRR data. *Atmospheric research*, **34**(1-4), 259–283.

Rosenfeld, D. and Lensky, I. (1998). Satellite–based insights into precipitation formation processes in continental and maritime convective clouds. *Bulletin of the American Meteorological Society*, **79**(11), 2457–2476.

Rossow, W. and Schiffer, R. (1999). Advances in understanding clouds from ISCCP. *Bulletin of the American Meteorological Society*, **80**(11), 2261–2287.

Schmeits, M., Kok, K., Vogelezang, D., and van Westrhenen, R. (2006). *http://www.knmi.nl/research/biennial/05-06_Thunderstorms.pdf*.

Schmeits, M., Kok, K., Vogelezang, D., and van Westrhenen, R. (2008). Probabilistic forecasts of (severe) thunderstorms for the purpose of issuing a weather alarm in the Netherlands. *Weather and Forecasting*, **23**(6), 1253–1267.

Schmetz, J., Tjemkes, S., Gube, M., and Van de Berg, L. (1997). Monitoring deep convection and convective overshooting with METEOSAT. *Advances in Space Research*, **19**(3), 433–441.

Schmetz, J., Pili, P., Tjemkes, S., Just, D., Kerkmann, J., Rota, S., and Ratier, A. (2002). An introduction to Meteosat second generation (MSG). *Bulletin of the American Meteorological Society*, **83**(7), 977–992.

Setvák, M. and Doswell III, C. (1991). The AVHRR channel 3 cloud top reflectivity of convective storms. *Monthly Weather Review*, **119**(3), 841–847.

Setvák, M., Rabin, R., Doswell, C., and Levizzani, V. (2003). Satellite observations of convective storm tops in the 1.6, 3.7 and 3.9 μm spectral bands. *Atmospheric Research*, **67**, 607–627.

Smith, R. (1997). *The physics and parameterization of moist atmospheric convection*. Kluwer Academic Publishers.

Stammes, P. (2001). Spectral radiance modelling in the UV-visible range. In *IRS 2000: Current Problems in Atmospheric Radiation*, pages 385–388.

Stamnes, K., Tsay, S., Wiscombe, W., and Jayaweera, K. (1988). Numerically stable algorithm for discrete-ordinate-method radiative transfer in multiple scattering and emitting layered media. *Applied Optics*, **27**(12), 2502–2509.

Stephens, G., Paltridge, G., and Platt, C. (1978). Radiation profiles in extended water clouds. III: Observations. *Journal of the Atmospheric Sciences*, **35**(11), 2133–2141.

Tag, P., Bankert, R., and Brody, L. (2000). An AVHRR multiple cloud-type classification package. *Journal of Applied Meteorology*, **39**(2), 125–134.

Thies, B., Nauß, T., and Bendix, J. (2008). Precipitation process and rainfall intensity differentiation using Meteosat Second Generation Spinning Enhanced Visible and Infrared Imager data. *Journal of Geophysical Research-Atmospheres*, **113**(D23), D23206.

Thorpe, A. and Miller, M. (1978). Numerical simulations showing the role of the downdraught in cumulonimbus motion and splitting. *Quarterly Journal of the Royal Meteorological Society*, **104**(442).

Tjemkes, S., Van de Berg, L., and Schmetz, J. (1997). Warm water vapour pixels over high clouds as observed by METEOSAT. *Contributions to Atmospheric Physics*, **70**(1), 15–21.

Velden, C., Hayden, C., Nieman, S., Menzel, W., Wanzong, S., and Goerss, J. (1997). Upper-tropospheric winds derived from geostationary satellite water vapor observations. *Bulletin of the American Meteorological Society*, **78**(2), 173–195.

Velden, C., Stettner, D., and Daniels, J. (2000). Wind vector fields derived from GOES rapid scan imagery. In *Conference on Satellite Meteorology and Oceanography, 10 th, Long Beach, CA*, pages 20–23.

Walther, A. (2008). *Radar-based precipitation classification in the Baltic Sea area.* Freie Universität Berlin.

Wauben, W., Baltink, H., de Haij, M., Maat, N., and The, H. (2006). *Status, Evaluation and Developments of the Automated Cloud Observations in the Netherlands*. KNMI TECO.

Weickmann, H. (1949). Die Eisphase in der Atmosphaere. *Bericht des Deutschen Wetterdienstes in der U.S. Zone*, **6**.

Welch, R., Sengupta, S., and Chen, D. (1988). Cloud field classification based upon high spatial resolution textural features 1. Gray level co-occurrence matrix approach. *Journal of Geophysical Research-Atmospheres*, **93**(D10).

Wilks, D. S. (2006). *Statistical Methods in the Atmospheric Sciences*. Academic, New York.

Young, K. (1993). *Microphysical processes in clouds*. Oxford University Press, USA.

Young, L. (2007). *http://perspectivevision.blogspot.com/search?q=clouds*.

Zinner, T., Mannstein, H., and Tafferner, A. (2008). Cb-TRAM: Tracking and monitoring severe convection from onset over rapid development to mature phase using multi-channel Meteosat-8 SEVIRI data. *Meteorology and Atmospheric Physics*, **101**(3), 191–210.

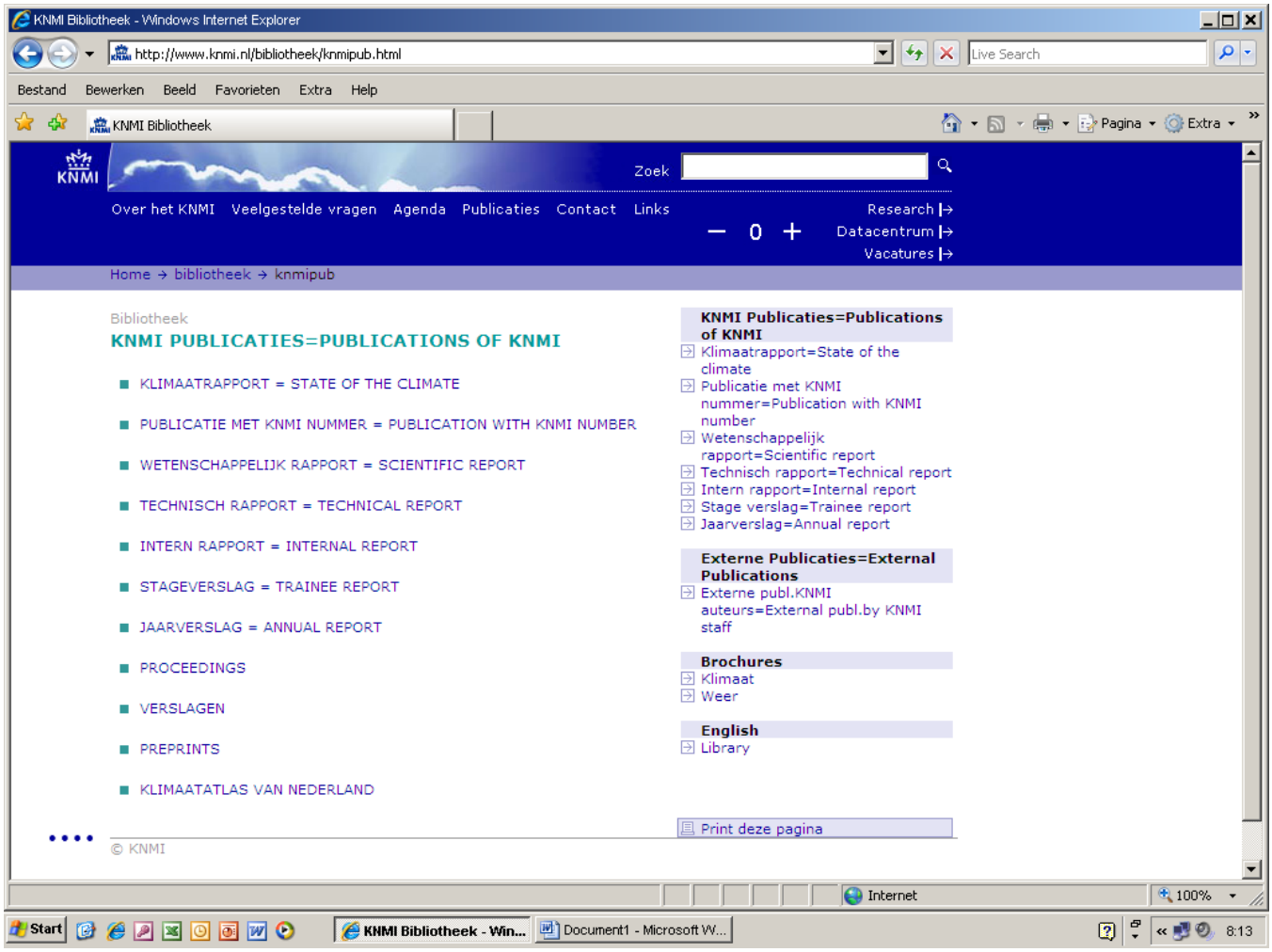

All titles of KNMI-publications (and a full text PDF for the most recent ones) can be found on

http://www.knmi.nl/bibliotheek/knmipub.html

If you have any questions, please contact us: bibliotheek@knmi.nl